Fresh Eyes for an Old Moon: ALMA & JWST Perspectives of Callisto

Thesis by
Maria Noel Camarca

In Partial Fulfillment of the Requirements for the
Degree of
Doctor of Philosophy

CALIFORNIA INSTITUTE OF TECHNOLOGY
Pasadena, California

2025
Defended May 16, 2025

Maria Noel Camarca
ORCID: https://orcid.org/0000-0003-3887-4080

ACKNOWLEDGEMENTS

If the only prayer you said was thank you, that would be enough. — Meister Eckhart

Prior to arriving at Caltech, I enjoyed thinking about who my future friends and mentors would be when a new chapter of my life started in Pasadena. The time has come to offer these people my thanks, and I could not be happier to write this part of my thesis.

Firstly, I want to thank Prof. Katherine de Kleer for being my advisor. Thank you, Katherine, for your careful guidance, your scientific creativity, your strong sense of scientific ethics, and most importantly, your encouraging and patient mentorship over the last six years. I am so excited to see what the future holds for you as you continue on through your professorial career in astronomy, and know that it was an honor to be your first graduate student :). I may not be able to repay you for the gift of charitable mentorship you've given me, but know I will do my best to pay this forward.

There are a number of other Caltech faculty members that deserve my thanks. I am grateful for the guidance of my Thesis Advisor Committee (TAC), including Profs. Bethany Ehlmann, Geoff Blake, and Gregg Hallinan. All of my TAC members were incredibly encouraging and I'm grateful for their contributed expertise to this project. My first time observing with Keck Observatory was as part of the Blake Group when I was doing one of my first year props. So thank you, Geoff, for introducing me to astronomical observing!

I would also like to thank Prof. Andy Ingersoll for being my occasional lunchtime companion and summertime ping-pong opponent. I fear that the new students in planetary are completely unaware of Andy's devastating serves.

To my radio astronomy mentors both inside and outside of Caltech: I don't know if my life is better knowing what a "visibility" is, but I do know I'm better off having received your mentorship. Thanks for holding my hand through it! Bryan Butler, Imke de Pater, and Alex Akins: it's been a pleasure to partake in this small field of astronomy, in no small part due to the humor in the planetary radio community. Specifically on the note of humor and encouragement, Xander Thelen, you take the cake here, thanks for the support that started during my tenure as a post-bac at NASA Goddard, and continued up until the end of this PhD.

My graduate student friends in the planetary science are some of the most creative and skilled young people I have ever had the pleasure of meeting. Know that I wish I could write a whole paragraph about every single one of you! I truly cherished the early days of my planetary science cohort when we were a set of four: Mike McKeon, Marguerite Epstein-Martin, Brandon Rasmussen, and myself. In particular, Mike, I am incredibly grateful for your friendship, and very importantly, your sense of humor. I look forward to following your career as your friend and colleague. Thank you to Julie Inglis for frequently visiting my office with your friendly face and to offer the gift of a hug. Abby Keebler, thank you for opening my eyes to goat cheese. Thank you to Ryleigh Davis and Matthew Belykov, for your companionship on coffee runs and your love of all things JWST. Zac Milby, you are a source of evergreen conversation and your calibrated work-life balance was a much-needed model for many of us in the department, including myself, so thank you. Thank you to my legendary suite of officemates, including YuYu Phua, Kim Paragas, Valeria Kachmar, Eva Scheller and Will Denman. To summarize my experience being YuYu's officemate: you really just had to be there. Thank you to Shreyas Vissapragada, Yaayati Chachan, Aida Behmard, and Jess Spake for your model of incredible scientific drive, your years of friendship, unrivaled taste in music, and tasteful series of kickbacks.

To my friends in graduate school outside planetary, I'm so grateful for you as well. To Jimmy Atterholt and Ben Strozewski: I will remember our multi-year lunch series so fondly, as it was a place where friendship, philosophy (?), and fun takes could flourish. Thank you to Tina Seeger for your incredible scientific enthusiasm! Thank you to Tess Marlin and Maria Derda, I'm so glad we met so early in graduate school such that we could share in the experience together. I'll always be grateful for noodle night. Ina Sorensen, I literally won the Cats housing lottery with you as my first-year random roommate. Thank you to former Blake group member Olivia Wilkins for our many, many friendship walks on nice afternoons around Caltech's beautiful campus and the surrounding lush neighborhoods. Andy Boyle, you are a good trail runner.

To my friends that I met through the Graduate Christian Fellowship (GCF), what a joy your friendship and love for Christ has provided me. Without this group, I wouldn't have had the pleasure of meeting Bekah Loving-Ngo, Sami Chang, Albert Wandui, Grigory Heaton, Nathan Wei, Tanner Harms, Mark Zhang, Andy Ylitalo, Caroline Paules, Rachel Gehlhar, and Hannah Manetsch. With this group there

were so many Monday meetings, lovely hikes, terrible movie nights, boba adventures, Saturday morning runs, and importantly, material and spiritual accompaniment. Rachel, thanks for encouraging me to see this thesis document as just a really complicated lasagna that *will* come together in the end :). Hannah, thank you for your joy and the eyes of mercy through which you see the world.

Additionally, my time at Caltech would not have been the same without the students in the Caltech Catholics group: Jorge (+Hayley) Llop, Nick (+Mairead) Friesenhahn, Brendan Lynch, Lauren Conger, Daniel Park, and Tim Csernica. To Stephanie Breunig, thank you for being my friend and roommate for those years :). Alessandra Flaherty, you know how meaningful your friendship is for me. Thank you for praying for me when I couldn't pray for myself. Thank you to Katt Redmond for the gift of friendship and mentorship. Thank you to other folks at my parish, St. Phillip's, including Krista Corbello and Fr. Tony Gomez.

Thank you to my professors from undergrad: my thesis advisor Prof. Deana Jaber, my academic advisor Dr. Eric Bubar, and other professors whose professional encouragement I benefited from: Prof. Stacy Lopresti-Goodman and Prof. Susan Agolini, thank you. And to my professors from my gap year at American University, Profs. Phil Johnson and Nathan Harshman, thank you for welcoming me into the AU fold!

Thank you to my advisors and colleagues from my post-bac days at NASA Goddard. Without this time of preparation, I would not be in the field. Thank you to Drs. Mike Mumma, Geronimo Villanueva, Lucas Paganini, Sara Faggi, and Manuela Lippi. Thank you to Maureen Palmer and Nick Lombardo for your friendship.

To Karin Öberg: thank you for encouraging me to apply to Caltech planetary. I shared with you my proposed list of graduate school applications, you decided that it wouldn't do, and then you completely breathed ambition into my plans. For this, I am beyond grateful.

Thank you to my friends who were with me before Caltech: Michaela Houchens, John Sampson, Angela Wagner, Susanna Wise, Sarah Boelsche, Emily Ott, Kaitlin Atterbury, Hansel D'Souza, Mary and Dominic Mangino, and Erin Donn.

To my extended family; thank you for following along this journey and reaching out throughout the years with messages of support. Aunt Margaret, thank you so much for moving me out to Pasadena. Uncle Mike Fegan and Aunt Mary Camarca, thanks for being great godparents.

To my new family by marriage, the Halpins (+ Ambuul, Sparks, Curtis, O'Donnell, and Martinez families): thank you for welcoming me with open and loving arms into your family. Tim and Susan Halpin, thank you for letting me practice my presentations with you, for being so enthusiastic about my science, and for the gift of your son.

To my brothers and sisters, Luke, Jozef, Sean, Anastasia, Kateri, Vinny, and Gigi: there are not enough lines in this document that could sufficiently capture my gratitude for your love and support. After leaving home in the early morning to catch that one-way flight from Dulles to LAX, I cried in the car thinking of how much I'd miss you. What a joy it was to have you visit throughout the years. Gigi, thank you for all the mail :), I'll always be your valentine and scientist.

To my Mom and Dad: thank you for the gift of a loving home. A home where you encouraged your children to pursue their vocations, whatever they might be.

To my spouse, Thomas: of all of the words typed in this document, the most consequential ones are the ones that remind you how much I love you.

ABSTRACT

As though its surface were frozen in time, Jupiter's moon Callisto has seemingly done little more than collect and degrade impact features since its formation some ∼4.5 billion years ago. One outcome of Callisto's quiescence is that its geologic map retains only a few units, with large-scale landforms consisting of either enormous multi-ring impact basins or crater-laden plains. Despite this geologic simplicity, our knowledgebase of Callisto's material surface properties and volatile ice distributions is limited compared to the other icy Galilean moons. Understanding how Callisto localizes its thermal properties and delicate volatile ices is essential to understanding how long-term particle bombardment, solar insolation, and extended impact damage has sculpted its aged surface. While Callisto's much more active sibling satellites have scrubbed some or all of their surfaces free of the most ancient records, the oldest surface processes in the Galilean system remain visible today on Callisto. And with large telescope facilities such as the Atacama Large Millimeter/submillimeter Array (ALMA) and the James Web Space Telescope, these surface properties are now accessible to Earth-based observers.

In Chapters 2 and 3 of my dissertation, I complete the icy Galilean satellite ALMA catalog with the full Callisto dataset which includes leading and trailing hemisphere images at ALMA Bands 7, 6, and 3, corresponding to 343, 223, and 97 GHz, respectively. At these frequencies, we sample the subsurface depths of order a few centimeters down to about half a meter. From these data, I demonstrate that Callisto's' subsurface thermal emission is much less susceptible to diurnal variation compared to the other icy satellites and that while Callisto's largest craters are thermally consistent with much smaller ones, the warm surface anomalies tell a story of impact bombardment not recorded in current geologic maps. Moreover, I identify several cold anomalies associated with large impacts, as well as one that might be relevant to Callisto's tenuous and patchy CO_2 atmosphere.

In Chapter 4 of my dissertation, I present the results from a JWST NIRSpec 2.85–5.35 μm observing campaign that allowed us to inspect many of Callisto's volatile surface materials for the first time since the end of the Galileo mission in the early 2000s. In this work, I identify the Lofn/Heimdall impact region as Callisto's largest source of non-radiolytic CO_2. This particular crater suite may represent one of the best locations on Callisto to look for deep subsurface materials brought to the surface by the impact. Additionally, I propose Callisto's well-known radiolytic CO_2 trailing

hemisphere bullseye is accompanied by a second bullseye in water ice exposure that may share a common origin.

Lastly, in Chapter 5, I offer a brief synthesis of the icy moon ALMA survey, an endeavor that fulfills scientific promises that pre-date the array itself.

Altogether, this dissertation offers the community two of the key Callisto datasets of the 2020s era of research. Now that ESA's JUICE mission and NASA's Europa Clipper are en-route to the Jovian system, this research offers a timely complement to what is a blossoming era for Callisto and broader icy satellite exploration.

PUBLISHED CONTENT AND CONTRIBUTIONS

Camarca, M. et al. (2023). "Thermal Properties of the Leading Hemisphere of Callisto Inferred from ALMA Observations". *The Planetary Science Journal* Vol. 4, No. 8. DOI: 10.3847/PSJ/aceb68.

M.C. participated in the direction of the project, reduced and calibrated the ALMA data, ran the thermal modeling scripts, led the interpretation, and wrote the manuscript.

TABLE OF CONTENTS

LIST OF ILLUSTRATIONS

LIST OF TABLES

Chapter 1

INTRODUCTION

In his consequential treatise *Sidereus Nuncius*, the Italian astronomer Galileo Galilei (1564–1642) recounts observations of the night sky he made with his homemade telescope (Galilei, 1610). The publication of *Sidereus Nuncius* marks an inflection point in the history of astronomy that is of almost unrivaled magnitude. His careful drawings of the Moon as seen through the telescope revealed a place with its own mountains and its own valleys, a place where the sunshine falls on textured landforms—a place like Earth. This challenged the Aristotelian vision that our Moon rested in the heavens as a perfect, smooth sphere (Wootton, 2010). Accompanying his drawings of lunar surface texture are observations of the mighty planet Jupiter. On the night of January 7th 1610, Galileo recorded that there were a suite of stars arranged neatly in a line near Jupiter. Over the next few days, the stars remained close to Jupiter, but changed their positions relative to one another. These observations prompted Galileo to recognize what he saw were not stars, but instead a family of moons. This finding helped confirm the Copernican model that the Earth is not the center of the universe (Wootton, 2010). If Galileo were alive today, he might be pleased to learn that one of the great endeavors of modern planetary science is to marry the study of surface textures and landforms with the moons named in his honor, the Galilean moons.

Excitingly, today we understand that the Jovian satellite system first observed by

Figure 1.1: The Galilean satellites. From left to right: Io, Europa, Ganymede, and Callisto. Image credit: NASA/JPL/DLR

Galileo is less like a set of "scaled-up" versions of Earth's moon, and more like a scaled-down set of planets (Fig. 1.1). All of them except for Europa are larger than Earth's Moon, and Ganymede and Callisto are even "Mercury-sized." The orbital periods are all very short, and range from about forty-two hours for Io to just over two weeks for Callisto[1]. However, just like Earth's moon, all of these satellites are tidally locked, meaning that an observer from Jupiter's perspective will only ever see one face of these moons. Although the moons themselves are enormous, they are still very small compared to Jupiter, such that if you added up all their masses, it only results in about 0.02% of Jupiter's mass. Indeed, all of the aforementioned characteristics—the resonant configuration, the mass ratio to the host—mirror the physical and orbital properties that have emerged as key trends among the many other solar systems we have discovered elsewhere in the Galaxy (Laughlin et al., 2015). This is why the Galilean moons are rightfully understood as a miniature solar system right in our backyard. And in the same way that our Solar System bears four terrestrial planets—Mercury, Venus, Earth, and Mars—with wonderfully different surface histories, so too does the Galilean system bear four worlds with a treasury of geologic activity. The outermost moon, Callisto, is the muse of this thesis.

1.1 Scope of This Work

Studies of individual planets generally fall into one of three categories: the surface, the interior, or the atmosphere. None of these categories are truly mutually exclusive, because many planetary objects bear complex atmosphere-surface and surface-interior exchange processes. Therefore, forwarding our understanding of one piece of a planet may ultimately improve our understanding of the other pieces. The work enclosed in this document dedicates its attention to one piece of Callisto—its surface. Specifically, the primary endeavor of this thesis is to understand the material thermal properties of Callisto's ancient surface. The other task of this thesis is to forward our understanding of the satellite's surface chemistry. For an icy, airless planetary satellite such as Callisto, determining how material properties and surface chemistry vary across a surface, either in predictable or unpredictable ways, is a key that unlocks the door to a greater understanding of the geologic history of that object, and paves the way for deciphering the balance between endogenic and exogenic modifications to that object. The goals of this thesis were accomplished using two telescope facilities, namely the Atacama Large Millimeter/submillimeter

[1] `https://nssdc.gsfc.nasa.gov/planetary/factsheet/galileanfact_table.html`

Array (ALMA) and the James Webb Space Telescope (JWST).

A brief summary of the thesis chapters is as follows. The content of Chapter 2 is a targeted analysis of Callisto's leading hemisphere using a 343 GHz ALMA observation, which features its largest impact basin, Valhalla. I find that, consistent with prior spacecraft observations, Callisto's thermal emission profile is not well described using homogeneous thermal properties. Moreover, I confirm that icy craters in the Galilean system bear cold thermal signatures even at their most extreme sizes, and identify an area to the south of Valhalla as thermally-unique terrain.

In Chapter 3, I perform a comprehensive analysis of the entire Callisto ALMA data set. In this work, I reduce and analyze observations of Callisto's leading and trailing hemisphere in three ALMA bands from 97–343 GHz. For this larger-scale project, I explore three different thermophysical modeling approaches to fit the thermal emission profiles retrieved from ALMA. Consistent with the paradigm, I find that Callisto's submillimeter/millimeter emission at other frequencies and for other hemispheres is not well-fit using only single thermal inertia and emissivity. Rather, fits are improved by adopting either a two-thermal inertia model, or models with a variable electrical skin depth. With these approaches, I find that the material properties in the upper 10s of cm of the subsurface are consistent with higher emissivities (consistent with past work, e.g. Muhleman et al. 1991; Moore et al. 2004) and higher thermal inertias compared to its icy Galilean siblings. For many observations, the application of these more complex modeling procedures helps to suppress large-scale spatial structure in the residuals that otherwise obscures the thermal features due to geology. However, the trailing hemisphere observations at 97 and 233 GHz persistently display large-scale spatial structure in the temperature residuals that suggests some model physics (e.g., roughness) may be required for future analyses. For the observations with thermal residuals that do appear mostly driven by the underlying geology, I recover cold anomalies observed for Valhalla and the Lofn region in the 343-97 GHz regime, and identify a possible cold thermal anomaly in the trailing hemisphere 97 GHz observation that may provide context for JWST observations of Callisto's patchy CO_2 atmosphere (Cartwright et al., 2024).

In Chapter 4, I look at Callisto through the infrared eyes of JWST. I present the first high-sensitivity, global map of the 3.1 μm water ice feature, including updated maps of CO_2 and other volatiles using a new observation centered on Callisto's largest impact feature, Valhalla. In this work, I demonstrate that on the leading hemisphere, the strength of the Fresnel peak is primarily driven by the geology (i.e., major im-

pacts). On the trailing hemisphere, I find a new hemisphere-sized trend, namely a bullseye pattern for the Fresnel peak band areas with a depletion in the center of this disk. I speculate that this trend may be related to the same radiolytic processes that drive the synthesis of CO_2 in Callisto's dark regolith. Moreover, I find that the Lofn/Heimdall impact suite in Callisto's southern hemisphere may contain the largest amount of non-radiolytic CO_2 on Callisto. This finding is significant because Lofn might be one of Callisto's most promising terrains to look for materials excavated from a subsurface water-rich zone.

In Chapter 5, I write a short synthesis of the main scientific outcomes of the ALMA continuum survey of the Galilean moons. I highlight the most salient trends in the thermal properties between the three icy satellites, and identify the geology-temperature motifs common among the three. Additionally, I return to ALMA planning documents to highlight that the complete survey of the thermal emission of the Galilean satellites fulfills a decades-old scientific goal that predates ALMA itself. Lastly, I identify a few avenues for merging these ALMA results with those obtained at other wavelengths.

The chapters described may be treated as standalone units. Chapter 2 is published, 3 is in review, and Chapters 4 and 5 are in preparation for submission. As such, the introduction section of this thesis is a merger of the key themes from the introductions written for each chapter. Some portions of the introduction feature expanded language aimed at making the relevant physics accessible to a wider audience.

In the subsequent sections of this introduction, I will first describe the unique world that is Callisto, and summarize the geology of this moon upon which this work is to be interpreted. Afterwards, I will motivate the radio astronomy component of this thesis by summarizing the usefulness of thermal property studies in planetary science, and identify the gap in our understanding prior to this work. Next, I summarize the motivations for the JWST observations.

1.2 Summary of the Geology of Callisto

The story of Callisto's surface is one that diverges from the patterns of activity typical among large moons in the Solar System. At a diameter of ~4820 km, Callisto is our solar system's third largest moon, after Ganymede and Titan. Typically, large planetary satellites bear evidence for some kind of geologic activity in the past, and in special cases, the present. Among the inner three Galilean satellites Io, Europa and Ganymede, there are many examples of geologic activity both old and new.

For instance, Io is the most volcanically active body in the Solar System. Its colorful orange, red, and yellow surface is covered in lava lakes from which powerful, present-day eruptions are regularly documented by spacecraft and telescopes[2] (e.g., Morabito et al., 1979; Davies et al., 2006; de Kleer et al., 2019; Zambon et al., 2023). On the young, water-rich surface of Europa abound evidence of tectonic and chemical alterations linked to its salty subsurface ocean (McCord et al., 1999; Collins et al., 2009). At Ganymede, regions of dark, older terrain are entangled with ribbons of bright, highly tectonically deformed material that offers evidence of major past disruption (Pappalardo et al., 2004). Upon arrival at Callisto, one is greeted by a very different kind of terrain, one that appears nearly devoid of any evidence for volcanism, tectonics, or surface-interior interactions of any form.

As a consequence of its inactivity, Callisto's surface at the global scale comprises just a few geologic units, most of which are related to impact craters. The most recent geologic map of Callisto is based on Galileo and Voyager imaging data (Greeley et al., 2000). These units include cratered plains, light plains, and smooth/dark plains, as well as units linked to multi-ring basins or other impacts (Greeley et al., 2000; Moore et al., 2004). Based on the large number of craters Callisto possesses, its surface is arguably the most ancient in the solar system, with terrains at least 4 billion years old (Zahnle et al., 1998).

Imprinted on this incredible record of long-term impact alteration are some extraordinary examples of large-scale craters. One such example includes the multi-ring impact basin, a feature observed on rocky bodies in the form of Orientale on the Moon (Head, 1974) and Caloris on Mercury (Fassett et al., 2009). In particular, Callisto's multi-ring impact basins are the largest and most well-preserved in the solar system. Centered at 15° N, 56° W is Valhalla, the largest of these basins. Valhalla bears outer rings that extend to a diameter of ∼3800 km, a length that exceeds $3/4$ of the width of the lower continental United States. Other large multi-ring basins include Asgard (D∼1400 km, 32° N, 140° W) in the northern hemisphere, and Adlinda (D∼840 km, −49° N, 36° W) in the southern hemisphere. Structures like Valhalla are helpful data points for those interested in the thermal history of Callisto's outer crust, as they are the possible relics of a time when the satellite's crust had a different thermal gradient and viscosity (Mc Kinnon et al., 1980).

The dominance of impacts at Callisto's largest scales is complemented by a story of

[2] Anyone may inspect recent images of Io's volcanism taken by the Keck Twilight Zone Program hosted at `https://www2.keck.hawaii.edu/inst/tda/TwilightZone.html#`

widespread surface degradation at finer scales. It has been shown that Callisto has an underabundance of small (< 1 km) craters relative to Ganymede (e.g., Chapman et al., 1999). Because the same impactors are expected to hit both Ganymede and Callisto, this result suggests that the smallest craters on Callisto are modified by being disaggregated rather than pulverized by smaller impacts, as observed on Ganymede (Moore et al., 2004). Evidence for the self-disassembly of Callisto's rim-forming bedrock is also found in the km-scale high resolution Galileo images. On Callisto, these images show that craters transition from bowls with neatly-defined rims to discontinuous rims with much shallower bowls, possibly due to infill from disaggregated rim material (Fig. 17.2 in Moore et al. 2004). By contrast, the km-scale craters on Ganymede evolve from the typical bowl topography to that pummeled by smaller impacts (Fig. 17.3 in Moore et al. 2004). Other examples of degradational processes on Callisto include examples of landslides in craters, identifiable via their lobe-like deposit shapes (e.g., Fig. 17.16 in Moore et al., 2004). The extent of large-scale surface degradation has been linked to sublimation-driven processes, and for Callisto, has been suggested to require CO_2 as a high-volatility, crustal component (Moore et al., 1999). This sublimation-degradation of Callisto's landforms is intimately related to the other of Callisto's most salient features: its large dark material blanket.

The geometric albedo of Callisto is $\sim$0.2, making it the darkest out of the Galilean moons (Moore et al., 2004). The darkening agent on Callisto is its widespread dark material blanket, inferred to be many meters thick (Moore et al., 2004; Basilevsky et al., 2002) The widespread sublimation on Callisto described in the previous paragraph may help explain Callisto's large share of dark material if this blanket is interpreted as a large lag deposit. However, the balance between the endogenic and exogenic origin of this dark blanket is not fully understood. It is also possible that Callisto has collected infalling dust from the Jovian irregular satellites (Bottke et al., 2013). Part of the difficulty in diagnosing the origin of Callisto's dark material is a lack in our understand of the exact composition of the material. In the post-Galileo view, the secure compositional insight for the dark material appears to be the presence of iron- and Mg-OH bearing minerals (Calvin et al., 1991; Moore et al., 2004). However, the identities of many infrared absorption features in Callisto's non-icy regolith remain uncertain.

In summary, Callisto is one of the Solar System's best long-term records of impact bombardment and its largest geologically inactive moon. Therefore, Callisto is an

ideal target for studying the effects of nearly pure exogenic surface sculpting on an icy moon. Equipped with a review of the geologic setting of Callisto, we now describe the necessity of constraining the thermal properties for a planetary surface, and the need for applying these studies for Callisto.

1.3 Thermal Property Studies and the Case for Callisto

One of the most important vital signs that can be collected for a planetary surface is its temperature. In fact, it is often the first thing many people want to know about a planet (Melosh, 2011). In the timeframe of this thesis, acquiring the temperature of a rocky exoplanet using JWST (Greene et al., 2023) can score you a press release.[3] Why is understanding surface temperature so important? On a global scale, temperature determines whether certain chemical compounds may exist on a planetary surface, and in what phase they may exist (solid, liquid, gas). On more local scales, changes in temperature across a planetary surface can reveal the presence (or absence) of geologic processes that are not always obvious just by inspecting optical images.

For icy, airless satellites such as Callisto, the distribution of surface heat emission is primarily controlled by material properties such as the thermal inertia Γ (SI units of $\mathrm{J\,m^{-2}\,K^{-1}\,s^{-1/2}}$ are assumed throughout) and emissivity ϵ (e.g., Ferrari 2018). Thermal inertia is often parameterized in the following form:

$$\Gamma = \sqrt{k\rho c}$$

where k is the thermal conductivity, ρ is the density, and c is the heat capacity. The thermal inertia of a material is a measure of how resistant that material is to changes in temperature. For example, consider two plastic containers of material left to cool in a refrigerator overnight. In one container, there is a layer of sand, and in the the other is a heavier, flat rock that is about the same volume as the sand. Assuming all other physical properties of the rock and sand are equal, one will find that upon pulling the two materials out of the refrigerator that the sand will warm up to room temperature faster than the rock. This is because loosely compacted (i.e., less dense) materials like sand have a lower thermal inertia than tightly-compacted (i.e., more dense) materials like the rock. For context, the Γ of common planetary materials include water ice $\Gamma \sim 2000$, fresh snow $\Gamma \sim 174$, solid rock (basalt) $\Gamma \sim 1600$-2400, and fine dust $\Gamma \sim 61$ (Melosh, 2011). Emissivity measures the effectiveness

[3] https://www.nasa.gov/universe/nasas-webb-measures-the-temperature-of-a-rocky-exoplanet/

of a material in radiating its energy as heat. It is a unitless quantity ranging from 0 to 1 that is defined as the ratio of energy emitted by a surface to that emitted by a perfect blackbody of the same temperature (Incropera et al., 2007). If the emissivity of a surface = 1, then that surface is emitting like a perfect blackbody. Real-world materials fall somewhere between 0 and 1, and the value of the emissivity can be used as a clue in determining surface composition or texture. For instance, polished metallic surfaces are very low emissivity (e.g., $\epsilon \sim$0.05), while roughened, oxidized metallic surfaces are much higher (e.g., $\epsilon \sim 0.60$) [4]. In this work, the emissivities in question are specifically "spectral" emissivities that are applicable to the specific millimeter/submillimeter frequencies they were made at. Importantly, pinpointing how the material properties such as Γ and ϵ vary spatially across a surface, along with the magnitude of their variation, can help discriminate between the effect of endogenic and exogenic surface processes.

Examples illustrating the diagnostic power of thermal property measurements can be found across many solar system bodies. For example, in the Saturnian system, thermal infrared measurements from the Cassini Composite Infrared Spectrometer were used to study the small icy moons Tethys (Howett et al., 2012; Howett et al., 2019) and Mimas (Howett et al., 2019). These observations revealed that both satellites have a high thermal inertia feature centered at low latitudes on their leading hemispheres that is likely connected to the bombardment of high-energy electrons. This finding demonstrated that the Saturnian particle environment is capable of altering surface texture (Howett et al., 2011; Schaible et al., 2017; Schenk et al., 2011). At the Moon, measurements across the ∼13–400 μm regime from the Diviner Lunar Radiometer on board the Lunar Reconnaissance Orbiter showed that the Moon's regolith is uniform at global scales, suggesting that processes like impact gardening work quickly to homogenize the upper 10 cm; additionally, maps of local thermal inertia variations helped assign plausible impact ejecta deposits to parent craters (Hayne et al., 2017).

In the Jovian system, recent work with the Atacama Large Millimeter/submillimeter Array (ALMA) has proved useful for characterizing the surface of Io (de Pater et al., 2020), confirming the surficial origin of apparent nighttime hot spots on Europa (Trumbo et al., 2017; Trumbo et al., 2018), and identifying plausible exogenic thermal trends on Ganymede (de Kleer et al., 2021). With all of these studies, surface trends were identified with hemisphere- or global-scale coverage of the planetary

[4] https://www.thermoworks.com/emissivity-table/

body. In particular, some (sub)millimeter/centimeter observations may probe below the strongest time-of-day temperature variations (i.e., below the diurnal thermal skin depth) and the most heavily processed upper surface layers.

Prior to this thesis work, the thermal properties of Callisto's surface were poorly constrained because there are only a few disk-resolved studies at thermal wavelengths. In the infrared, the Voyager Infrared Interferometer Spectrometer and Radiometer (IRIS) instrument returned a featureless spectrum of Callisto, offering little information regarding composition (Moore et al., 2004). However, the eclipse cooling curves showed that Callisto's surface is not thermally uniform, as the best-fit model adopted a two-layer thermal inertia surface with one component of $\Gamma = 300$ overlain by a (mm thick) component of $\Gamma = 15$ (Spencer, 1987). Moreover, the IRIS spectra exhibited a trend of increasing brightness temperature with decreasing wavelength, suggesting unresolved temperature contrasts on the surface; this trend also varied with solar incidence angle, hinting that Callisto's surface may be less smooth than Ganymede's, which did not exhibit this solar incidence angle dependence (Moore et al., 2004; Spencer, 1987). The thermal IR temperature of Callisto's surface was measured to be ∼158 K at 20 μm (Morrison et al., 1972; Moore et al., 2004) and ∼140–150 K at ∼10 μm (de Pater et al., 2021), while the H_2O ice surface temperature derived using H_2O spectral features is somewhat lower at ∼115 K (Grundy et al., 1999). Past disk-averaged thermal wavelength measurements of Callisto's brightness temperature show a decrease from 135 K (de Pater et al., 1989) in the submillimeter regime to about ∼90–100 K at centimeter wavelengths (Pauliny-Toth et al., 1974; Berge et al., 1975; de Pater et al., 1984; Muhleman et al., 1986; Butler, 2012). Although other disk-integrated results for Callisto fill in the gaps between these wavelengths, there is a scarcity of spatially resolved data sets.

This thesis work addresses this scarcity for Callisto by presenting the first global, spatially resolved maps of Callisto's thermal emission at submillimeter/millimeter wavelengths. These maps were acquired using the most suitable telescope for observations at these wavelengths: the Atacama Large Millimeter/submillimeter Array (ALMA).

1.4 Motivation of Infrared Spectroscopy of Callisto using JWST

At present, the study of exposed H_2O ice on Callisto and its sibling Galilean moons is motivated by the large role ice plays in generating their atmospheres, as well as the tendency of ice to track with regional geology. Because the Galilean satellites

are embedded in the intense magnetosphere of Jupiter, the H_2O ice on their surfaces is regularly bombarded by charged particles (electrons, protons, S^+ and other heavy ions) with a wide range of energies from ∼1 KeV to 100s MeV (e.g., Cassidy et al. 2010 and references therein). This interaction of charged particles with the ice then drives a lot of unique chemistry. For instance, H_2O ice radiolysis is a fundamental step in the formation of molecular oxygen (Johnson et al., 1997). Molecular oxygen is an important component of Galilean satellite atmospheres as inferred via UV and optical auroral emissions (de Kleer et al., 2023; Cunningham et al., 2015), and has also been detected on their surfaces, likely trapped in H_2O ice (Spencer et al., 2002; Trumbo et al., 2021). Additionally, H_2O ice may serve as a solid-phase host that helps Callisto retain some of its highly volatile CO_2 (Delitsky et al., 1998).

In the near-infrared, the state of H_2O ice may be probed through analyses of spectral features in the 1 to 3 μm range. Examples of early ground-based observations of H_2O ice on Callisto include those acquired with Kuiper Airborne Observatory (Pollack et al., 1978) and Mauna Kea Observatory (Clark et al., 1980), and evidence for the presence of frost was also noted in early thermal measurements (Morrison et al., 1972). The current primary source of information about Callisto's H_2O ice originates from data acquired by the NIMS instrument onboard the Galileo spacecraft. The NIMS instrument provided spectral measurements in the 0.7-5.2 μm range with a spectral resolving power of ∼40-200 (Carlson et al., 1992). The NIMS data show that the presence of exposed H_2O ice generally tracked with the presence of craters, however the NIMS spectra were often noisy due to internal instrument performance and Callisto's low areal exposure of surface ice (∼10 percent,Hansen et al. 2004).

At present, studies of H_2O and the chemistry of volatiles in the Galilean system are being greatly advanced by the James Webb Space Telescope (JWST). As an infrared telescope, JWST is sensitive to the ro-vibrational absorption and emission features of solid and gas phase volatiles that dominate the surface compositions of these moons. And with the incredible spatial resolution of JWST, the location of these volatiles can be tethered to geologic maps of the surface made from spacecraft data, such that their origins (either endogenic or exogenic) can be evaluated. For example, SO gas has been observed right above an active volcano on Io (de Pater et al., 2023). JWST observations of Europa confirmed that surficial CO_2 reservoirs are largely (but not exclusively) concentrated in chaos terrains located in Tara and Powys Regiones, consistent with a subsurface origin (Trumbo et al., 2023b; Villanueva et al., 2023). JWST observations of Ganymede show in great detail how

the moon's intrinsic magnetic field promotes the collection of select volatiles near the poles (Trumbo et al., 2023a; Bockelée-Morvan et al., 2024). The first published analysis of Callisto using the Near Infrared Spectrograph (NIRSpec) instrument onboard JWST focused on the moon's CO_2 reservoirs (Cartwright et al., 2024). In this work, we provide JWST spectral maps of the 3.1 μm Fresnel Reflectance peak on Callisto. In addition, we extend recent spectral maps of CO_2 and the 4.57 μm feature (Cartwright et al., 2024) with a new JWST observation centered on Callisto's largest impact basin, Valhalla.

BIBLIOGRAPHY

Basilevsky, A. T. et al. (2002). "The Morphology of Small Craters and Knobs on the Surface of Jupiter's Satellite Callisto". *Solar System Research* Vol. 36, No. 4. DOI: 10.1023/A:1019576422376.

Berge, G. L. et al. (1975). "Callisto: Disk Temperature at 3.71-Centimeter Wavelength". *Science* Vol. 187, No. 4175. DOI: 10.1126/science.187.4175.441.

Bockelée-Morvan, D. et al. (2024). "A patchy CO2 exosphere on Ganymede revealed by the James Webb Space Telescope". *Astronomy & Astrophysics* Vol. 690. DOI: 10.1051/0004-6361/202451599.

Bottke, W. F. et al. (2013). "Black rain: The burial of the Galilean satellites in irregular satellite debris". *Icarus* Vol. 223, No. 2. DOI: 10.1016/j.icarus.2013.01.008.

Butler, B. (2012). *ALMA Memo 594*.

Calvin, W. M. et al. (1991). "Modeling the reflectance spectrum of Callisto 0.25 to 4.1 μm". *Icarus* Vol. 89, No. 2. DOI: 10.1016/0019-1035(91)90180-2.

Carlson, R. W. et al. (1992). "Near-Infrared Mapping Spectrometer experiment on Galileo". *Space Science Reviews* Vol. 60, No. 1. DOI: 10.1007/BF00216865.

Cartwright, R. J. et al. (2024). "Revealing Callisto's Carbon-rich Surface and CO_2 Atmosphere with JWST". *The Planetary Science Journal* Vol. 5, No. 3. DOI: 10.3847/PSJ/ad23e6.

Cassidy, T. et al. (2010). "Radiolysis and Photolysis of Icy Satellite Surfaces: Experiments and Theory". *Space Science Reviews* Vol. 153, No. 1. DOI: 10.1007/s11214-009-9625-3.

Chapman, C. R. et al. (1999). "Low spatial density of small craters on Callisto." *Bulletin of the American Astronomical Society* Vol. 31, No. 4.

Clark, R. N. et al. (1980). "The Galilean Satellites: New Near-Infrared Spectral Reflectance Measurements (0.65-2.5 microns) and a 0.325-5 micron Summary". Vol. 41.

Collins, G. et al. (2009). "Chaotic Terrain on Europa". *Europa*.

Cunningham, N. J. et al. (2015). "Detection of Callisto's oxygen atmosphere with the Hubble Space Telescope". *Icarus* Vol. 254. DOI: 10.1016/j.icarus.2015.03.021.

Davies, A. G. et al. (2006). "The heartbeat of the volcano: The discovery of episodic activity at Prometheus on Io". *Icarus* Vol. 184, No. 2. DOI: 10.1016/j.icarus.2006.05.012.

de Kleer, K. et al. (2019). "Io's Volcanic Activity from Time Domain Adaptive Optics Observations: 2013–2018". *The Astronomical Journal* Vol. 158, No. 1. DOI: 10.3847/1538-3881/ab2380.

de Kleer, K. et al. (2021). "Ganymede's Surface Properties from Millimeter and Infrared Thermal Emission". *The Planetary Science Journal* Vol. 2, No. 1. DOI: 10.3847/PSJ/abcbf4.

de Kleer, K. et al. (2023). "The Optical Aurorae of Europa, Ganymede, and Callisto". *The Planetary Science Journal* Vol. 4. DOI: 10.3847/PSJ/acb53c.

de Pater, I. et al. (1984). "VLA observations of the Galilean satellites". *Icarus* Vol. 57, No. 1. DOI: 10.1016/0019-1035(84)90011-3.

de Pater, I. et al. (1989). "Planetary Observations at a Wavelength of 355/zm". *Icarus* Vol. 79.

de Pater, I. et al. (2020). "ALMA Observations of Io Going into and Coming out of Eclipse". *The Planetary Science Journal* Vol. 1, No. 3. DOI: 10.3847/PSJ/abb93d.

de Pater, I. et al. (2021). "SOFIA Observations of Variability in Jupiter's Para-H_2 Distribution and Subsurface Emission Characteristics of the Galilean Satellites". *The Planetary Science Journal* Vol. 2, No. 6. DOI: 10.3847/PSJ/ac2d24.

de Pater, I. et al. (2023). "An Energetic Eruption With Associated SO 1.707 Micron Emissions at Io's Kanehekili Fluctus and a Brightening Event at Loki Patera Observed by JWST". *Journal of Geophysical Research: Planets* Vol. 128, No. 8. DOI: 10.1029/2023JE007872.

Delitsky, M. L. et al. (1998). "Ice chemistry on the Galilean satellites". *Journal of Geophysical Research: Planets* Vol. 103 (E13). DOI: 10.1029/1998JE900020.

Fassett, C. I. et al. (2009). "Caloris impact basin: Exterior geomorphology, stratigraphy, morphometry, radial sculpture, and smooth plains deposits". *Earth and Planetary Science Letters*. MESSENGER's First Flyby of Mercury Vol. 285, No. 3. DOI: 10.1016/j.epsl.2009.05.022.

Ferrari, C. (2018). "Thermal Properties of Icy Surfaces in the Outer Solar System". *Space Science Reviews* Vol. 214, No. 8. DOI: 10.1007/s11214-018-0546-x.

Galilei, G. (1610). *Sidereus nuncius*. DOI: 10.3931/e-rara-695.

Greeley, R. et al. (2000). "Galileo views of the geology of Callisto". *Planetary and Space Science* Vol. 48, No. 9. DOI: 10.1016/S0032-0633(00)00050-7.

Greene, T. P. et al. (2023). "Thermal emission from the Earth-sized exoplanet TRAPPIST-1 b using JWST". *Nature* Vol. 618, No. 7963. DOI: 10.1038/s41586-023-05951-7.

Grundy, W. M. et al. (1999). "Near-Infrared Spectra of Icy Outer Solar System Surfaces: Remote Determination of H2O Ice Temperatures". *Icarus* Vol. 142, No. 2. DOI: 10.1006/icar.1999.6216.

Hansen, G. B. et al. (2004). “Amorphous and crystalline ice on the Galilean satellites: A balance between thermal and radiolytic processes”. *Journal of Geophysical Research: Planets* Vol. 109 (E1). DOI: 10.1029/2003JE002149.

Hayne, P. O. et al. (2017). “Global Regolith Thermophysical Properties of the Moon From the Diviner Lunar Radiometer Experiment: Lunar Regolith Thermophysical Properties”. *Journal of Geophysical Research: Planets* Vol. 122, No. 12. DOI: 10.1002/2017JE005387.

Head, J. W. (1974). “Orientale multi-ringed basin interior and implications for the petrogenesis of lunar highland samples”. *The moon* Vol. 11, No. 3. DOI: 10.1007/BF00589168.

Howett, C. et al. (2011). “A high-amplitude thermal inertia anomaly of probable magnetospheric origin on Saturn’s moon Mimas”. *Icarus* Vol. 216, No. 1. DOI: 10.1016/j.icarus.2011.09.007.

Howett, C. et al. (2012). “PacMan returns: An electron-generated thermal anomaly on Tethys”. *Icarus* Vol. 221, No. 2. DOI: 10.1016/j.icarus.2012.10.013.

Howett, C. et al. (2019). “Maps of Tethys’ thermophysical properties”. *Icarus* Vol. 321. DOI: 10.1016/j.icarus.2018.12.018.

Incropera, F. P. et al., eds. (2007). *Fundamentals of heat and mass transfer*. 6. ed. Hoboken, NJ: Wiley. 997 pp.

Johnson, R. E. et al. (1997). “Photolysis and radiolysis of water ice on outer solar system bodies”. *Journal of Geophysical Research: Planets* Vol. 102 (E5). DOI: 10.1029/97JE00068.

Laughlin, G. et al. (2015). *Exoplanetary Geophysics: An Emerging Discipline*. DOI: 10.1016/B978-0-444-53802-4.00186-X.

Mc Kinnon, W. B. et al. (1980). “Evolution of planetary lithospheres: Evidence from multiringed structures on Ganymede and Callisto”. *Icarus* Vol. 44, No. 2. DOI: 10.1016/0019-1035(80)90037-8.

McCord, T. B. et al. (1999). “Hydrated salt minerals on Europa’s surface from the Galileo near-infrared mapping spectrometer (NIMS) investigation”. *Journal of Geophysical Research: Planets* Vol. 104 (E5). DOI: 10.1029/1999JE900005.

Melosh, H. J. (2011). *Planetary Surface Processes*. DOI: 10.1017/CBO9780511977848.

Moore, J. et al. (2004). “Callisto”. *Jupiter: The Planet, Satellites and Magnetosphere*. Cambridge: Cambridge University Press.

Moore, J. M. et al. (1999). “Mass Movement and Landform Degradation on the Icy Galilean Satellites: Results of the Galileo Nominal Mission”. *Icarus* Vol. 140, No. 2. DOI: 10.1006/icar.1999.6132.

Morabito, L. A. et al. (1979). “Discovery of Currently Active Extraterrestrial Volcanism”. *Science* Vol. 204, No. 4396. DOI: 10.1126/science.204.4396.972.

Morrison, D. et al. (1972). "Temperatures of Titan and the Galilean Satellites at 20 Microns". *The Astrophysical Journal* Vol. 173. DOI: 10.1086/180934.

Muhleman, D. O. et al. (1986). "Precise VLA positions and flux-density measurements of the Jupiter system." *The Astronomical Journal* Vol. 92. DOI: 10.1086/114279.

Muhleman, D. O. et al. (1991). "Observations of Mars, Uranus, Neptune, Io, Europa, Ganymede, and Callisto at a wavelength of 2.66 mm". *Icarus* Vol. 92. DOI: 10.1016/0019-1035(91)90050-4.

Pappalardo, R. et al. (2004). "Ganymede". *Jupiter: The Planet, Satellites and Magnetosphere*. Ed. by F. Bagenal et al. Cambridge University Press.

Pauliny-Toth, I. I. K. et al. (1974). "The Brightness Temperatures of Ganymede and Callisto at 2.8 CM Wavelength". *Astronomy and Astrophysics, Vol. 34, p. 129 (1974)* Vol. 34.

Pollack, J. B. et al. (1978). "Near-infrared spectra of the Galilean satellites: Observations and compositional implications". *Icarus* Vol. 36, No. 3. DOI: 10.1016/0019-1035(78)90110-0.

Schaible, M. J. et al. (2017). "High energy electron sintering of icy regoliths: Formation of the PacMan thermal anomalies on the icy Saturnian moons". *Icarus* Vol. 285. DOI: 10.1016/j.icarus.2016.08.033.

Schenk, P. et al. (2011). "Plasma, plumes and rings: Saturn system dynamics as recorded in global color patterns on its midsize icy satellites". *Icarus, Volume 211, Issue 1, p. 740-757.* Vol. 211, No. 1. DOI: 10.1016/j.icarus.2010.08.016.

Spencer, J. R. et al. (2002). "Condensed O2 on Europa and Callisto". *The Astronomical Journal* Vol. 124, No. 6. DOI: 10.1086/344307.

Spencer, J. R. (1987). "THE SURFACES OF EUROPA, GANYMEDE, AND CALLISTO: AN INVESTIGATION USING VOYAGER IRIS THERMAL INFRARED SPECTRA (JUPITER)." PhD thesis. University of Arizona.

Trumbo, S. K. et al. (2017). "ALMA Thermal Observations of a Proposed Plume Source Region on Europa". *The Astronomical Journal* Vol. 154, No. 4. DOI: 10.3847/1538-3881/aa8769.

Trumbo, S. K. et al. (2018). "ALMA Thermal Observations of Europa". *The Astronomical Journal* Vol. 156, No. 4. DOI: 10.3847/1538-3881/aada87.

Trumbo, S. K. et al. (2021). "The Geographic Distribution of Dense-phase O2 on Ganymede". *The Planetary Science Journal* Vol. 2, No. 4. DOI: 10.3847/PSJ/ac0cee.

Trumbo, S. K. et al. (2023a). "Hydrogen peroxide at the poles of Ganymede". *Science Advances* Vol. 9, No. 29. DOI: 10.1126/sciadv.adg3724.

Trumbo, S. K. et al. (2023b). "The distribution of CO_2 on Europa indicates an internal source of carbon". *Science* Vol. 381, No. 6664. DOI: 10.1126/science.adg4155.

Villanueva, G. L. et al. (2023). "Endogenous CO_2 ice mixture on the surface of Europa and no detection of plume activity". *Science* Vol. 381, No. 6664. DOI: 10.1126/science.adg4270.

Wootton, D. (2010). "The Starry Messenger". *Galileo*. Watcher of the Skies. Yale University Press.

Zahnle, K. et al. (1998). "Cratering Rates on the Galilean Satellites". *Icarus* Vol. 136, No. 2. DOI: 10.1006/icar.1998.6015.

Zambon, F. et al. (2023). "Io Hot Spot Distribution Detected by Juno/JIRAM". *Geophysical Research Letters* Vol. 50, No. 1. DOI: 10.1029/2022GL100597.

Chapter 2

THERMAL PROPERTIES OF THE LEADING HEMISPHERE OF CALLISTO INFERRED FROM ALMA OBSERVATIONS

The content of this chapter was adapted from the following article:

Camarca, M., K. de Kleer, B. Butler, A. B. Akins, A. Thelen, I. de Pater, M. A. Gurwell, and A. Moullet (2023). "Thermal Properties of the Leading Hemisphere of Callisto Inferred from ALMA Observations". *The Planetary Science Journal* Vol. 4, No. 8. DOI: 10.3847/PSJ/aceb68.

Abstract

We present a thermal observation of Callisto's leading hemisphere obtained using the Atacama Large Millimeter/submillimeter Array (ALMA) at 0.87 mm (343 GHz). The angular resolution achieved for this observation was $\sim$0.16″, which for Callisto at the time of this observation ($D \sim 1.05''$) was equivalent to $\sim$6 elements across the surface. Our disk-integrated brightness temperature of 116 $\pm$ 5 K (8.03 $\pm$ 0.40 Jy) is consistent with prior disk-integrated observations. Global surface properties were derived from the observation using a thermophysical model (de Kleer et al., 2021a) constrained by spacecraft data. We find that models parameterized by two thermal inertia components more accurately fit the data than single thermal inertia models. Our best-fit global parameters adopt a lower thermal inertia of 15-50 $\mathrm{J\,m^{-2}\,K^{-1}\,s^{-1/2}}$ and a higher thermal inertia component of 1200-2000 $\mathrm{J\,m^{-2}\,K^{-1}\,s^{-1/2}}$, with retrieved millimeter emissivities of 0.89-0.91. We identify several thermally anomalous regions, including spots $\sim$3 K colder than model predictions co-located with the Valhalla impact basin and a complex of craters in the southern hemisphere; this indicates the presence of materials possessing either a higher thermal inertia or a lower emissivity. A warm region confined to the mid-latitudes in these leading hemisphere data may be indicative of regolith property changes due to exogenic sculpting.

2.1 Introduction

The Galilean moons of Jupiter—Io, Europa, Ganymede, and Callisto—form a continuum of geologic activity for which the inactive endmember is Callisto. A satellite whose surface is dominated almost exclusively by impact craters, Callisto retains one of the oldest surfaces (∼4.5 Gyr) in the Solar System. Although it is the third largest planetary moon and may harbor a subsurface ocean (Zimmer, 2000), Callisto bears little to no evidence for any tectonics, volcanism, or other manifestations of surface-interior interactions (Moore et al., 2004). By contrast, geologic activity is readily observed on the other Galilean satellites. For instance: Io is volcanically active in the present day and thermal emission from its colorful eruptions is routinely observed using ground-based telescopes (de Kleer et al., 2019) and spacecraft (Mura et al., 2020; Davies et al., 2006); Europa has a young, water-rich surface accompanied by evidence for surface-interior interactions (Carlson et al., 2009); and Ganymede is encircled by bright, ribbon-like, tectonically-deformed regions suggestive of major past activity (Pappalardo et al., 2004). Therefore, as the only Galilean moon with a surface dominated by exogenic sculpting, Callisto stands out as one of the best records of long-term impact modification the Solar System has to offer.

As a consequence of its inactivity, Callisto's surface at the global scale comprises just a few geologic units. These units include cratered plains, light plains, and smooth/dark plains, as well as units linked to multi-ring basins or other impacts (Moore et al., 2004). In particular, Callisto's multi-ring impact basins are the largest in the Solar System. Valhalla, the largest of these basins, has outer rings extending to a diameter of ∼3800 km and occupies ∼16% of Callisto's surface area. Structures like Valhalla are possible relics of a time in Callisto's history where the surface had a higher thermal gradient and was more ductile (Schenk, 1995) and represent regions of interest to look for exposed subsurface materials. While the multi-ring basins are the most obvious large features on Callisto, the dominant landform is the heavily cratered plains. These swaths of impact-scarred terrain are often blanketed by a dark material for which the exact composition and origin remains uncertain, with endogenic explanations often focusing on surface erosion/sublimation processes (Moore et al., 2004) and exogenic theories usually invoking dust infall from the irregular Jovian satellites (Bottke et al., 2013). Although Callisto retains the largest share of dark material (its albedo is 0.2, the lowest of the Galileans, Moore et al. 2004), Europa and Ganymede also have similarly dark products on their surfaces (Greeley et al., 2004; Pappalardo et al., 2004). Altogether, these features contribute to the fact that Callisto's quiescent surface remains poorly understood.

For many Solar System objects, unknowns pertaining to unique geologic features or the balance of exo- and endogenic processes on their surfaces have been investigated by inferring material properties from thermal observations. At wavelengths in the infrared and (sub)millimeter, radiation originates from the surface/near-subsurface and can be leveraged to infer properties such as emissivity, thermal inertia (Γ = J m^{-2} K^{-1} s$^{-1/2}$; henceforth thermal inertia will be given without units but always uses these SI units), porosity, etc. The variation of such properties across a surface encodes information as to how that surface evolved and provides clues regarding the nature of the external modification environment. For example, in the Saturnian system, thermal infrared Cassini Composite Infrared Spectrometer (CIRS) measurements of the small icy moons Tethys (Howett et al., 2012; Howett et al., 2019) and Mimas (Howett et al., 2011) revealed both satellites have a high thermal inertia feature centered at mid-latitudes on their leading hemispheres, demonstrating the Saturnian particle environment is capable of altering surface texture (Howett et al., 2011; Schaible et al., 2017; Schenk et al., 2011). At the Moon, measurements across the ∼13-400 μm regime from the Diviner Lunar Radiometer onboard the Lunar Reconnaissance Orbiter showed that the Moon's regolith is uniform at global scales, suggesting processes like impact gardening work quickly to homogenize the upper 10 cm; additionally, maps of local thermal inertia variations helped assign plausible impact ejecta deposits to parent craters (Hayne et al., 2017). In the Jovian system, recent work with the Atacama Large Millimeter/submillimeter Array (ALMA) has proved useful for characterizing the surface of Io (de Pater et al., 2020), confirming the surficial origin of apparent nighttime hot spots on Europa (Trumbo et al., 2017; Trumbo et al., 2018), and identifying plausible exogenic thermal trends on Ganymede (de Kleer et al., 2021a). With all of these studies, surface trends were identified with hemisphere-scale or global-scale coverage of the planetary body. In particular, some (sub)millimeter/centimeter observations may probe below the strongest time-of-day temperature variations (i.e., below the diurnal thermal skin depth) and below the most heavily processed upper surface layers.

At present, the thermal properties of Callisto's surface are poorly constrained because there are only a few disk-resolved studies at thermal wavelengths. In the infrared, the Voyager Infrared Interferometer Spectrometer and Radiometer (IRIS) instrument returned a featureless spectrum of Callisto, offering little information regarding composition (Spencer, 1987). However, the eclipse cooling curves showed that Callisto's surface is not thermally uniform, as the best-fit model adopted a two-component thermal inertia surface with one higher component of $\Gamma = 300$ and a

lower component of $\Gamma = 15$ (Spencer, 1987). Moreover, the IRIS spectra exhibited a trend of increasing brightness temperature with decreasing wavelength, suggesting unresolved temperature contrasts on the surface; this trend also varied with solar incidence angle, hinting that Callisto's surface may be less smooth than Ganymede's, which did not exhibit this solar incidence angle dependence (Spencer, 1987). The thermal IR temperature of Callisto's surface was measured to be ∼158 K at 20 μm (Morrison et al., 1972; Moore et al., 2004) and ∼140-150 K at ∼10 μm (de Pater et al., 2021), while the H_2O ice surface temperature derived using H_2O spectral features is somewhat lower at ∼115 K (Grundy et al., 1999). Past disk-integrated radio thermal wavelength measurements of Callisto's brightness temperature show a decrease from 135 K (de Pater et al., 1989) in the sub-mm regime to about ∼90-100 K at cm wavelengths (Pauliny-Toth et al., 1974; Muhleman et al., 1986; Butler, 2012; Berge et al., 1975; de Pater et al., 1984). Although other disk-integrated results for Callisto fill in the gaps between these wavelengths, there is a scarcity of spatially resolved datasets.

In this work, we present the first high-resolution thermal observation of Callisto using ALMA by mapping the leading hemisphere at 0.87 mm (343 GHz). Section 2.2 describes the observations, data analysis, and flux calibration. Section 2.3 details the thermophysical model used to interpret the data and describes how surface properties are derived. Section 2.4 presents the final, calibrated leading hemisphere image of Callisto as obtained with ALMA and includes the results and interpretation of the thermophysical modeling analysis. Section 2.5 summarizes the conclusions of this work.

2.2 Methods

Observations

Our observations of Callisto were acquired using ALMA. Located on the Chajnantor plateau in the Atacama desert, Chile, the main ALMA array is composed of 54 12-meter radio antennas that are linked via a correlator to function as an interferometer. As an interferometer, ALMA can achieve higher spatial resolution on planetary objects than is possible using single-dish facilities at the same wavelength. The spatial resolution ALMA can achieve, combined with its frequency coverage, make this telescope facility ideal for conducting thermal studies of the Galilean satellites from Earth.

We observed the leading hemisphere of Callisto using ALMA on 2016 November

01. The data were taken using the Band 7 receiver at a central frequency of 343 GHz (0.87 mm) with four spectral windows collectively spanning ∼8 GHz and an on-source integration time of 121 s. During observations, the array was in configuration C-5 with 39 12-m antennae. The baselines ranged from 18.6 m to 1.1 km, affording an angular resolution of ∼0.16″. The angular diameter of Callisto during data acquisition was ∼1.05″, so ∼6 resolution elements across the disk were achieved, equivalent to a spatial footprint of ∼790 km at the satellite's distance. At the time of the observation, the sub-observer longitude was 50° W. Calibration for array pointing, flux density, bandpass response, and phase were obtained via observations of quasars J1256-0547 and J1232-0224.

Data Analysis

After observations, the data were provided as a pipeline-calibrated measurement set containing the visibilities, which are the fundamental quantities measured by an interferometer and are equal to the Fourier transform of the sky brightness temperature distribution at discrete spatial frequencies (Muders et al., 2014). For a review of the interferometric observation and imaging of Solar System objects, see Butler et al. (1999). Because continuum observations of the Galilean satellites typically have very high signal-to-noise ratios (SNR) and easily modeled shapes (disks), we improved the SNR of the final pipeline-generated images by applying an iterative self-calibration procedure (for an in-depth explanation of self-calibration, see Brogan et al. (2018)). To conduct this processing, we used the Common Astronomy Software Application (CASA) package (McMullin et al., 2007). As ALMA observations at 0.87 mm (343 GHz) probe continuum emission from the subsurface, we integrated the signal over the entire 8 GHz of bandwidth using multi-frequency synthesis (Sault et al., 1994). Our phase-only self-calibration using CASA followed as such: for the first round of imaging, a Lambertian disk scaled to the size and brightness temperature of Callisto was used as a startmodel for the `tclean` task (Rau et al., 2011); no additional clean components were added. Next, the complex antenna-based gains were calculated using the CASA `gaincal` task on a interval spanning the full integration time (i.e., > 121 s) and then applied using `applycal`. Then, the corrected visibilities were imaged again adopting a shallow clean, using the previous `tclean` output image as the startmodel. This cycle of cleaning and computing gains continued down to an interval of 2 s, at which the image SNR ceased to substantially improve. A dynamic range of ∼580 (peak flux/rms in units of Jy/beam) was obtained for the final image. For `tclean` parameters, we adopted a Briggs weighting scheme

with a robust parameter of 0.0, and used the "Clark" deconvolver (Clark, 1980). A primary beam correction was applied to the self-calibrated image product. The dimensions of the final clean beam were $0.16'' \times 0.19''$. The rms (root-mean-square) noise of the final image (measured from a non-source region of the non-primary beam corrected product) was 0.585 mJy/beam, or about 0.2 K.

After self-calibrating the data, we derived the disk-integrated flux density directly from the visibilities. We report disk-integrated flux densities from these fits rather than from the images because the visibilities are the more direct data product. Reporting the disk-integrated flux is useful for placing our results in context with previous radio observations of Callisto that are largely spatially unresolved. The visibilities were fit with Bessel functions using the CASA task `uvmodelfit` assuming a uniform disk model, fitting to all spectral windows, and by excluding baselines >200 m for an optimal fit, as the longer baselines are sensitive to the variations across the disk, rather than just the disk-integrated flux. The final disk-integrated brightness temperature (T_b) was calculated by inverting the following equation [1]:

$$F_\nu = 10^{26} \frac{\pi R_C^2}{206265^2} \frac{2h\nu^3}{c^2} \times \left[\frac{1}{e^{h\nu/k_b T_b} - 1} - \frac{1}{e^{h\nu/k_b T_{cmb}} - 1}\right] \tag{2.1}$$

where F_ν is the disk-integrated flux density in Janskys, R_C is the radius of Callisto in arcseconds and, in SI units, h is Planck's constant, c is the speed of light, ν is the observation frequency, k_b is the Boltzmann constant, and T_{cmb} is the cosmic microwave background (2.7 K). The uncertainties in the final T_b incorporate flux density scale calibration errors, which was parameterized by a 5% error of the total flux density, and visibility fitting errors on the order of 0.4 mJy. Our final calibrated image is presented in Fig. 2.1.

ALMA Flux Density Calibration Check

The ALMA pipeline applies a flux density calibration to the target data during initial processing. Because the ALMA calibrator sources are quasars (which are variable) and the ALMA pipeline occasionally does not use the most complete calibrator information, manual flux calibration correction is sometimes required (e.g., Trumbo et al. 2018; de Kleer et al. 2021a). We checked whether such a correction was required for these data by comparing the pipeline flux model to the ALMA Calibrator

[1] This equation has a typo in de Kleer et al. (2021a), but is correct in the latest arXiv version of that paper (`https://arxiv.org/pdf/2101.04211.pdf`). The "206265", which is the number of arcseconds in a radian, was not squared.

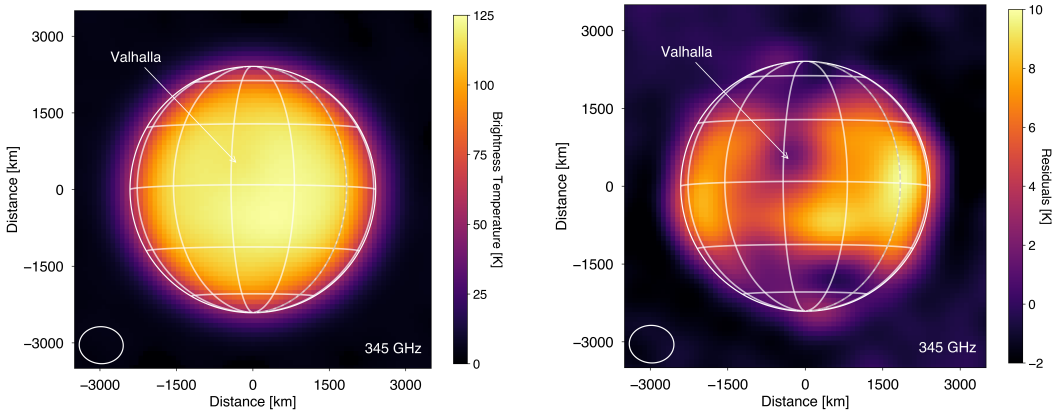

Figure 2.1: (a) Calibrated ALMA Band 7 (0.87 mm/343 GHz) image of Callisto's leading hemisphere. (b) Result of subtracting a sample Lambertian disk from (a) to highlight difference in T_b across the disk. In both images, the ellipse in the lower left corner represents the FWHM (full-width at half-maximum) of the synthesized ALMA beam. The latitude/longitude grid is spaced at 30° increments, and the 0° longitude line is marked with dashes. Callisto's north pole is aligned with the image axis. Notably, the Valhalla impact crater appears slightly colder than other disk regions viewed at similar incident and emission angles.

Catalogue[2] of all observations of our calibration source in the period surrounding our observations. The quasar used for flux calibration was J1256-0547, which the calibrator catalogue recorded observations of at Bands 3 and 7. A check of flux density measurements in these bands between 2016-10-27 and 2016-11-01 (i.e., before and after our data were obtained) indicated it is not necessary to correct the pipeline calibration of these data.

2.3 Thermophysical Model

The final product of calibrating and imaging the ALMA Callisto visibilities is a map of brightness temperature across the satellite's disk (Fig. 2.1). In order to interpret this observed T_b map, we fit the data with a thermophysical model that treats the transport of heat by conduction and radiation through Callisto's surface. For each latitude and longitude on the satellite, the model constructs a temperature profile that evolves with time t and depth z into the surface. Practically, the thermophysical model numerically solves the 1D heat diffusion equation, which is given by:

$$\rho c_p \frac{\partial T}{\partial t} = \frac{\partial}{\partial z}(k\frac{\partial T}{\partial z}) \tag{2.2}$$

[2] `https://almascience.nrao.edu/sc/`

where ρ is the density, c_p is the heat capacity, T is the temperature, and k is the thermal conductivity. For this differential equation, the boundary conditions adopted no heat flow at depth and solar insolation at the distance of Callisto based on spatially varying albedo, as described in Section 2.3. The model was evolved over ∼15 Callisto days (1 Callisto day = 16.69 Earth days) in time steps of at least 1/500 of a day to allow for equilibration, and was run up to several thermal skin depths below the surface. The key tunable parameters in the model are the thermal inertia and emissivity. To find the best-fit model for our Band 7 Callisto image, we performed model runs over a wide range of thermal inertias, ranging from $\Gamma = 15$ to $\Gamma = 2000$, corresponding to values appropriate for very unconsolidated material and water ice, respectively (Ferrari et al., 2016). For each model, we integrated the emission at depth along the line of sight to account for subsurface radiation that is probed at ALMA thermal wavelengths. For full details of the model, including a full description of the radiative transfer, dielectric properties, and other key processes and equations, see Section 3 of de Kleer et al. (2021a). The final output of the model is an image of integrated thermal emission from Callisto's (sub)surface at the viewing geometry of the observations, convolved to the resolution of the ALMA data. The model image is then compared directly to the observations to determine the best-fit thermal inertia and emissivity.

Two-Component Mixtures

Although some models generated using a single thermal inertia provided a better fit for either Callisto's limb or center-of-disk, no single model could fit both parts, regardless of treatment of the surface emission incidence angle dependence (e.g. by using smooth or rough surface implementations). We further considered two-component surface models, which have previously been employed to fit observations of the Galilean satellites, and Callisto specifically. For example, Spencer (1987) reported that Voyager infrared cooling curves of Callisto that displayed an initial, fast cooling followed by a slower cooling rate could be modeled by a surface with a high thermal inertia $\Gamma \sim 300$ overlain by a thin, low thermal inertia layer of $\Gamma \sim 15$. Here, we explored how the systematics in the single model residuals (e.g., rings on the limb in the residuals) could be addressed by a two-component approach.

To create each two-component model, we conducted the following: first, two sets of unconvolved models were generated; the first set adopted thermal inertias ranging from Γ_{lower} = 15-400 and the second set used Γ_{higher} = 500-2000. Each member of the low thermal inertia set was linearly combined with each member of the high

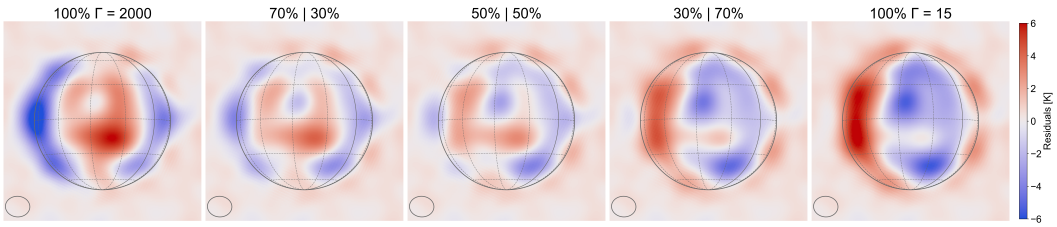

Figure 2.2: Examples of a linear mixture of two models of different thermal inertias (Γ, J m^{-2} K^{-1} s$^{-1/2}$), one using $\Gamma = 2000$ and another using $\Gamma = 15$. Positive (red) and negative (blue) residuals correspond to surface regions in the data that are warmer and cooler than predicted by the model, respectively. The figure demonstrates that very low thermal inertia models predict too little limb emission relative to disk center, while very high thermal inertia models provide a poor fit for the opposite reason; a mixture of the two models provides a better fit without systematic center-to-limb trends in the residuals.

thermal inertia set, forming two-component pairs. For each pair of Γ_{lower} and Γ_{higher} models, we created 11 linear mixtures that ranged from 0% Γ_{lower} + 100% Γ_{higher}, to 100% Γ_{lower} + 0% Γ_{higher}; the models were mixed in increments of 10% (see Fig. 2.2 for an example mixture). The spatial alignment of each model pair was checked for proper overlap. After the components were mixed, the two-Γ model was convolved with the synthesized ALMA beam and subtracted from the data. The emissivity for each mixed model was obtained by performing a least-squares analysis, with the off-disk flux masked out for the calculation. Goodness of fit for the thermophysical models was determined using the cost function, which takes into consideration the number of resolution elements (i.e., ALMA beams). Details for applying the cost function to ALMA data are described in Section 3.4 of de Kleer et al. (2021b); we note that the cost function is formally limited to data sets with independent data points.

Albedo Map

Our model does not treat the albedo of Callisto as a free parameter, rather it ingests a bolometric (bond) albedo map derived from spacecraft data, following Trumbo et al. (2017) and Trumbo et al. (2018) and de Kleer et al. (2021a). For this map, we combined information from: (1) a high-resolution (∼1 km) USGS greyscale map of Callisto's surface[3], with (2) spectral albedos measured at 0.35, 0.41, 0.48, and 0.59 μm obtained at 20 locations by Voyager (Johnson et al., 1983). First, the

[3]`https://astrogeology.usgs.gov/search/map/Callisto/Voyager-Galileo/Callisto_Voyager_GalileoSSI_global_mosaic_1km`

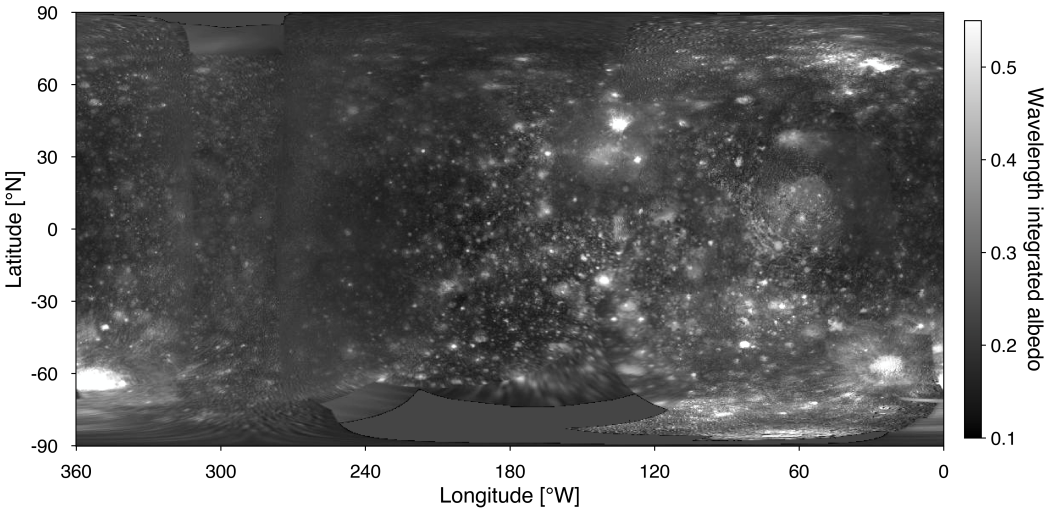

Figure 2.3: A high-resolution version of the wavelength integrated albedo map of Callisto based on Voyager and Galileo data. The creation of this map is described in 2.3.

coordinates of the 20 spectral albedo measurements were used to identify 20 corresponding locations on the USGS map. For each of these locations on the USGS map, an average greyscale value was derived from a 40×40 km box matched to the resolution of Voyager. Next, because the 0.35 - 0.59 μm range covers only ∼80% of the solar spectrum, we extended the spectral coverage by scaling 0.6 – 2.5 μm disk-integrated reflections to our data (Clark et al., 1980). Then, we computed a weighted, wavelength-integrated albedo for each of the 20 points, derived a linear function relating greyscale value to wavelength-integrated albedo, and then mapped this function to the entire USGS map (Fig. 2.3). The wavelength-integrated map was then multiplied by a phase integral of 0.51 (Buratti, 1991) to convert it to a bolometric albedo map. We replaced poorly sampled regions near the poles in the greyscale map with a global average; the exact values of the albedo map at the poles has negligible impact on the thermal model fits since the viewing geometry of the data is nearly equatorial.

2.4 Results & Discussion

We present surface properties derived from an ALMA 0.87 mm (343 GHz) observation of Callisto's leading hemisphere, as well as brightness temperature residual maps created with best-fit thermophysical models. In Section 2.4, we present an integrated T_b measurement, and place our result in context with past, unresolved thermal wavelength observations. In Section 2.4, we describe the single thermal

inertia model results. In Section 2.4, we discuss the results from modeling the data with two thermal inertia components. Lastly, in Section 2.4 we detail the connections between regional temperature signatures and the local geology.

Disk-Integrated Brightness Temperature

We determined the disk-integrated flux density of Callisto's leading hemisphere is 8.03 ± 0.40 Jy at 343.5 GHz (0.87 mm), which is equivalent to a brightness temperature of 116 ± 5 K. In Fig. 2.4, we place our measurement in context with previous disk-integrated quantities obtained over the mm to cm wavelength regime. Overall, our result agrees well with past work, including the SMA measurements by Gurwell & Moullet (ALMA memo #594, Butler 2012) collected in the 0.8-1.3 mm range, as well as an IRAM–PdBI observation at 1.3 mm by Moreno (2007). A separate measurement by Ulich et al. (1984) at 1.3 mm is notably about ∼35 K higher than neighboring results. As seen in Fig. 2.4, there is an overall decrease in brightness temperature with increasing wavelength, with temperatures centered around ∼150 K at 10 μm that drop to ∼90-100 K longward of 1 cm wavelengths. The trend of brightness temperatures cooling off at longer wavelengths can be attributed to several factors, including the fact that lower frequency observations probe deeper into the subsurface where the diurnal wave is attenuated. Additionally, higher thermal inertia (e.g., denser) materials are often found at depth, and can further bring down daytime brightness temperatures. A similar trend of decreasing brightness temperature with wavelength is observed for the other Galilean satellites (see Fig. 4 of de Pater et al. 2021 and Fig. 6 of de Kleer et al. 2021a).

Global Properties: Single Thermal Inertia

We initially fit our ALMA image of Callisto's leading hemisphere using a model parameterized by a single Γ and a best-fit emissivity, and found the global properties were poorly constrained using this approach. The single-Γ models that best-fit the observed T_b distribution is given by $\Gamma = 600$-1800, with emissivities of 0.91-0.93. If it is the case that Callisto's regolith consists of higher-Γ material, then constraining precise Γ values from the model is difficult because the ALMA data probe materials buried at depths that experience low diurnal wave fluctuations; additionally, increasing Γ produces progressively flatter temperature profiles that are difficult to distinguish between. In addition to varying Γ, we tested other model parameters, including the porosity, treatment of refraction, and ice to dust ratio; none of these changes provided a significantly better fit. Mainly, the systematic residuals and poor

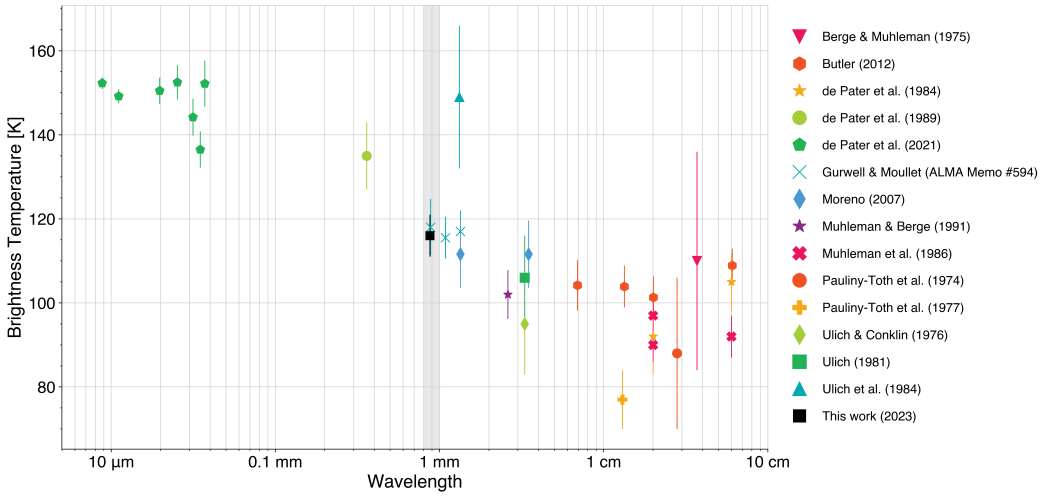

Figure 2.4: Summary of disk-integrated brightness temperature measurements for Callisto plotted as a function of wavelength. The gray vertical bar highlights the wavelength of our measurement, which fits in well with most neighboring data. Data in this plot are taken from: Berge et al. (1975), Butler (2012), de Pater et al. (1984), de Pater et al. (1989), and de Pater et al. (2021), Gurwell & Moullet (ALMA memo #594, Butler 2012), Moreno (2007), Muhleman et al. (1991), Muhleman et al. (1986), Pauliny-Toth et al. (1974) and Pauliny-Toth et al. (1977), Ulich et al. (1976), Ulich (1981), and Ulich et al. (1984).

fits, along with the previous evidence (Spencer, 1987) for a thermally heterogeneous surface, motivated our two-component analysis.

Global Properties: Two Thermal Inertias

Given the difficulties of fitting the observed T_b distribution with a single Γ, we now present the thermal properties acquired by modeling the data with two Γ components. The model parameters that satisfied a cutoff of 2× the minimum chi-squared (χ^2) allow Γ_{lower} = 15-50 and Γ_{higher} = 1200-2000, with best-fit global spectral emissivities of 0.89-0.91 (Fig. 2.5) The acceptable mixing ratios favored the Γ_{higher} component, with ranges varying from 70-50%, compared to 30-50% for Γ_{lower}. An example of how the residuals change with varying the percentage of $\Gamma_{lower}/\Gamma_{higher}$ is shown in Fig. 2.2. While the endmember models have T_b deviations from the data up to around ±6 K, the maximum deviations for the best-fitting two-component models are ∼2-3 K. Fig. 2.2 also demonstrates how the systematic inability of the single-component models to fit the limbs, especially the morning side, is remediated by the two-Γ system.

Context for Callisto's thermal properties derived at millimeter wavelengths is pro-

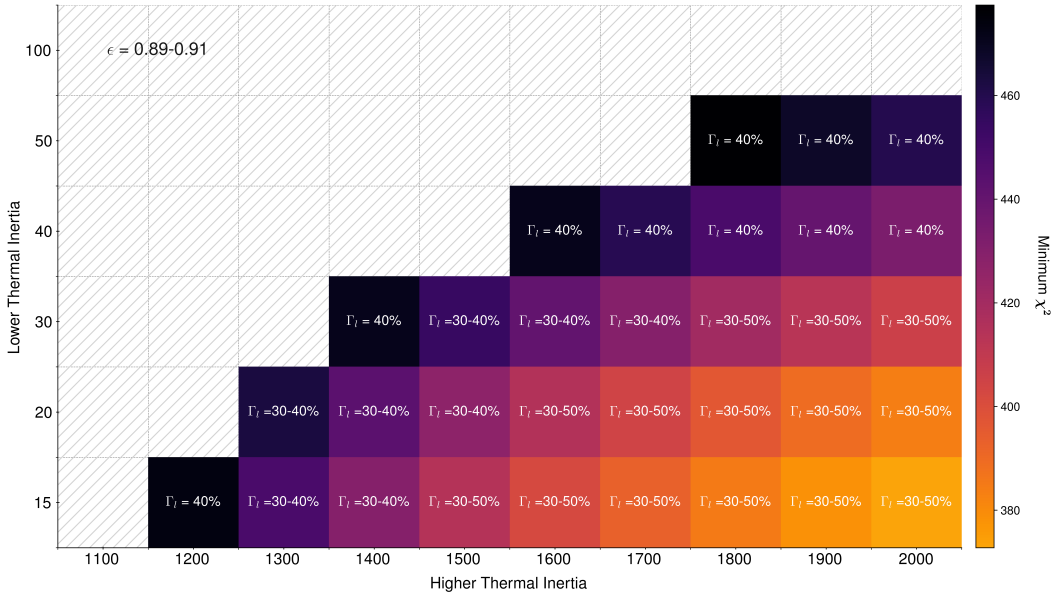

Figure 2.5: Summary of best-fit two-Γ models. Each cell represents the linear mixture results for a combination of Γ_{lower} (vertical axis) and Γ_{higher} (horizontal axis). The text imposed on each cell gives the range of Γ_{lower} (shortened to Γ_l on the plot) that satisfied the χ^2 cutoff. The actual color of each cell corresponds to the minimum χ^2 achieved within a given mixture range. E.g., the cell corresponding to the mixture of the $\Gamma_{lower} = 20$ and $\Gamma_{higher} = 1600$ models is labeled with "Γ_l = 30-50%", meaning that mixtures of 30-50% $\Gamma_{lower} = 20$ and 70-50% $\Gamma_{higher} = 1600$ met the χ^2 constraints. The range of acceptable emissivities is included in the upper left corner of the plot. Empty cells marked with a hatch pattern signal model pairs for which no mixing ratio of thermal inertia components met the χ^2 cutoff. The full range of Γ values tested spanned Γ_{lower} = 15-400 and Γ_{higher} = 500-2000.

vided by previous work at infrared wavelengths. Using the IRIS instrument onboard Voyager, Spencer (1987) found Callisto's infrared emission was best-fit by a model that adopted two, vertically stratified thermal inertia components: an upper $\Gamma = 15^{+2}_{-2}$ layer that controlled the initial fast cooling and a lower $\Gamma = 300^{+200}_{-200}$ that maintained the slower cooling later during the eclipse. As such, our result that a simple, one-Γ model is not sufficient to match Callisto's thermal millimeter emission is consistent with other work. Similarly, our best-fit Γ_{lower} overlaps with the upper layer inferred by Spencer (1987), although there is a larger discrepancy with our inferred second component (Γ_{higher} = 1200-2000). However, comparing the thermal properties derived from IRIS data and 345 GHz ALMA data is not straightforward, given that these wavelengths sense the upper mm of a surface and depths of ∼5 cm into the subsurface, respectively. Importantly, the thermophysical model treatment

by Spencer (1987) assumes that the two thermal inertia components are vertically stratified, while ours is implemented with horizontal segregation. Spencer (1987) did perform a simple test of horizontally stratified two-Γ models, but used Γ values that were best-fits for Ganymede and not best-fits for Callisto. Future work using individual ALMA observations at different observing frequencies will provide a more robust evaluation of vertical heterogeneity at millimeter wavelengths.

Additional context for Callisto's thermal properties derived at millimeter wavelengths is provided by similar ALMA observations of the other Galilean satellites. The mapping of Ganymede by de Kleer et al. (2021a) and Europa by Trumbo et al. (2018) together with the current work on Callisto suggests a general increase of thermal inertia with distance from Jupiter. For example, the T_b distributions on Ganymede observed by de Kleer et al. (2021a) at 343.5, 223, and 97.4 GHz yielded effective thermal inertias of $\Gamma = 450^{+300}_{-250}$, 350^{+350}_{-250}, and 750^{+200}_{-350} respectively, while Trumbo et al. (2018) obtained a much lower $\Gamma = 95$ for Europa with possible surface variations of Γ = 40-300. Using eclipse cooling data, de Pater et al. (2020) inferred Io's thermal inertia to be $\Gamma = 50$ based on the infrared, and around $\Gamma = 350$ based on mm data. Regarding horizontal segregation of surface materials, de Kleer et al. (2021a) tested such two-Γ models to estimate thermal inertia for observations of Ganymede at separate wavelengths, but such models were not preferred to single Γ regimes, which differs from the the proposed explanation for Callisto's T_b distribution. For emissivities, the measured global values for Callisto of 0.89-0.91 are higher than the 0.75 derived for Europa at 223 GHz (Trumbo et al., 2018) and 0.75-0.78 measured for Ganymede at 97.5-343.5 GHz (de Kleer et al., 2021a). This result is reasonable given that the emissivity of ice is lower than rock at millimeter wavelengths and Callisto's surface is not as abundantly ice-rich as its Galilean siblings. Moreover, the spatially-resolved ALMA images of the Galilean moons reveal morphological differences suggestive of their variations in thermal properties (Fig. 2.6). Among the icy Galileans, Callisto's thermal emission is more homogeneous across varying longitudes than that of either Europa or Ganymede, which is consistent with range of inferred thermal inertias inferred for Callisto reaching higher values.

Local Thermal Residuals

In addition to deriving global surface properties from our thermophysical model, we also highlight terrain-specific thermal anomalies that are robust to model parameter changes (Fig. 2.7). Note: references to west/east when describing the relative location or orientation of thermal residuals refers to geographic west/east on Callisto,

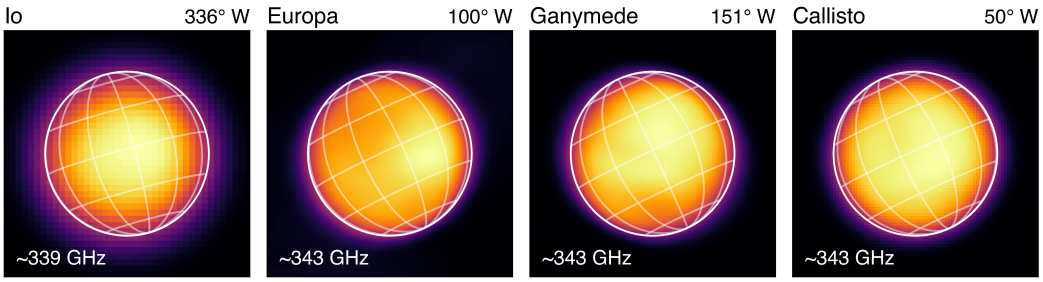

Figure 2.6: Normalized continuum images of the Galilean satellites obtained with ALMA. The longitude indicated on the top right of each plot is the sub-observer longitude at the time of the observation. The latitude/longitude lines are spaced in 30° increments. Io data is from de Pater et al. (2020), Europa from Thelen (2023), Ganymede from de Kleer et al. (2021a), and Callisto is this work.

not astronomical west/east.

Valhalla Impact Basin

A noticeably cool region observed in both the calibrated image (Fig. 2.1) and the model residuals (Fig. 2.7) is well centered on the Valhalla impact basin. This thermal residual is colder by ∼8 K than surrounding terrain in the calibrated image, and about by ∼2-3 K compared to model predictions (which incorporate albedo), meaning the SNR of this residual is ∼10 with the 0.2 K measured image rms. Given that the spatial footprint of our ALMA beam at the distance of Callisto is ∼790 km, this thermal residual (which is larger than the beam) covers the entirety of Valhalla's high-albedo $D \sim 360$ km central zone and part of the $D \sim 1900$ km inner ridge and trough zone (Moore et al., 2004). The strength of the cold residual tapers off in outer trough terrain of Valhalla, which extends to $D \sim 3800$ km (Moore et al., 2004). In terms of morphology, this thermal feature may be slightly extended to the southwest, which is a different direction than the ALMA beam elongation and therefore not an artifact of the non-circular resolution element.

A correlation between cold thermal features and impact craters is a phenomenon observed on both Jovian and Saturnian icy satellites. Often, impacts excavate higher thermal inertia materials from the subsurface (e.g., ice-rich, higher density), creating localized terrain that maintains cooler daytime temperatures relative to surface materials that are more responsive to diurnally varying insolation. This is consistent with the thermophysical model residuals at the location of Valhalla improving as higher global thermal inertias were tested, as demonstrated in Fig. 2.2. Given Valhalla is

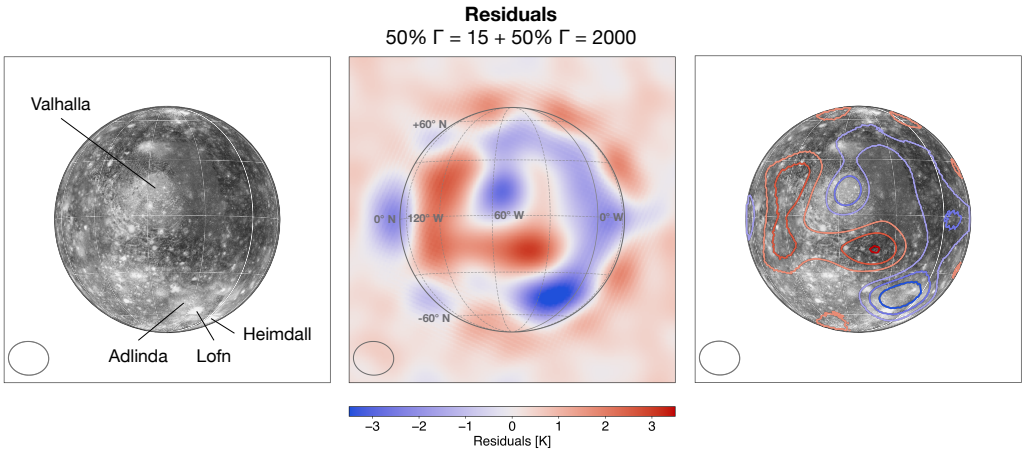

Figure 2.7: A side-by-side comparison of the localized thermal residuals on Callisto with an albedo map projected to the same observer sub-longitude and sub-latitude. The latitude/longitude grid spacing is 30°. The ellipse in the lower left corner of each panel represents the ALMA synthesized beam at the time of observing. *Left panel*: projected albedo map of Callisto with major geologic features identified. Contrast added for ease of identification. *Middle panel*: Representative residuals from the range of best-fit two thermal inertia models. *Right panel*: Residual contour lines drawn on the projected albedo map to better illustrate the correlation between certain warm/cold regions and local terrain. Contours are drawn for $\pm$ 3, $\pm$ 2, and $\pm$ 1 K.

one of the largest impact features in the Solar System, it is expected that this geologic unit contains relatively more exposed subsurface materials. Impact features on other Galilean moons observed to be thermally-cold via disk-resolved observations include Tros and Osiris on Ganymede (de Kleer et al., 2021a; Brown et al., 2022), and Pwyll on Europa (Trumbo et al., 2017; Trumbo et al., 2018). Anomalously cold craters have also been observed in the Saturnian system on Titan (Janssen et al., 2016) and Rhea (Bonnefoy et al., 2020). With the results for Valhalla presented here, this general trend is confirmed to extend to the largest class of impacts in the Solar System.

Adlinda, Heimdall, and Lofn

Valhalla is not the only impact feature in our observation co-located with regional thermal anomalies—a collection of three large craters in the southern hemisphere may be the source of the cold residual located near 40° S and 12° W. This crater complex includes Adlinda and Heimdall, both of which are multi-ring impact features, and Lofn, which sits in-between/on top of the former two. Adlinda is marked

by outer troughs that reach up to $D \sim 850$ km, however almost 1/3 of its structure is obscured by ejecta from Lofn (Moore et al., 2004). Lofn itself is an exceptionally bright, young anomalous dome crater and is Callisto's largest non multi-ring feature ($D \sim 355$ km) (Moore et al., 2004). The morphology of this crater (e.g., unusually shallow relief) and the presence of water-rich deposits suggest the original Lofn impactor struck a relatively liquid/slushy region of Callisto's interior (Schenk, 2002; Greeley et al., 2001; Greeley et al., 2000). Heimdall bears outer rings that extend up to $D \sim 400$ km and center geologic units with albedos high enough to saturate the Galileo images (Greeley et al., 2000). Because these individual craters are below the resolution of this observation, the measured properties are averages between these craters and the surrounding terrains. However, the region can still be seen to possess distinct thermal properties (Fig. 2.7).

As with the Valhalla cold region, the cold spot near the Adlinda/Lofn/Heimdall complex could be explained by impact-excavated higher-Γ surface products. The residual itself diverges from model predictions by about 3-4 K (so SNR ∼15-20) and is roughly 1.5 beams across and is extended toward the northeast. The high albedos of Lofn and Heimdall, as well as spectroscopic evidence, point toward the presence of increased surface ice relative to the surrounding cratered plains, which could result in locally higher thermal inertia. Ligier et al. (2020) interpret their near-infrared maps of Callisto obtained using SINFONI on the VLT to suggest the small grains (25-100 μm) abundance is uniquely enhanced near Lofn and Heimdall (and at high latitudes in general). For an icy surface such as Callisto's, areas with small-grained ice particles can exhibit ice sintering, which increases grain-grain contacts and thereby increases the effective thermal inertia.

Unlike the Valhalla cold residual, however, this cold residual is not well-centered on the three-crater complex— rather, the temperature minimum is located roughly 12° (or roughly 0.08″) northeast of Lofn's bright central region. Although this region is closer to Callisto's limb, where the resolution tapers off due to geometric foreshortening, the fact that the residual is extended toward the northeast, e.g. not in the direction of beam elongation, suggests the offset may be real. Moreover, in the visible albedo map (Fig. 2.7), there is similar cratered terrain to the west of this residual that diverges from model predictions on order of the 0.2 K image rms, implying the thermal properties of the region corresponding to the cold residual are unique. A potential relationship to this residual may be found in the Galileo NIMS maps of CO_2 4.2 μm band depths by Hibbitts et al. (2000). The vicinity of Heimdall/Lofn

bears locally deep CO_2 band depths, with moderate band depths also extending in a northeastern direction. However, because a link is difficult to confirm we only note the spatial correspondence of these features.

Additional Localized Thermal Anomalies

In addition to the thermal residuals on Callisto that appear connected to specific geologic units (e.g, Valhalla and the Adlinda/Heimdall/Lofn complex), there are other residuals that are not correlated to distinct geologic units. The first region is a warm, L-shaped residual that occupies the area west and south of Valhalla. The vertical component of the L is centered at almost 90° W and is symmetric across the equator with a divergence from the model of ∼2-3 K, while the horizontal portion of the L is similarly warm, and extends eastward to ∼25° W. The reason for the L shape may be because the warm region is cropped by the cold Valhalla impact to the northeast. The second region is the colder area that occupies most of Callisto's disk east of Valhalla, starting at ∼25° W and extending toward the limb. According to the geologic map of Callisto (Greeley et al., 2000), both regions are classified as the same cratered plains terrain, despite exhibiting both cold and warm residuals. This is unlike the other significant thermal residuals shown in Fig. 2.7, where the units (i.e. large impacts) are linked to only one type of thermal signature (i.e., cold).

Given the morphology and location of these residuals, one speculation is that the ALMA data are sensitive to surface texture alterations induced by the Jovian particle environment. In the Jovian and Saturnian systems, the leading hemispheres of the icy satellites are preferentially bombarded by micrometeorites and neutral particles (such as dust), with the satellites' equatorial to mid-latitude regions most prominently affected, and their trailing hemispheres are preferentially impacted by charged species. Examples of these phenomena include the hemispheric color asymmetry on Europa (Carlson et al., 2009) and "Pacman"-shaped thermally-cold regions on Mimas and Tethys detected by Cassini (Howett et al., 2012; Howett et al., 2011). Given that the warm L-shape on Callisto's leading hemisphere occupies mid-latitude regions near the satellite's apex of motion, it is possible the local regolith has been texturized to a less-compact material, perhaps due to micrometeorite bombardment since less-compacted regoliths generally have lower thermal inertias and grain contact areas due to lower bulk densities, resulting in faster daytime warming. The micrometeorite bombardment hypothesis is consistent with explanations for similar T_b distributions on Ganymede's leading hemisphere detected with ALMA (de Kleer

et al., 2021a). Moreover, as summarized by Moore et al. (2004), solar phase curves produced by Buratti (1991) also suggest Callisto's leading side is less compact than on the trailing side, although Domingue et al. (1997) using opposition effect data from Thompson et al. (1992) infer the opposite result. Although beyond the scope of the current work, a trailing hemisphere image of Callisto at millimeter wavelengths could confirm if the warm region is actually confined to the leading hemisphere. Even if future observations confirm the equatorial warm region is leading hemisphere-specific, it may originate from several, interacting external modification processes.

2.5 Conclusion

We present a leading hemisphere thermal image of Callisto obtained at millimeter wavelengths (0.87 mm/343 GHz). Our first approach at modeling the thermal emission of Callisto used a thermal model parameterized by a single thermal inertia, for which we obtained a global best-fit of $\Gamma = 600$-1800 (J m^{-2} K^{-1} s$^{-1/2}$) and best-fit emissivities of 0.91-0.93. The single-Γ approach yielded high and systematic residuals that suggested a two-Γ model may describe Callisto's surface more accurately. Our global best-fit two-Γ model adopted $\Gamma_{lower} = 15$-50 and $\Gamma_{higher} = 1200$-2000, with acceptable mixing ratios of $\Gamma_{lower} = 30$-50% and $\Gamma_{higher} = 70$-50%, and emissivities of 0.89-0.91. Our result that a single-Γ model is not sufficient to accurately model Callisto's surface is consistent with results from Spencer (1987) derived using IRIS infrared data. The Γ_{higher} we derived is higher than properties inferred from the infrared, and the presence of a low-thermal inertia component that may suggest the presence of a very uncompact surface component is consistent with other optical results (e.g., Buratti 1991). Callisto's thermal inertia components as inferred from these ALMA data are higher than those on Ganymede ($\Gamma \sim 450$-750; de Kleer et al. 2021a) and Europa ($\Gamma \sim 95$; Trumbo et al. 2017; Trumbo et al. 2018), which agrees with its more thermally-uniform appearance (Fig. 2.6).

In addition to deriving a global best-fit to the T_b distribution, we also examined localized residuals to determine correlations, if any, with regional geologic features. We found that the Valhalla impact basin was co-located with a cold temperature anomaly $\sim$3 K, which extends the association between large impact craters/colder temperatures previously observed on other moons up to the multi-ring impact class. In addition, we found that the other primary cold region in our T_b map is in the vicinity of a collection of craters including Adlinda, Heimdall, and Lofn, of which the latter two are among the brightest and youngest large features on the leading

hemisphere. However, the cold residual is notably extended away from this suite of craters toward the northeast, which may imply surface textures related to factors other than cratering may be relevant. One residual for which there is no obvious association with a geologic unit is a warm L-shaped region that is nearly centered on the leading hemisphere and is constrained to about $\pm$ 30° latitude. We speculated that this feature, like similar warm residuals observed on Ganymede's leading hemisphere (de Kleer et al., 2021a), might represent a region of lower thermal inertia resulting from micrometeorite bombardment that preferentially texturizes the leading hemisphere. However, such a hypothesis is difficult to confirm in the context of a single thermal observation.

The data presented here provide the first spatially-resolved image of Callisto's surface at ALMA observing frequencies. Future analysis of observations that include imaging of Callisto's trailing hemisphere at 0.87 mm/343 GHz, as well as mapping at other thermally-relevant wavelengths (e.g., 100-343 GHz), will help build the global and vertical-depth coverage needed to better understand the thermal features presented here. Additionally, this work offers ground-based observational context for the future European Space Agency (ESA) JUICE (JUpiter Icy Moons Explorer) mission to the Jovian satellites. The JUICE science program highlights Callisto as a key element in crafting the narrative of Jovian satellite formation and the emergence of potentially habitable environments and ocean-bearing worlds (ESA, 2014). ALMA imaging of Callisto in the $\sim$100-343 GHz range will provide a near-subsurface ($\sim$cm-m depths) complement to the JUICE instrument payload, which includes ground-penetrating radar (RIME, $\sim$9 MHz, depths of $\sim$9 km) and the Submillimeter Wave Instrument (SWI, $\sim$530-601 GHz).

Acknowledgements

We acknowledge support from the National Science Foundation Graduate Research Fellowship under Grant No. DGE-1745301 to M.C., and from the Heising-Simons Foundation via a 51 Pegasi b postdoctoral fellowship and under grant #2019-1611 to K.dK. Contributions by A.A. were carried out at the Jet Propulsion Laboratory, California Institute of Technology, under a contract with the National Aeronautics and Space Administration (80NM0018D0004). This paper makes use of the following ALMA data: ADS/ JAO.ALMA#2016.1.00691.S. ALMA is a partnership of ESO (representing its member states), NSF (USA) and NINS (Japan), together with NRC (Canada), MOST and ASIAA (Taiwan), and KASI (Republic of Korea), in cooperation with the Republic of Chile. The Joint ALMA Observatory is operated

by ESO, AUI/NRAO, and NAOJ. The National Radio Astronomy Observatory is a facility of the National Science Foundation operated under cooperative agreement by Associated Universities, Inc.

BIBLIOGRAPHY

Berge, G. L. et al. (1975). "Callisto: Disk Temperature at 3.71-Centimeter Wavelength". *Science* Vol. 187, No. 4175. DOI: 10.1126/science.187.4175.441.

Bonnefoy, L. et al. (2020). "Rhea's subsurface probed by the Cassini radiometer: Insights into its thermal, structural, and compositional properties". *Icarus* Vol. 352. DOI: 10.1016/j.icarus.2020.113947.

Bottke, W. F. et al. (2013). "Black rain: The burial of the Galilean satellites in irregular satellite debris". *Icarus* Vol. 223, No. 2. DOI: 10.1016/j.icarus.2013.01.008.

Brogan, C. L. et al. (2018). "Advanced Gain Calibration Techniques in Radio Interferometry". *arXiv:1805.05266 [astro-ph]*.

Brown, S. et al. (2022). *Sub-surface Observations of Ganymede’s Ice Shell from the Juno Microwave Radiometer*. EGU22-10748. Copernicus Meetings. DOI: 10.5194/egusphere-egu22-10748.

Buratti, B. J. (1991). "Ganymede and Callisto: Surface textural dichotomies and photometric analysis". *Icarus* Vol. 92, No. 2. DOI: 10.1016/0019-1035(91)90054-W.

Butler, B. (2012). *ALMA Memo 594*.

Butler, B. J. et al. (1999). "Solar System Objects". *Synthesis Imaging in Radio Astronomy II*. Ed. by G. B. Taylor et al. Vol. 180.

Carlson, R. W. et al. (2009). "Europa's Surface Composition". *Europa*. Ed. by R. T. Pappalardo et al. University of Arizona Press. DOI: 10.2307/j.ctt1xp3wdw.

Clark, B. G. (1980). "An efficient implementation of the algorithm 'CLEAN'". *Astronomy and Astrophysics* Vol. 89, No. 3.

Clark, R. N. et al. (1980). "The Galilean Satellites: New Near-Infrared Spectral Reflectance Measurements (0.65-2.5 microns) and a 0.325-5 micron Summary". Vol. 41.

Davies, A. G. et al. (2006). "The heartbeat of the volcano: The discovery of episodic activity at Prometheus on Io". *Icarus* Vol. 184, No. 2. DOI: 10.1016/j.icarus.2006.05.012.

de Kleer, K. et al. (2019). "Io's Volcanic Activity from Time Domain Adaptive Optics Observations: 2013–2018". *The Astronomical Journal* Vol. 158, No. 1. DOI: 10.3847/1538-3881/ab2380.

de Kleer, K. et al. (2021a). "Ganymede's Surface Properties from Millimeter and Infrared Thermal Emission". *The Planetary Science Journal* Vol. 2, No. 1. DOI: 10.3847/PSJ/abcbf4.

de Kleer, K. et al. (2021b). "The Surface of (16) Psyche from Thermal Emission and Polarization Mapping". *The Planetary Science Journal* Vol. 2, No. 4. DOI: 10.3847/PSJ/ac01ec.

de Pater, I. et al. (1984). "VLA observations of the Galilean satellites". *Icarus* Vol. 57, No. 1. DOI: 10.1016/0019-1035(84)90011-3.

de Pater, I. et al. (1989). "Planetary Observations at a Wavelength of 355/zm". *Icarus* Vol. 79.

de Pater, I. et al. (2020). "ALMA Observations of Io Going into and Coming out of Eclipse". *The Planetary Science Journal* Vol. 1, No. 3. DOI: 10.3847/PSJ/abb93d.

de Pater, I. et al. (2021). "SOFIA Observations of Variability in Jupiter's Para-H_2 Distribution and Subsurface Emission Characteristics of the Galilean Satellites". *The Planetary Science Journal* Vol. 2, No. 6. DOI: 10.3847/PSJ/ac2d24.

Domingue, D. et al. (1997). "Re-Analysis of the Solar Phase Curves of the Icy Galilean Satellites". *Icarus* Vol. 128. DOI: 10.1006/icar.1997.5730.

ESA (2014). *JUICE Definition Study Report*.

Ferrari, C. et al. (2016). "Low thermal inertias of icy planetary surfaces: Evidence for amorphous ice?" *Astronomy & Astrophysics* Vol. 588. DOI: 10.1051/0004-6361/201527625.

Greeley, R. et al. (2004). "Geology of Europa". *Jupiter: The Planet, Satellites and Magnetosphere*. Ed. by F. Bagenal et al. Cambridge University Press.

Greeley, R. et al. (2000). "Galileo views of the geology of Callisto". *Planetary and Space Science* Vol. 48, No. 9. DOI: 10.1016/S0032-0633(00)00050-7.

Greeley, R. et al. (2001). "Geology of Lofn Crater, Callisto". *Journal of Geophysical Research: Planets* Vol. 106 (E2). DOI: 10.1029/2000JE001262.

Grundy, W. M. et al. (1999). "Near-Infrared Spectra of Icy Outer Solar System Surfaces: Remote Determination of H2O Ice Temperatures". *Icarus* Vol. 142, No. 2. DOI: 10.1006/icar.1999.6216.

Hayne, P. O. et al. (2017). "Global Regolith Thermophysical Properties of the Moon From the Diviner Lunar Radiometer Experiment: Lunar Regolith Thermophysical Properties". *Journal of Geophysical Research: Planets* Vol. 122, No. 12. DOI: 10.1002/2017JE005387.

Hibbitts, C. A. et al. (2000). "Distributions of CO_2 and SO_2 on the surface of Callisto". *Journal of Geophysical Research: Planets* Vol. 105 (E9). DOI: 10.1029/1999JE001101.

Howett, C. et al. (2011). "A high-amplitude thermal inertia anomaly of probable magnetospheric origin on Saturn's moon Mimas". *Icarus* Vol. 216, No. 1. DOI: 10.1016/j.icarus.2011.09.007.

Howett, C. et al. (2012). "PacMan returns: An electron-generated thermal anomaly on Tethys". *Icarus* Vol. 221, No. 2. DOI: 10.1016/j.icarus.2012.10.013.

Howett, C. et al. (2019). "Maps of Tethys' thermophysical properties". *Icarus* Vol. 321. DOI: 10.1016/j.icarus.2018.12.018.

Janssen, M. et al. (2016). "Titan's surface at 2.18-cm wavelength imaged by the Cassini RADAR radiometer: Results and interpretations through the first ten years of observation". *Icarus* Vol. 270. DOI: 10.1016/j.icarus.2015.09.027.

Johnson, T. V. et al. (1983). "Global multispectral mosaics of the icy Galilean satellites". *Journal of Geophysical Research: Solid Earth* Vol. 88 (B7). DOI: 10.1029/JB088iB07p05789.

Ligier, N. et al. (2020). "NEW INSIGHTS INTO CALLISTO'S SURFACE COMPOSITION WITH THE GROUND- BASED NEAR-INFRARED IMAGING SPECTROMETER SINFONI OF THE VLT."

McMullin, J. P. et al. (2007). "CASA Architecture and Applications". Vol. 376.

Moore, J. et al. (2004). "Callisto". *Jupiter: The Planet, Satellites and Magnetosphere*. Cambridge: Cambridge University Press.

Moreno, R. (2007). *Report on continuum measurements of Ganymede and Callisto with the IRAM–PdB interferometer : Application to flux calibration, Internal Memo*.

Morrison, D. et al. (1972). "Temperatures of Titan and the Galilean Satellites at 20 Microns". *The Astrophysical Journal* Vol. 173. DOI: 10.1086/180934.

Muders, D. et al. (2014). "The ALMA Pipeline". *Astronomical Data Analysis Software and Systems XXIII*. Ed. by N. Manset et al. Vol. 485. San Francisco, CA.

Muhleman, D. O. et al. (1986). "Precise VLA positions and flux-density measurements of the Jupiter system." *The Astronomical Journal* Vol. 92. DOI: 10.1086/114279.

Muhleman, D. O. et al. (1991). "Observations of Mars, Uranus, Neptune, Io, Europa, Ganymede, and Callisto at a wavelength of 2.66 mm". *Icarus* Vol. 92. DOI: 10.1016/0019-1035(91)90050-4.

Mura, A. et al. (2020). "Infrared observations of Io from Juno". *Icarus* Vol. 341. DOI: 10.1016/j.icarus.2019.113607.

Pappalardo, R. et al. (2004). "Ganymede". *Jupiter: The Planet, Satellites and Magnetosphere*. Ed. by F. Bagenal et al. Cambridge University Press.

Pauliny-Toth, I. I. K. et al. (1974). "The Brightness Temperatures of Ganymede and Callisto at 2.8 CM Wavelength". *Astronomy and Astrophysics, Vol. 34, p. 129 (1974)* Vol. 34.

Pauliny-Toth, I. I. K. et al. (1977). "Observations of Ganymede and Callisto at 1.3 cm wavelength." *Astronomy and Astrophysics* Vol. 58, No. 3.

Rau, U. et al. (2011). "A multi-scale multi-frequency deconvolution algorithm for synthesis imaging in radio interferometry". *Astronomy & Astrophysics* Vol. 532. DOI: 10.1051/0004-6361/201117104.

Sault, R. J. et al. (1994). "Multi-frequency synthesis techniques in radio interferometric imaging." *Astronomy and Astrophysics Supplement Series* Vol. 108.

Schaible, M. J. et al. (2017). "High energy electron sintering of icy regoliths: Formation of the PacMan thermal anomalies on the icy Saturnian moons". *Icarus* Vol. 285. DOI: 10.1016/j.icarus.2016.08.033.

Schenk, P. et al. (2011). "Plasma, plumes and rings: Saturn system dynamics as recorded in global color patterns on its midsize icy satellites". *Icarus, Volume 211, Issue 1, p. 740-757.* Vol. 211, No. 1. DOI: 10.1016/j.icarus.2010.08.016.

Schenk, P. M. (1995). "The geology of Callisto". *Journal of Geophysical Research: Planets* Vol. 100 (E9). DOI: 10.1029/95JE01855.

Schenk, P. M. (2002). "Thickness constraints on the icy shells of the galilean satellites from a comparison of crater shapes". *Nature* Vol. 417, No. 6887. DOI: 10.1038/417419a.

Spencer, J. R. (1987). "THE SURFACES OF EUROPA, GANYMEDE, AND CALLISTO: AN INVESTIGATION USING VOYAGER IRIS THERMAL INFRARED SPECTRA (JUPITER)." PhD thesis. University of Arizona.

Thelen, A. (2023). "Mapping Europa's Thermal Properties with ALMA." *LPI Contrib. No. 2806*. In collab. with K. de Kleer et al.

Thompson, D. T. et al. (1992). "Photoelectric photometry of Europa and Callisto 1976–1991". *Journal of Geophysical Research* Vol. 97 (E9). DOI: 10.1029/92JE01399.

Trumbo, S. K. et al. (2017). "ALMA Thermal Observations of a Proposed Plume Source Region on Europa". *The Astronomical Journal* Vol. 154, No. 4. DOI: 10.3847/1538-3881/aa8769.

Trumbo, S. K. et al. (2018). "ALMA Thermal Observations of Europa". *The Astronomical Journal* Vol. 156, No. 4. DOI: 10.3847/1538-3881/aada87.

Ulich, B. L. (1981). "Millimeter-wavelength continuum calibration sources." *The Astronomical Journal* Vol. 86. DOI: 10.1086/113046.

Ulich, B. L. et al. (1976). "Observations of Ganymede, Callisto, Ceres, Uranus, and Neptune at 3.33 mm wavelength". *Icarus* Vol. 27, No. 2. DOI: 10.1016/0019-1035(76)90001-4.

Ulich, B. L. et al. (1984). "Planetary observations at a wavelength of 1.32 mm". *Icarus* Vol. 60, No. 3. DOI: 10.1016/0019-1035(84)90166-0.

Zimmer, C. (2000). "Subsurface Oceans on Europa and Callisto: Constraints from Galileo Magnetometer Observations". *Icarus* Vol. 147, No. 2. DOI: 10.1006/icar.2000.6456.

Chapter 3

A MULTI-FREQUENCY GLOBAL VIEW OF CALLISTO'S THERMAL PROPERTIES FROM ALMA

The content of this chapter was adapted from the following article:

Camarca, M., K. de Kleer, B. Butler, A. Thelen, C. Meyer, A. B. Akins, I. de Pater, and M. A. Gurwell (submitted). "A multi-frequency global view of Callisto's thermal properties from ALMA". *Planetary Science Journal*. Submitted.

Abstract

We present thermal observations of Callisto's leading and trailing hemispheres obtained using the Atacama Large Millimeter/submillimeter Array (ALMA) at 0.87 mm (343 GHz), 1.3 mm (233 GHz), and 3 mm (97 GHz). The angular resolution achieved for these observations ranged from 0.″09-0.″24, corresponding to ∼420-1100 km at Callisto. Global surface properties were derived from the observations using a thermophysical model (de Kleer et al., 2021a) constrained by spacecraft data. We find that Callisto's millimeter emissivities are high, with representative values of 0.85-0.97, compared to 0.75-0.85 for Europa and Ganymede at these wavelengths. It is clear that models parameterized by a single thermal inertia are not sufficient to model Callisto's thermal emission, and clearly deviate from the temperature distributions in the data in systematic ways. Rather, more complex models that adopt either two thermal inertia components or that treat electrical skin depth as a free parameter fit the data more accurately than single thermal inertia models. Residuals from the global best-fit models reveal thermal anomalies; in particular, brightness temperatures that are locally 3-5 K colder than surrounding terrain are associated with impact craters. We identify the Valhalla impact basin and a suite of large craters, including Lofn, as key cold anomalies ($\sim 3-5$ K) and geologic features of interest in these data. These data provide context for Callisto JWST results (Cartwright et al., 2024) as well as the other ALMA Galilean moon observations (de Kleer et al., 2021a; Trumbo et al., 2018; Trumbo et al., 2017; Thelen et al., 2024), and may be useful ground-based context for upcoming Galilean satellite missions (JUICE, Europa Clipper).

3.1 Introduction

Among the solar system's rich portfolio of icy moons, Callisto stands out by token of its remarkably timeworn and ancient surface. With terrains as old as >4 billion years (Zahnle et al., 1998), Callisto reigns as the geologically quiescent endmember of the Galilean satellites. Like the other icy Galilean moons, Callisto nominally bears a liquid water subsurface ocean (Zimmer, 2000; Khurana et al., 1998; Kivelson et al., 1999; Saur et al., 2010), but unlike its icy siblings, Callisto does not appear to host any crustal recycling mechanisms. At present, there is little to no evidence for any volcanism, tectonics, or other surface-interior interactions (Moore et al., 2004; Greeley et al., 2000). Instead, Callisto's geology is dominated by a collection of craters and their evolved ruins. At the global scale, large multi-ring impact basins such as Valhalla (D ~3800 km) and Asgard (D ~1400 km) located on the leading hemisphere are the dominant geologic units on this D ~4820 km moon. At the finer scales, high-resolution images obtained by the Galileo spacecraft revealed that a dark material blankets the surface (Moore et al., 2004). Explanations for the origin of Callisto's dark material include dust infall from the irregular Jovian satellites (e.g., Bottke et al., 2013), reminiscent of how Iapetus obtained its dark leading hemisphere, and sublimation/erosional processes creating a lag deposit (Moore et al., 2004). However, the balance between exogenic and endogenic origins for this material remains poorly understood. As one of the solar system's best long-term records of impact bombardment and its largest geologically inactive moon, Callisto is the ideal target for understanding near purely exogenic surface sculpting.

The passive thermal emission from a surface provides information on surface properties, and hence how a planetary object has evolved through interactions with its external environment. For icy, airless satellites such as Callisto, the distribution of surface heat emission is primarily controlled by material properties such as the thermal inertia Γ (units of J m^{-2} K^{-1} $s^{-1/2}$ are assumed throughout) and emissivity ϵ (Ferrari, 2018). Pinpointing how these material properties vary spatially across a surface, along with the magnitude of their variation, can help discriminate between the effect of endogenic and exogenic surface processes. For example, thermal emission measurements of the Saturnian moons Mimas and Tethys acquired with Cassini's Composite Infrared Spectrometer (CIRS) demonstrated there is high thermal-inertia material concentrated at the apex of their leading hemispheres, which suggests that the Saturnian particle environment is capable of changing the grain properties of these moons, for example through sintering (Howett et al., 2011; Howett et al., 2019; Howett et al., 2012). In the Jovian system at radio wavelengths, observations

of Europa by Trumbo et al. (2017) and Trumbo et al. (2018) using the Atacama Large Millimeter/submillimeter Array (ALMA) showed that a purported endogenic hot spot (Sparks et al., 2017) invoked to explain Galileo PPR data (Spencer et al., 1999) could be straightforwardly interpreted as a region of local high thermal inertia. These examples emphasize the usefulness of global or near global scale maps of planetary thermal emission. Depending on the observation wavelength used, material properties can be sensed in the uppermost surface via infrared measurements, or in the near-subsurface layers via millimeter/submillimeter measurements. A benefit of probing subsurface layers is that such observations bypass the most heavily processed surface layers.

Space-based thermal infrared observations of Callisto come from the Voyager Infrared Interferometer Spectrometer and Radiometer (IRIS) and Galileo PPR instruments. Based on eclipse cooling curves, Spencer (1987b) suggested that Callisto's surface is not thermally uniform, with the best-fit model invoking a thin (mm thick) $\Gamma = 15$ component overlaying a $\Gamma = 300$ component. At a wavelength of $\sim$20 μm, the disk-integrated temperature was measured to be 158 K (Morrison et al., 1972; Moore et al., 2004), while at $\sim$10 μm temperatures of $\sim$140-150 K were reported by de Pater et al. (2021). A measurement of the H_2O ice surface temperature derived from spectral features is somewhat lower at 115 K, indicating that the high-albedo ice-rich regions are colder than the average surface (Grundy et al., 1999). Across the radio wavelength regime, disk-averaged brightness temperatures range from $\sim$135 K in the submillimeter (de Pater et al., 1989) down to $\sim$90-100 K in the centimeter (Pauliny-Toth et al., 1974; Muhleman et al., 1986; Butler, 2012; Berge et al., 1975; de Pater et al., 1984), consistent with decreasing temperature with depth over the upper $\sim$meters.

At present, global, spatially-resolved millimeter/submillimeter thermal property maps only exist for Ganymede (e.g., de Kleer et al., 2021a) and Europa (Trumbo et al., 2017; Trumbo et al., 2018; Thelen et al., 2024). Recently, Camarca et al. (2023) published a spatially resolved 343 GHz thermal image of Callisto's leading hemisphere as observed with ALMA. In that image, the Valhalla impact basin can be identified as terrain $\sim$3 K colder than model predictions, and was accompanied by low-latitude warm regions possibly linked to meteorite bombardment. However, like with the other icy Galilean satellites, a global map acquired at multiple wavelengths is needed to identify the extent to which leading/trailing hemisphere differences exist in the millimeter, to determine whether thermal anomalies are tethered to local

geologic terrains, and how the thermal emission profiles of these terrains varies with depth.

In this work, we present the first global set of high-resolution thermal observations of Callisto using ALMA by mapping the leading and trailing hemispheres at 3 mm (97 GHz), 1.3 mm (233 GHz), and 0.87 mm (343 GHz). Section 3.2 describes the observations, data analysis, and flux density calibration. Section 3.3 details the thermophysical model used to interpret the data and describes how surface properties are derived. Section 3.4 presents the results and interpretation of the thermophysical modeling analysis. Section 3.5 summarizes the conclusions of this work.

3.2 Methods

Observations

Observations of Callisto were obtained using ALMA, located on the Chajnantor plateau in the Atacama desert of northern Chile. The main ALMA array is composed of 50 12-m radio/sub-mm antennas linked via a correlator to function as an interferometer, where each pair of antennas samples the Fourier transform of the sky brightness distribution. The data product delivered by ALMA is a measurement set (MS) comprising "complex visibilities", or the amplitudes and phases of the cross-correlated signals generated by each pair of antennas, which can be used to reconstruct the sky brightness distribution using image inversion and deconvolution techniques (see Thompson et al., 2017, and references therein). Since the main array antennas can be distributed across up to 16 km of the plateau, ALMA is capable of achieving much higher angular resolution than is possible using a single antenna at similar wavelengths. The resolutions achieved by ALMA, in combination with its high sensitivity and spectral coverage, enable thermal mapping of the Galilean satellites and other small bodies in the solar system.

We present seven observations of Callisto's leading and trailing hemispheres obtained between 2016 October 24 and 2017 October 3 (Program 2016.1.00691.S, P.I. de Kleer). Each hemisphere has spectral coverage in three receiver bands with central frequencies of 97 GHz (∼3 mm; Band 3), 233 GHz (∼1.3 mm; Band 6), and 343 GHz (∼0.87 mm; Band 7). The Band 6 trailing hemisphere was first observed on 2016 October 25, however the synthesized beam ($0\farcs21 \times 0\farcs29$) did not meet the resolution requirements. A corrected observation of Callisto was obtained at a similar viewing geometry on 2017 July 4 with a satisfactory synthesized beam ($0\farcs12 \times 0\farcs20$). Given that the spatial resolution of the first observation is relatively

poor, we present the calibrated image and disk-averaged quantities, but do not include it in the thermal model analysis. The angular resolution of the remaining six observations ranges from ∼0.″09-0.″24. At the distance of the satellite, these angular resolutions correspond to spatial resolutions of ∼420 to 730 km according to the beam minor axis and scales of ∼700 to 1100 km on the beam major axis, suitable for mapping Callisto's largest impact basins and large-scale terrains. Within each receiver band, spectral coverage spanned four spectral windows with collective bandwidth of ∼8 GHz and on-source integration times of ∼121 s for Bands 6 and 7 to ∼300 s for the Band 3 observations. Calibration for array pointing, flux density, bandpass response, and phase were obtained via observations of quasars J1256–0547, J1232–0224, J1336-0829, and J1517-2422.

Table 3.1: Observing Parameters and Derived Quantities

Date	Time	Ang. Diam.	Beam	Beam P.A.	Sub-Obs. Lon	Sub-Obs. Lat	Phase Ang.	ν	λ	F_ν	T_b	Image rms	
(UT)	(UT)	(arcsec)	(arcsec)	(deg)	(°W)	(°N)	(deg)	(GHz)	(mm)	(Jy)	(K)	(mJy/beam)	(K)
2016 Nov 01	15:07	1.05	0.16×0.19	−68.6	50	−2.2	4.9	343	0.87	8.03 ± 0.40	116 ± 5	0.585	0.20
2016 Oct 24	11:26	1.05	0.11×0.24	66.7	236	−2.2	3.9	343	0.87	7.43 ± 0.37	109 ± 5	0.532	0.21
2017 Jul 09	00:41	1.23	0.10×0.23	−63.1	27	−2.5	10.7	233	1.3	4.81 ± 0.24	109 ± 5	0.406	0.41
2017 Jul 04	20:49	1.24	0.12×0.20	−83.2	297	−2.5	10.7	233	1.3	5.24 ± 0.26	115 ± 6	0.575	0.53
2016 Oct 25*	12:07	1.04	0.21×0.29	60.8	258	−2.2	4.0	233	1.3	3.38 ± 0.17	107 ± 5	0.610	0.22
2017 Oct 03	19:33	1.04	0.09×0.15	69.5	84	−2.6	3.2	97	3	0.62 ± 0.03	110 ± 5	0.193	1.7
2017 Sep 06	15:34	1.07	0.11×0.23	62.0	224	−2.5	6.7	97	3	0.64 ± 0.03	106 ± 5	0.184	0.96

The F_ν and T_b columns refer to the disk-integrated flux density and the disk-averaged brightness temperature. The Beam P.A. column refers to the beam position angle. The date marked with an * denotes a Band 6 trailing hemisphere observation acquired with a synthesized beam size larger than the proposal requirements. We opt to present the calibrated image for this poor resolution band 6 observation, but do not include it in the thermal modeling.

Data Analysis

To process the MS, we followed established routines for calibrating and imaging solar system interferometric data (e.g., see Thelen et al. 2024; Camarca et al. 2023; de Kleer et al. 2021a), summarized below. For a review of the interferometric observation and imaging of Solar System objects, see Butler et al. (1999).

The imaging routine for these datasets consisted of an iterative cycle of imaging and self-calibration. The use of self-calibration to address phase fluctuations typically yields higher signal-to-noise images for Solar System objects than those generated directly by the ALMA pipeline. Self-calibration is effective for objects like the Galilean satellites because they have easily modeled shapes (disks) and have sufficient flux density (high SNR). For a more detailed explanation of this process, see Brogan et al. (2018). We conducted our imaging using the Common Astronomy Software Application (CASA) package (Team et al., 2022). In each band, we integrated the signal over the entire 8 GHz of bandwidth using multi-frequency synthesis (Sault et al., 1994). Our phase-only self-calibration using CASA followed as such: for the first round of imaging, a Lambertian disk scaled to the size and brightness temperature of Callisto was used as a `startmodel` for the `tclean` task (Rau et al., 2011); no additional clean components were added. Next, the complex antenna-based gain corrections were calculated using the CASA `gaincal` task on an interval spanning the full integration time and then applied using `applycal`. Then, the corrected visibilities were imaged again adopting a shallow clean, using the previous `tclean` output model as the `startmodel`. This cycle of cleaning and computing gains continued down to an interval of 2 s; at shorter time intervals the image SNR ceased to substantially improve. For `tclean` parameters, we adopted a Briggs weighting scheme (Briggs, 1995) with a robust parameter of 0.0, and used the "Clark" deconvolver (Clark, 1980). The dimensions of the final clean beams are included in Table 3.1. The rms (root-mean-square) noise of the final images (measured from a non-source region of the image products) is reported, with values ranging from about 0.20-1.7 K. Our final calibrated images are presented in Fig. 3.1.

After self-calibrating the data, we derived the disk-integrated flux density F_ν using a fit to the visibilities. We report F_ν quantities from these fits rather than from the images because the visibilities are the more direct data product. Reporting F_ν is useful for placing our results in context with previous radio observations of Callisto that are largely spatially unresolved. The visibilities were fit with Bessel functions using the CASA task `uvmodelfit` assuming a uniform disk model, fitting to all

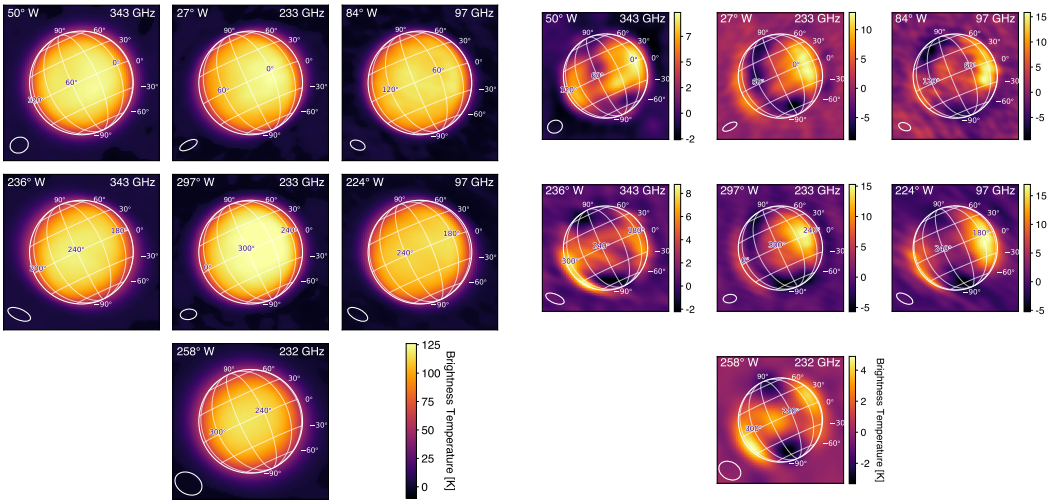

Figure 3.1: *Left*: Calibrated ALMA images of Callisto. *Right:* Residuals obtained by subtracting Lambertian disks from images on the left to highlight differences in T_b across the disk, with the unit being K for all panels. In both panels, the ellipse in the lower left corner represents the FWHM (full-width at half-maximum) of the synthesized ALMA beam, which is the resolution element. The latitude/longitude grid is spaced at 30° increments. The images are all scaled such that the horizontal and vertical axes each span -3500 km to +3500 km on a side.

spectral windows, and by excluding baselines >200 m for an optimal fit, as the longer baselines are sensitive to the variations across the disk rather than just the disk-integrated flux density. The final disk-averaged brightness temperature (T_b) was calculated by inverting the following equation (see Appendix A in de Pater et al. 2014):

$$F_\nu = 10^{26} \frac{\pi R_C^2}{206265^2} \frac{2h\nu^3}{c^2} \times \left[\frac{1}{e^{h\nu/k_b T_b} - 1} - \frac{1}{e^{h\nu/k_b T_{cmb}} - 1} \right] \tag{3.1}$$

where F_ν is the disk-integrated flux density in Janskys, R_C is the radius of Callisto in arcseconds, the quantity 206265 is the number of arcseconds in a radian, and, in SI units, h is Planck's constant, c is the speed of light, ν is the observation frequency, k_b is the Boltzmann constant, and T_{cmb} is the cosmic microwave background (2.7 K). The final T_b measurements are presented in Table 3.1. The uncertainties in the final T_b incorporate flux density scale calibration errors, which were parameterized by a 5% error of the total flux density, and the visibility fitting errors.

ALMA Pipeline Flux Density Calibration Check

The ALMA pipeline uses quasars to calibrate the flux density of the science target data. Given that quasars are variable sources, it is necessary to verify that the ALMA pipeline has used the most complete information for setting the visibility amplitude scale. Sometimes, a manual correction to the flux density calibration scale is required (e.g, Trumbo et al. 2018; de Kleer et al. 2021a; Thelen et al. 2024; de Pater et al. 2019; Francis et al. 2020). For all of our observations, the quasar J1256-0547 was used for flux density scale calibration. To verify its flux density, measurements of the quasar taken between 2016 September and 2017 November at ALMA Bands 3, 6, and 7 were downloaded from the ALMA calibrator catalogue. These time-resolved measurements were compared to the `setjy` visibility amplitude scale set by the pipeline scripts for each day of our observations. Our inspection of a year-long range of J1256-0547 observations demonstrated consistency with the values adopted by the pipeline, and we did not make any manual corrections to the flux density scale calibration.

3.3 Thermophysical Model

We model the data using a thermophysical model previously used for ALMA observations of the Galilean satellites, which is described in detail in Section 3 of de Kleer et al. (2021a), with key points reiterated by Camarca et al. (2023) and Thelen et al. (2024). In this work, we summarize the main points.

The output of self-calibrating and imaging the ALMA visibilities is a map of flux density per beam that can be converted to brightness temperature across Callisto's disk (Fig. 3.1). Because these observations were acquired at radio wavelengths and are therefore sensitive to subsurface emission, a thermophysical model that incorporates radiative transfer is needed (Mitchell et al., 1994). The model described by de Kleer et al. (2021a) treats the transport of heat via conduction and radiation through the subsurface. For each latitude and longitude on Callisto, the model constructs a time-dependent and depth-dependent temperature profile. This temperature profile is prescribed by solving the 1D heat equation, given by:

$$\rho c_p \frac{\partial T}{\partial t} = \frac{\partial}{\partial z}\left(k \frac{\partial T}{\partial z}\right) \tag{3.2}$$

where t is time, z is depth, ρ is the density, c_p is the heat capacity, T is the temperature, and k is the thermal conductivity. For solving this differential equation, the lower boundary condition is set by the assumption of zero heat flow at depth, and the upper boundary condition is set by solar insolation at the distance of Callisto

based on spatially varying bond albedo (we use the same spacecraft-data constrained albedo map published by Camarca et al. 2023). The model was evolved over ∼15 Callisto days (1 Callisto day = 16.69 Earth days) in time steps of at least 1/500 of a day to allow for equilibration, and was run from the surface down to to several thermal skin depths below the surface. The model is then compared to the data to determine the best-fit global thermal inertia and emissivity. The reason these fits are global, rather than local, is because an individual ALMA observation is a "snapshot" in time of Callisto's thermal emission profile. Our observations are spatially resolved, meaning we obtain the temperature at many locations across Callisto. But for an individual location, we only retrieve that temperature for a single local time. As such, we refrain from attempting to fit local properties on Callisto because we do not observe individual locations at multiple times of day. However, under the assumption that the thermal properties are constant across the disk, we can use the fact that the local time at each individual location is different to build a global thermal emission model. In other words, we interpret spatial differences in the thermal emission as time-of-day differences. Additionally, we note that our modeling approach differs from de Kleer et al. (2021a) in that the two free parameters in our model are the thermal inertia and emissivity. In de Kleer et al. (2021b), the porosity is the primary free parameter, from which both thermophysical and electrical properties are calculated self-consistently assuming a grain size and dust fraction. In our implementation, the electrical properties are instead set assuming pure water ice, but are allowed to vary via a free scale factor. Similarly, in our implementation the thermal inertia is permitted to vary independently of the electrical properties, and without any assumptions about the underlying porosity, grain size, or composition. A final difference is that we fit the model parameters of each frequency and hemisphere independently rather than jointly fitting all data within a given frequency or longitude as done in de Kleer et al. (2021a). The motivation for the different implementation was that an approach in which all data within each frequency were jointly fit with a model that requires parameters to be physically self-consistent found a poor fit to the Callisto data. We therefore opted to fit each dataset independently and increased the number of independently-tunable parameters in order to attempt to fit the data. The fact that the self-consistent model implementation was not able to fit the data indicates that some physics may be missing in the model that is relevant to Callisto but not Ganymede or Europa.

As described by Camarca et al. (2023), Callisto's thermal emission at millimeter wavelengths is difficult to fit with a model that assumes a uniform thermal iner-

tia. Therefore, after testing single-Γ fits, we turned to testing two-Γ models using a procedure identical to that described in Section 3.1 of Camarca et al. (2023). This approach is an expanded application of the de Kleer et al. (2021a) model. In summary, we implemented the two-Γ approach by generating a grid of "lower" thermal inertia models (Γ = 15-400) and "higher" thermal inertia models (Γ = 500-2000). Pairs of low-Γ and high-Γ models are linearly added at variable relative percentages prior to convolution with the ALMA beam. At the point that the models are added, they are in units of Jy, not K. This task produced models that simulate materials at two thermal inertias mixed spatially below the resolution of the data. Each final two-Γ mixture model is then compared to the data. The exploration of multiple thermal inertias for Callisto's (sub)surface emission in this work as well as by Camarca et al. (2023) is motivated in part by prior infrared results from Spencer (1987b), which showed that a single thermal inertia model is not sufficient to reproduce Callisto's infrared emission. Importantly, the Spencer (1987b) treatment uses two vertically stratified layers, whereas our model treatment more closely matches a spatially inhomogeneous model.

A feature of the current work is an exploration of the effect of varying the electrical skin depth on the best-fit models to Callisto. The electrical skin depth (δ_{elec}) is the material property that sets the sensitivity of an observation of wavelength λ to thermal emission at depth z below the surface. It is defined as:

$$\delta_{elec} = \frac{\lambda}{4\pi\kappa} \tag{3.3}$$

where λ is the observation wavelength, and κ is the imaginary part of the complex refractive index, $\widetilde{\eta} = \eta + i\kappa$. For a detailed description of how δ_{elec} is implemented in the model, we refer the reader to Section 3.2 of de Kleer et al. (2021a). In our model implementation, δ_{elec} is computed using a κ value that has temperature and frequency dependence appropriate for pure water ice. However, for this work we tested varying δ_{elec} by an absorptivity scaling factor a_{scale} that is constant in wavelength and in temperature:

$$\delta_{elec} = \frac{\lambda}{4\pi(a_{scale}\kappa)} \tag{3.4}$$

where the tested values of a_{scale} ranged from 0.25 to 12.5, and represent the factor by which δ_{elec} is decreased. This range is informed by values obtained with similar tests of scaling the δ_{elec} for interpreting Europa ALMA data performed by Thelen et al. (2024).

The goodness of fit for the thermophysical models was determined using a cost function. The adopted cost function differs from a simple χ^2 through an adjustment that takes into account the fact that the number of independent datapoints is smaller than the number of pixels by an amount equal to the number of pixels per ALMA beam. This approach for estimating goodness-of-fit has been used in prior analyses, including de Kleer et al. (2021b) and Cambioni et al. (2019). For each model and observation, we calculated the following:

$$\chi^2 = \frac{1}{N_{pxl} - N_{param}} \times \sum_{j=1}^{N_{pxl}^{j}} (\frac{M_j - D_j}{\sigma})^2 \tag{3.5}$$

where N_{pxl} is the number of pixels on Callisto's disk, N_{par} is the number of model parameters (e.g., 2 for a single Γ and e), Models that satisfied the relation $\chi^2 < \chi^2_{min}(1 + \sqrt{2/(N_{dat} - N_{par})}$, where N_{dat} is the number of individual data points, were considered acceptable (Press et al., 1986; Hanuš et al., 2015). For our analysis, we treat N_{dat} as the number of ALMA resolution elements on-disk in a given observation, rather than the number of individual pixels on-disk; this results in a more conservative estimate of model uncertainties. To calculate N_{dat}, we divide the total number of pixels on-disk in a given observation by the number of pixels per ALMA beam. For additional details on applying the cost function to ALMA data, see Section 3.4 of de Kleer et al. (2021b).

For ease of readability, we implement a naming scheme into this work. The thermal model approaches used herein will be referred to with a capital M, with subscripts denoting the key variables of interest. M_Γ will refer to the single-Γ treatment, $M_{\Gamma,\Gamma}$ to the two-Γ treatment, and $M_{\Gamma,\delta}$ to the treatment using a single Γ and variable δ_{elec}.

3.4 Results & Discussion

We present surface properties inferred from ALMA images of Callisto obtained at ALMA Bands 3, 6, and 7, with corresponding wavelengths/frequencies of 3 mm (97 GHz), 1 mm (233 GHz), and 0.87 mm (343 GHz), respectively. These observations provide coverage of both Callisto's leading and trailing hemispheres. Along with the calibrated images shown in Fig. 3.1, we present best-fit thermophysical properties, as well as the residual maps produced by subtracting the corresponding best-fit models from the data to identify spatial variations in thermal properties. In Section 2.4, we present disk-averaged T_b measurements, and place our results in context with past thermal wavelength observations. In Sections 3.4 and 3.4, we present the

best-fit thermal properties and describe global trends in the spatial distribution of thermal emission. Lastly, in Section 3.4 we detail the connections between regional thermal signatures and the local geology.

Disk-Averaged Brightness Temperature

Because most past radio observations of Callisto are not spatially resolved, it is useful to report disk-integrated quantities to place our results in context. In Table 3.1, we report the disk-integrated flux densities F_ν in Jy and corresponding disk-averaged brightness temperatures T_b in K for the leading and trailing hemispheres at each frequency. In Fig. 3.2, we place these disk-averaged measurements in context with past measurements obtained for Callisto over the cm to sub-mm range. We find the F_ν span ∼0.62-8.03 Jy across the wavelength range of 3 to 0.87 mm, corresponding to T_b values in the range of ∼106-116 K. Consistent with what was previously reported by Camarca et al. (2023) for the 0.87 mm leading hemisphere measurement, the additional ALMA measurements presented here agree well with past work. However, the 1.3 mm measurement by Ulich et al. (1984) of T_b= 149 ± 17 K is about ∼35 K higher than other 1.3 mm measurements, including those presented in this work as well as those by Gurwell and Moullet (personal communication) and Moreno (2007). The measurement of Ganymede by Ulich et al. (1984) also disagrees with other measurements: in Fig. 6 of de Kleer et al. (2021a), the 1.3 mm T_b reported by Ulich et al. (1984) is ∼115 K, while nearby ALMA measurements (de Kleer et al., 2021a) and IRAM–PdB (Moreno, 2007) fall within the 80-100 K range (for Ganymede, the error bars of Ulich et al. (1984)'s T_b overlap with the neighboring measurements; for Callisto, the error is not close to overlap).

There is a general trend of decreasing T_b with increasing wavelength, beginning with values near 150 K in the infrared near 10 μm that fall off to 90-100 K in the 1-10 cm regime (Fig. 3.2). The depression of T_b values with increasing wavelength is likely due to the fact that longer wavelengths sense deeper subsurface layers where 1) the diurnal wave is attenuated and 2) higher thermal inertia (i.e., denser, more compacted) materials are expected to be present. In addition, there is drop in emissivity at millimeter wavelengths that is known to be linked to the optical properties of ice. At longer wavelengths, water ice becomes much more transparent than it is in the far infrared due to a decrease in the value of the imaginary part of the complex index of refraction. (e.g., Warren 2019). This behavior is also well documented in observations of the icy particles of Saturn's rings, for example, which exhibit a drop-off in emissivity around 0.2 mm (Spilker et al., 2005; Spilker et al., 2018). We find the T_b

measurements for Callisto's leading and trailing hemisphere at a given frequency are the same within uncertainties, a result that differs from hemispheric disparities observed in Europa ALMA and Submillimeter Array (SMA) observations (see Thelen et al. 2024 and references therein).

Emissivity

Nearly all of the thermal models that provide acceptable fits to the Callisto data have high millimeter emissivities (ϵ), with values ranging from ϵ ~0.85-0.97. As shown in Figs. 3.3, 3.4, and 3.5, Callisto's high emissivities persist across the 97-343 GHz range, across hemispheres, and across thermophysical model treatments. Even for observations that yield unconstrained Γ (e.g., the single-Γ treatment of the 97 GHz data), the derived emissivities remain high and overlap with the emissivity derived from observations that produced a more well-constrained Γ, demonstrating the robustness of these emissivity values. Prior measurements of Callisto's emissivity in other wavelength regimes also returned high values. As highlighted by Moore et al. (2004), emissivities near unity in the microwave were inferred from observations at 0.355 mm by de Pater et al. (1989) and beyond 2 mm by Muhleman et al. (1991). In the infrared, Spencer (1987b) found that Callisto's emissivity approached values up to around 0.92-0.94 in Voyager data.

These measurements of ϵ for Callisto can be placed in context with values derived for the other Galilean moons. A direct ϵ comparison is available via published ALMA observations of Ganymede and Europa. For Europa, Trumbo et al. (2018) reported $\epsilon = 0.75$ at 233 GHz based on thermal model treatment of just surface emission, while Thelen et al. (2024) reported values of $\epsilon = 0.80$-0.85 across frequencies of 97.5, 233, and 343.5 GHz after accounting for subsurface emission. For Ganymede, Spencer (1987a) found a high infrared emissivity of 0.94, while de Kleer et al. (2021a) reported ϵ = 0.75-0.78 in the millimeter. To summarize, Callisto's emissivities are consistently higher than its icy Galilean siblings across our frequency coverage, which is likely a consequence of the fact that Callisto's surface is not as abundantly ice-rich as its Galilean siblings and that the emissivity of ice is lower than rock at millimeter wavelengths (Hewison et al., 1999; Yan et al., 2008; de Kleer et al., 2021b).

Global Thermal Properties

We derived global thermal properties for Callisto by fitting a thermal model to the ALMA data using a suite of thermophysical modeling approaches, including single-

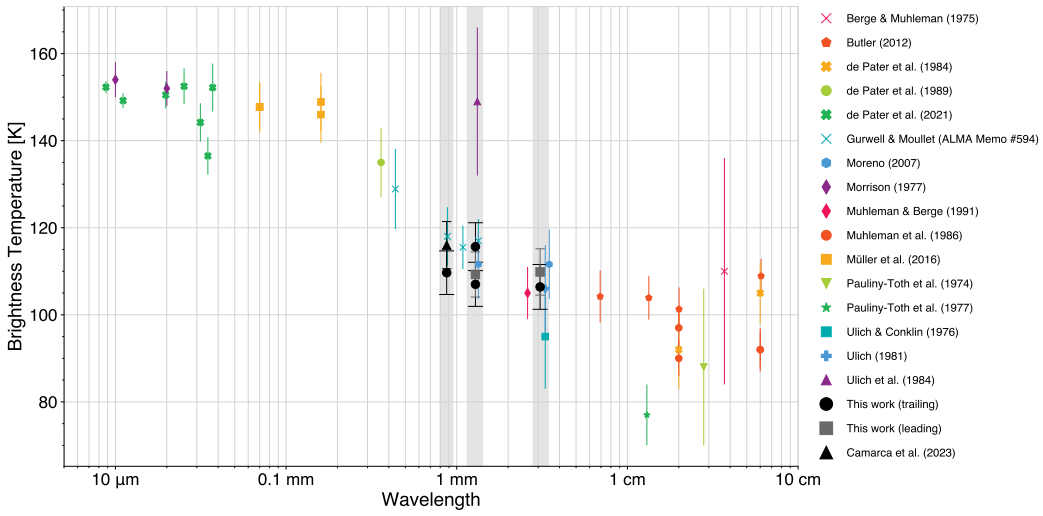

Figure 3.2: Summary of disk-averaged brightness temperature measurements for Callisto plotted as a function of wavelength. This plot is an update to the one shown in Camarca et al. (2023) including the additional ALMA data points presented here. Our measurements (black/gray points with capped error bars, highlighted in grey) agree with most neighboring data. Data in this plot are taken from: Berge et al. (1975), Butler (2012), de Pater et al. (1984), de Pater et al. (1989), and de Pater et al. (2021), Gurwell & Moullet (ALMA memo #594, Butler 2012), Moreno (2007), Morrison (1977), Muhleman et al. (1991), Muhleman et al. (1986), Müller et al. (2016), Pauliny-Toth et al. (1974) and Pauliny-Toth et al. (1977), Ulich et al. (1976), Ulich (1981), and Ulich et al. (1984).

Γ and two-Γ models, variations to the electrical skin depth, and the implementation of refraction using Hapke and Fresnel laws. We found most of the Callisto observations are not well-fit using models with a uniform thermal inertia across the satellite's surface, motivating the more complex approaches. The introduction of a secondary thermal inertia component and decreasing the electrical skin depth did improve the fit for a number of cases. In this section, we describe the outcomes of each individual modeling approach.

Single-Γ Results

As seen in the first row of Fig. 3.6, the data-minus-model residual images obtained by using a single-Γ approach (M_Γ) produced systematic features in the residuals from nearly every Callisto observation. For instance, the models usually failed to simultaneously fit the satellite disk center and the disk limb, with a typical model producing overly cold limbs and an overly warm disk center. The best-fit Γ and ϵ values are shown in Fig. 3.3. We find the emissivities inferred from M_Γ are consis-

tently high across all observations, with values generally above 0.90, although the range extends from 0.86 to 1.0 depending on the frequency band (values exceeding $\epsilon = 1$ were not permitted). Regarding the inferred Γ values, there is a large degree of variation between frequencies. The 343 GHz best-fit Γ ranges from about $\Gamma = 600$-1900, with no appreciable difference between the leading and trailing hemisphere. The 233 GHz data behave somewhat differently, with the leading hemisphere observation fit best by a much narrower range, $\Gamma = 100$-500, while the trailing hemisphere range of $\Gamma = 200$-1300 is wide compared to the 343 GHz data, albeit with a lower average value. The 97 GHz data are the most poorly constrained observations, although there are two separate ranges allowed: the first being $\Gamma = 100$-600 and the other being $\Gamma = 1200$-2000.

A poorly constrained Γ at 97 GHz is not surprising, given the 97 GHz data are sensitive to deeper subsurface layers than the 343 GHz and 233 GHz data. As described in Sec. 3.4, deeper subsurface layers experience more muted diurnal temperature fluctuations, which makes differentiating between models more difficult. A similar ALMA Band 3 result for Europa was reported by Thelen et al. (2024). Despite the lack of a constrained Γ, the 97 GHz trailing hemisphere observation is the only observation for which the M_Γ treatment does not result in image residuals that exhibit large-scale spatial systematics indicative that the model is not a good fit to the data (i.e., there is no obvious center of disk vs limb issue). Rather, the 97 GHz trailing residuals are more complex, with isolated regions of warm and cold terrains; these localized residuals will be discussed in Section 3.4.

Single-Γ and Variable δ_{elec} Results

We explored a variant of the M_Γ approach where we allowed variations to Γ and to the electrical skin depth δ_{elec} ($M_{\Gamma,\delta}$), which determines the subsurface depths that are responsible for the model emission at a given wavelength. The default electrical skin depth in the model corresponds to that of pure water ice. It depends on both temperature and frequency, but for the representative case of 233 GHz and 150 K, we calculate it is 65λ. The range of absorptivity scaling factors explored therefore corresponds to δ_{elec} in the range of $\sim$5-150λ. The low end of this range is representative of rocky regolith, while the upper end is representative of pure and porous ice (e.g., see Fig. 2 in de Kleer et al. 2021a and also de Kleer et al. 2021b). As shown in Fig. 3.4, we find that the model variables for the 233 GHz data are more tightly constrained than those of the 343 or 97 GHz data, which is consistent with the model

behavior found in the single-Γ approach. The direction of decreasing χ^2 for the models trends toward fractionally lower δ_{elec} values (higher values of a_{scale}). Nearly all of the models with the lowest individual χ^2 for a given observation adopted an absorptivity scaling factor of ∼10-12.5, which represents the upper bound of a_{scale} tested in the current work. Similarly, Thelen et al. (2024) found that the δ_{elec} required a scaling factor of order 10 to interpret Europa's thermal emission at 233 GHz.

For many models, allowing this parameter to vary provides an improvement over the M_Γ fits. As shown on the second row of Fig. 3.6, several model fits are greatly improved with the $M_{\Gamma,\delta}$ approach. The two observations most responsive to the $M_{\Gamma,\delta}$ treatment include the leading hemisphere 233 and 97 GHz images, with more modest improvements to the remaining observations. For example, the 233 and 97 GHz model residuals under the default M_Γ treatment are dominated by the warm disk centers and cold limbs described in the previous subsection. With the addition of δ_{elec} as a free parameter, the residuals are no longer dominated by large-scale spatial systematics but rather show localized residuals that are correlated with geologic features.

Two-Γ Results

We additionally modeled all of the observations using a two-Γ model ($M_{\Gamma,\Gamma}$), which Camarca et al. (2023) found to provide a better fit to Callisto ALMA data than M_Γ models. We show the best-fit $M_{\Gamma,\Gamma}$ residuals in the third row of Fig. 3.6. For some observations, the inclusion of a secondary thermal inertia component provided an improved fit over M_Γ. For example, the disk/limb fit problems for leading hemisphere 343 and 233 GHz images are muted using $M_{\Gamma,\Gamma}$. In the 343 GHz data, the $M_{\Gamma,\Gamma}$ approach greatly improved the ability of the model to match Callisto's cool limbs, especially the (geographic) eastern limb; additionally, the improved fit resulted in more prominent residual T_b signatures that can be linked with geologic terrain, i.e. the Valhalla impact basin. Similarly, in the 233 GHz leading hemisphere image, a cold spot co-located with Valhalla is not visible in the M_Γ residuals, but is visible with the improved $M_{\Gamma,\Gamma}$ residuals because it is no longer dominated by systematic residuals associated with a global model that is not a good match. By contrast, only modest improvement (or change) to the residuals is seen for the 97 GHz leading hemisphere data and the trailing hemisphere data across all frequency bands. For instance, the trailing hemisphere 343 GHz and 233 GHz $M_{\Gamma,\Gamma}$ residuals still bear the center-of-disk/limb fit systematics apparent in the M_Γ residuals, albeit

with smaller amplitude temperature deviations. The range of $M_{\Gamma,\Gamma}$ thermal inertia combinations that satisfied Eq. 3.5 for each observation are presented in Fig. 3.5. Generally, the Γ constraints for the 343 GHz data are better compared to the 233 GHz data. Like with the M_{Γ} modeling prescription, the 97 GHz models are very poorly constrained. Additionally, the distribution of the 97 GHz trailing hemisphere temperature residuals (i.e., the relative location of the hot and cold spots) is nearly identical to the M_{Γ} model. Collectively, these trends with frequency indicate that Γ is better constrained at higher frequencies because the diurnal temperature variations are larger due to the shallower depths sensed, while the temperature residuals observed at low frequencies are more robust to Γ. Although there are limitations to this approach, if high/low thermal inertia terrains are adjacent to each other at distances well below the resolution of an ALMA beam (hundreds of km), this is a reasonable approximation. An example of such terrains include the swaths of bright, icy peaks interspersed between Callisto's dark material blanket seen in high-resolution spacecraft images (Greeley et al., 2001; Moore et al., 2004).

Summary of Global Results

We find that a thermophysical model that adopts an approach more complex than just fitting for a single Γ and ϵ for the surface provide better fits to Callisto's thermal emission as measured at 97, 233, and 343 GHz. When the M_{Γ} approach is used, we find the best-fit values derived from M_{Γ} as organized by frequency are $\Gamma = 600$-1900, 100-1300, and unconstrained, for 343, 233, and 97 GHz respectively. However, modeling approaches that adopt either two-Γ components or treat the electrical skin depth δ_{elec} as a free parameter generally found a better fit, and in some cases resolved persistent large-scale spatial residuals untreated by the M_{Γ} approach. Using $M_{\Gamma,\delta}$, we find $\Gamma = 500$-2000, 300-600, and 50-2000 for 343, 233, and 97 GHz respectively. Application of the $M_{\Gamma,\Gamma}$ approach produced fits for the (lower, higher) components of Γ= (<100, unconstrained) for 233 GHz; Γ = (<50, >1200) for 343 GHz; and totally unconstrained for 97 GHz. The fact that Callisto's regolith appears to have a very high emissivity, with representative values ranging from ∼0.85-0.97 in our frequency regime, is consistent across all model treatments.

Regarding these Γ values, there is not a clear trend with subsurface depth. Both Fig. 3.3 and Fig. 3.5 demonstrate that the preferred thermal inertias appear higher for the 343 GHz data than the 233 GHz data, but there is overlap between the inferred values. Moreover, we do not constrain a difference in the value of the thermal proper-

ties between the leading and trailing hemispheres that is consistent across all model approaches. This is apparent in Fig. 3.3, 3.4, and 3.5, which shows that the thermal properties for a given frequency overlap between the two hemispheres. Lastly, the persistent inability of the modeling approaches to fix the large-scale warm/cold regions on the trailing hemisphere is suggestive that additional model physics may be required for those data. The fact that we do not constrain a difference in Callisto's thermal properties between 97-343 GHz leaves open the possibility that our ALMA observations have not bypassed the dark material blanket that globally covers Callisto. Estimates of the thickness of Callisto's dark material are up to many ∼meters to ∼10s of meters thick based on surface topography, including the smoothness of the surface at the 10 meter scale (Moore et al., 2004; Basilevsky et al., 2002). Therefore, it was not expected a priori that the ALMA data would bypass the dark material blanket, and the present modeling results appear consistent with this expectation. Altogether, the ALMA data may offer a lower bound for the dark material blanket that is not less than ∼10s of cm thick.

To place these Γ results in context with, we summarize results from ALMA observations of the other Galilean satellites. Using eclipse cooling data, de Pater et al. (2020) inferred Io's thermal inertia to be $\Gamma = 50$ based on infrared data, and around $\Gamma = 350$ based on millimeter observations. At 233 GHz, Trumbo et al. (2018) obtained $\Gamma = 95$ for Europa, with possible surface variations of $\Gamma = 40$-300. A comprehensive analysis of Europa at 97-345 GHz by Thelen et al. (2024) retrieved effective thermal inertias of $\Gamma = 50$–140, $\Gamma = 140$–180 for the leading and trailing hemispheres, respectively. The Ganymede observations by de Kleer et al. (2021a) at 343.5, 223, and 97.4 GHz yielded effective thermal inertias of $\Gamma = 450^{+300}_{-250}$, 350^{+350}_{-250}, and 750^{+200}_{-350} respectively. Although the thermal modeling procedure is not the same across all of these works, these findings, together with the results presented by Camarca et al. (2023), it appears there is some trend toward increasing thermal inertia with increasing distance from Jupiter (a trend also illustrated in Fig. 6 of Camarca et al. 2023).

Local Thermal Residuals

In the previous section, we outlined the global thermophysical properties we derived for Callisto. In this section, we describe thermal anomalies that may be tethered to the local geology. In these regions, the data do not agree with the global model, indicative of distinct thermal properties. For thermal anomalies that do not have an obvious geologic connection, we speculate on possible explanations within the

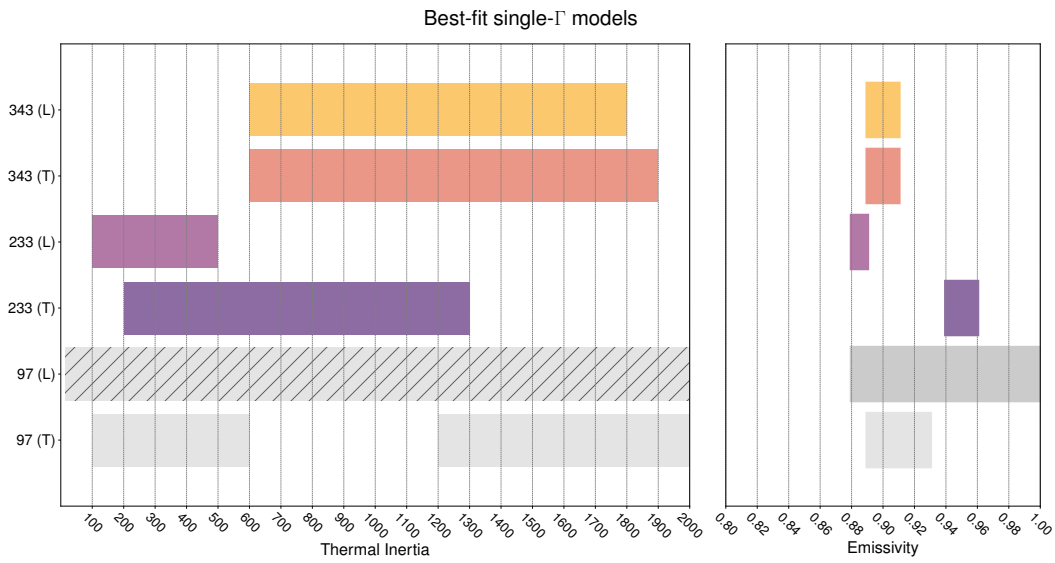

Figure 3.3: Results from model fits using single-Γ models (M_Γ). We note that the M_Γ approach produced consistent systematic effects in the residual maps indicating that none was a good fit, and is therefore not the preferred thermal modeling approach. For each observation frequency and hemisphere, the range of Γ and emissivity values that satisfied Eq. 3.5 are indicated by colored bars. The 97 GHz (L) models are not constrained in Γ space and are marked by a hatch pattern. The range of best-fit millimeter emissivities are shown on the right panel.

context of other observations of Callisto. The model residuals are presented in non-projected form in Fig. 3.6, as well as in map projected form in Fig. 3.7.

Valhalla Impact Basin

One of the most prominent thermal anomalies in these data is a cold spot on the leading hemisphere that tracks the center of the Valhalla impact basin. With its outer troughs extending to around 3800 km, Valhalla is Callisto's largest impact scar, and is likely the largest multiring impact basin in the solar system (Moore et al., 2004). The center of Valhalla is located at ∼18°N and ∼57°W, and was in-view for all of our leading hemisphere observations. For the 343 GHz data presented in Camarca et al. (2023), the site of the Valhalla impact basin was associated with a thermal anomaly about 10 K colder than surroundings in the calibrated images (rms of 0.20 K) and 3-5 K colder than the surroundings after subtracting the best-fit global model (i.e., after accounting for albedo). In the new 233 and 97 GHz images presented here, a similar large cold spot presents itself, which can be seen in the calibrated images and is even more pronounced in the Lambertian disk subtracted images (Fig. 3.1). The

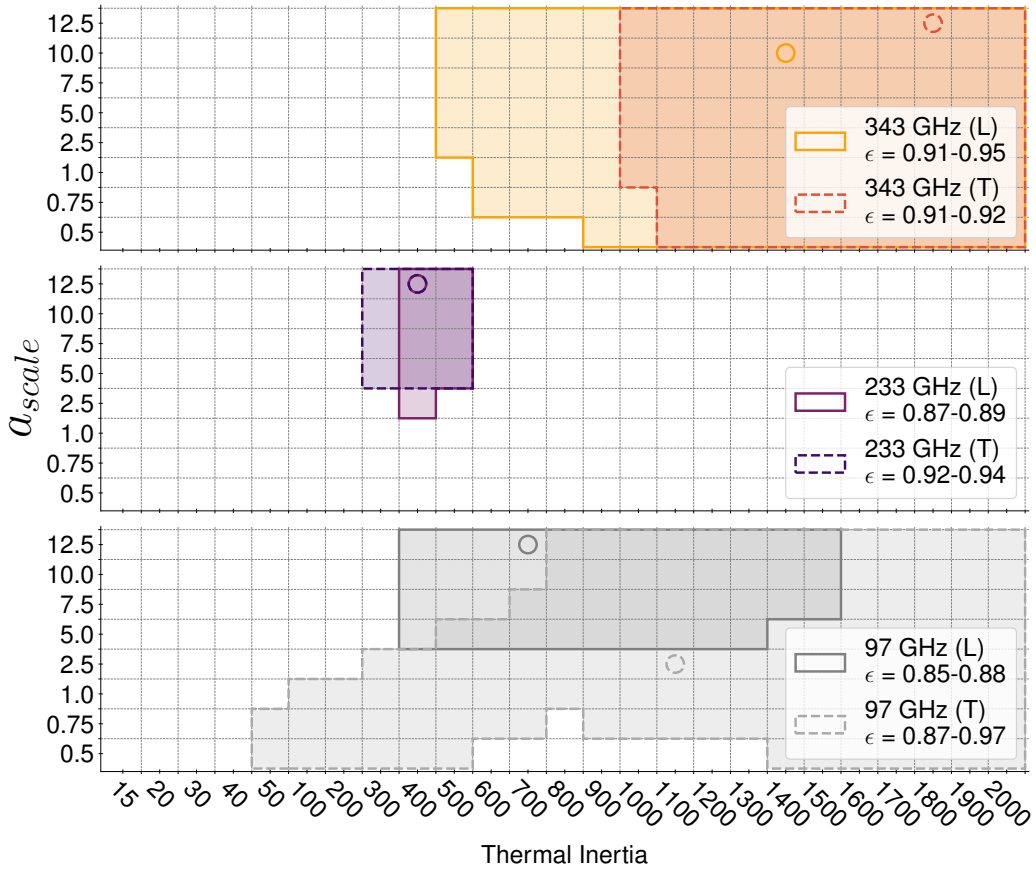

Figure 3.4: Summary of model fits treating electrical skin depth as a free parameter, $M_{\Gamma,\delta}$. The y-axis is presented as the factor by which δ_{elec} is decreased relative to pure water ice (a_{scale}); the actual δ_{elec} these values correspond to are temperature-dependent. Shaded regions refer to models that satisfied Eq. 3.5. The model results for each observing frequency (343, 233, and 97 GHz) are presented on separate panels for clarity. The circular markers indicate the location of the minimum χ^2 for each set of models; additionally, these markers indicate the $M_{\Gamma,\delta}$ models plotted in the second row of Fig. 3.6. Out of all of the observations, the 233 GHz observations are the most sensitive to changing δ_{elec}, while the observations at the other frequencies yield more poorly constrained δ_{elec} ranges. Importantly, this figure should be interpreted alongside Fig. 3.6, which demonstrates visually how the $M_{\Gamma,\delta}$ models outperform the M_{Γ} models.

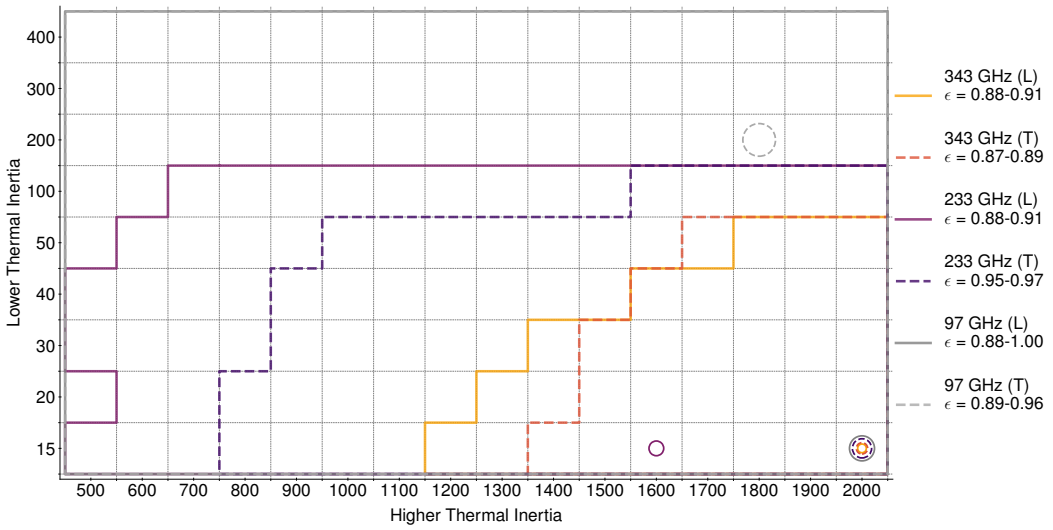

Figure 3.5: Summary of the two-Γ model ($M_{\Gamma,\Gamma}$) fits. For each observation, the range of two-Γ mixtures that satisfied Eq. 3.5 are enclosed below and to the right of the labeled lines. The 97 GHz results include the entire parameter space. The best-fit mixture model for each observation is denoted by an open circle; these same models are plotted in the third row of Fig. 3.6. The legend text (L) or (T) indicates a leading or trailing hemisphere observation, respectively. The best-fit emissivities are indicated under the observation label in the legend. For ease of interpretation, the exact ranges of acceptable mixing percentages for a given pair of thermal inertias is not shown. Generally, the Γ constraints for the 343 GHz data are tighter compared to the 233 GHz data. The 97 GHz data, both leading and trailing hemisphere, are not constrained at all.

T_b deviations of Valhalla from surrounding terrain in the 97 and 233 GHz best-fit thermal models are ∼5.2 K (3× rms) and ∼1.8 K (4× rms), respectively. The 233 GHz data observed Valhalla close to the morning terminator, while the 97 and 343 GHz data viewed it at local afternoon. The fact that the temperature difference with surrounding terrain is so much lower at 233 GHz therefore indicates that this region might have a higher thermal inertia than the surrounding terrain. It is possible that a lower emissivity in this region is also contributing to the thermal anomaly.

The association of cold thermal anomalies with large impact craters has been observed across many icy solar system objects. On Ganymede, cold spots were associated with the large impact craters Tros (D∼94 km) and Osiris (D∼107 km), as well as clusters of unresolved, small bright craters (de Kleer et al., 2021a). A 3 m depth temperature map based on 0.6-22 GHz observations using the Juno MWR instrument also confirmed that Tros is cold (Brown et al., 2023). Although Europa has far fewer craters than Ganymede or Callisto, its young crater Pwyll is thermally

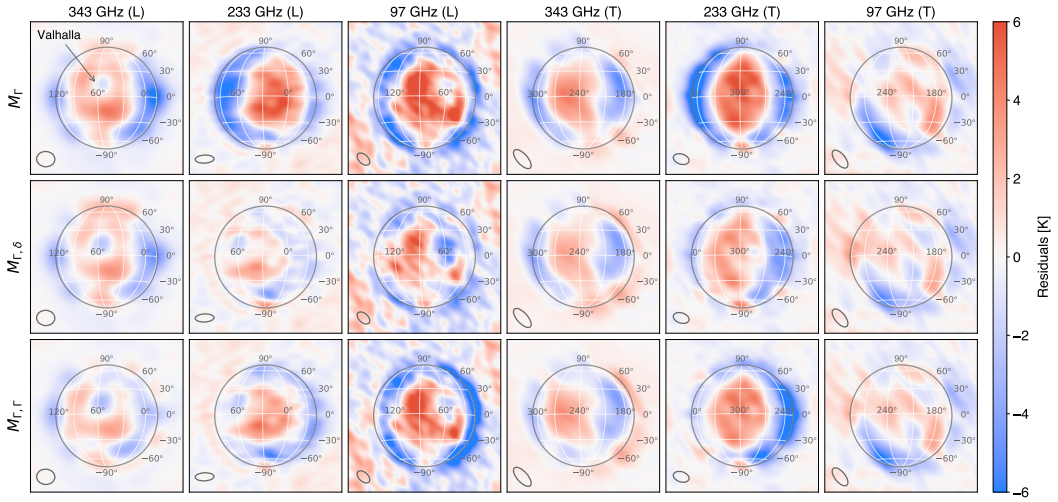

Figure 3.6: Grid of residuals derived from different thermal modeling approaches. Each column represents a unique observation, and each row is dedicated to a different modeling treatment. The first row shows residuals derived from models generated using a best-fit single thermal inertia (M_Γ). The second row shows residuals using a best-fit single thermal inertia with a variable skin depth ($M_{\Gamma,\delta}$). The third row shows best-fit residuals from using the two-thermal inertia mixture approach ($M_{\Gamma,\Gamma}$). Individual thermal anomalies on the disk edge are not considered reliable.

cold, as confirmed by Trumbo et al. (2017) and Trumbo et al. (2018) and Thelen et al. (2024). The Saturnian satellites follow suit, with cool craters identified on Titan (Janssen et al., 2016) and Rhea (Bonnefoy et al., 2020). In the cases listed here, cold is defined relative to a thermal model that already accounts for albedo. We note that, while cold craters are a general theme in thermal-wavelength data, there are certainly exceptions to this trend. For example, the large crater Tashmetum on Ganymede was not substantially cold in resolved ALMA images, suggesting some threshold for crater freshness may be required to impact a thermal fingerprint at these wavelengths (de Kleer et al., 2021a). Importantly, the Valhalla results presented here show that the cold crater trend is a phenomenon observed even for the largest impact class among icy satellites, namely the multiring impact basin. Understanding the thermal properties of large craters on Callisto may help inform further studies of localized volatile retention/excavation. For example, (Cartwright et al., 2024) recently mapped the 4.25 μm CO_2 absorption feature on Callisto using the Near Infrared Spectrograph (NIRSpec) instrument onboard the James Webb Space Telescope (JWST). These maps revealed solid-phase CO_2 enhancements in the multiring impact basin Asgard, as well as in pixels sampling the edge of Valhalla (Valhalla itself was not observed), a result in agreement with the Galileo NIMS map

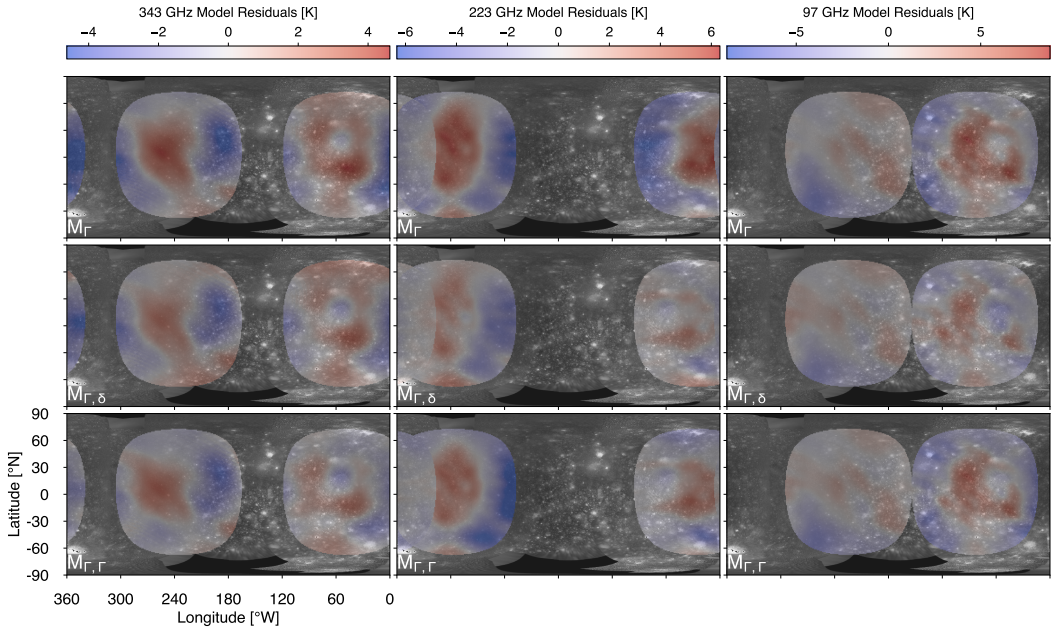

Figure 3.7: Residuals from Fig. 3.6 shown in projected form with the grayscale USGS Callisto map shown in the background. The Callisto grayscale data has been slightly modified to bring out surface features. Temperature residuals from each of our three modeling efforts are overlain in color, with warm colors denoted regions where the measured data are warmer than model predictions, and blue regions are colder than model predictions. First row: T_b residuals obtained using M_Γ models. Second row: T_b residuals obtained using $M_{\Gamma,\Gamma}$ models. Third row: T_b residuals obtained using $M_{\Gamma,\Gamma}$ models. The 343 GHz and 233 GHz trailing hemisphere model fits appears to have systematic discrepancies from the observations (i.e., poor center of disk/limb fits), while residuals at other hemispheres/frequencies appear to provide more reliable fits. Individual thermal anomalies near the disk center are generally more reliable than those at the disk edge.

(Hibbitts et al., 2002).

Adlinda, Heimdall, and Lofn

Like with Valhalla, the new data presented here also indicate the persistence of a cold spot near a suite of craters in Callisto's southern hemisphere. As noted in Camarca et al. (2023), a spot about 3-4 K cooler than nearby terrain was observed at 40° S, 12° W in the 343 GHz thermal model residuals. The candidate geologic unit(s) for that cold residual is the Adlinda/Heimdall/Lofn impact complex, which was not resolved by the ALMA beam. However, the cold spot's proximity to the satellite's limb precluded a definitive assignment to a local geologic feature due to geometric foreshortening. However, the new 233 GHz leading hemisphere image, centered at

a sub-observer longitude of 27° W, sampled a more favorable viewing geometry of the Adlinda/Heimdall/Lofn terrain, and indeed a cold spot at ∼30° W, ∼45° S and is co-located with this leading hemisphere crater suite. The sub-observer longitude of the 97 GHz leading hemisphere data was 85° W, which is too far west to observe any of these craters.

Cold Spot Near 270° W — a CO_2 Gas Connection?

One of the primary thermal features in the 97 GHz trailing hemisphere image is a near-limb cold spot roughly centered at −60° N and 270° W (Fig. 3.6). The 97 GHz trailing hemisphere data are not particularly responsive to different thermal model treatments, but depending on the implementation used, the cold spot is approximately 5-6 K colder than nearby terrain (Fig. 3.6). Based on the image rms of 0.96 K, this cold region is detected at 5× rms, making it the dominant thermal feature in that image; for comparison, the warmest warm region in that image is only ∼3 K above the best-fit model. Before proceeding to a discussion of this feature, we note that its proximity to the satellite's limb necessitates caution. This feature is additionally not obvious in the 233 GHz and 343 GHz trailing hemisphere image residuals. However, those data are poorly fit by the range of models tested, and it is the case that the cold spot tentatively associated with Adlinda/Heimdall/Lofn in Camarca et al. (2023) using just the 343 GHz image, which did not have a favorable viewing angle for that crater complex, is confirmed to be real based on the additional 233 GHz data presented here that has a more favorable viewing geometry. Treating this 97 GHz southern cold spot as tentatively real, we now highlight other relevant observations in this region.

Given that the sub-observer longitude of this image is 224° W, the nominal surface coverage includes material spanning 134°- 314° W. The possibility of whether the outermost terrains of Heimdall could explain this feature was explored, but in the Greeley et al. (2000) geologic map of Callisto, crater ejecta units mapped for Heimdall span from 315°-10° W, suggesting that these mapped materials are just out of view. Recently, Cartwright et al. (2024) published solid-phase CO_2 band depths and CO_2 gas column density for Callisto using the NIRSpec instrument onboard JWST. The JWST map reproduced the same trailing CO_2 bullseye pattern originally seen in Galileo NIMS data (Hibbitts et al., 2002); on Callisto, the trailing hemisphere is far richer in solid-phase CO_2 than the leading due to radiolytic processes. Curiously, in the JWST NIRSpec trailing hemisphere image cube, Callisto's peak CO_2

gas column density is physically offset from the peak of the solid CO_2 absorption. Instead, the gas peak is offset at around $-45°$ N, well aligned with where we observe the cold thermal anomaly in the ALMA data. It is possible that ALMA is sensing a local variation in subsurface composition that is linked to the CO_2 gas distribution.

Additional local residuals

While the previous two subsections described localized thermal anomalies for which there were geologic associations, in this section we discuss thermal features that lack such an association. There is a cold spot on the trailing hemisphere centered at roughly 210° W and $-20°$ N that is visible in a number of model residuals. The feature is most prominent in the 97 GHz trailing hemisphere residual map, which does not exhibit prominent disk center/limb fit systematics. However, evidence for this feature may also exist in the 343 GHz trailing residuals, as there is possibly a slightly colder structure at the same location in those model residuals. Additionally this feature can be seen in the 343 GHz trailing hemisphere Lambertian disk subtracted image (Fig. 3.1). Based on the Greeley et al. (2001) geologic map, the disk in-view for the 97 GHz trailing hemisphere image does not sample any major geologic units. The terrain is largely cratered plains with smaller mapped craters that are much smaller than the ALMA synthesized beam. A mapped geologic unit in the Greeley et al. (2001) map that approaches the ALMA beam size is a rounded patch of light plains centered at around 290 W and $-28°$ N. The light plains units are marked by a higher albedo (compared to the typical cratered plains), bear fewer craters, and are thought to form from the more ice-rich materials excavated by impact processes. Additionally in the 97 GHz trailing hemisphere residual, near 30° N and 180° W, there is a cold spot observed that is about 1.3 K colder than the disk average. This feature is possibly due the presence of some craters that fall just within the western bounds of the multiring basin Asgard. The primary named crater in this region is the bright impact feature Nirkes.

In addition, we follow up on the discussion in Camarca et al. (2023) addressing the existence of an "L-shape" thermal feature on the leading hemisphere in the 343 GHz feature. To summarize the finding of Camarca et al. (2023), there appears to be an L-shaped warm anomaly occupying the area west and south of Valhalla. The vertical component of the L is centered at almost 90° W and is symmetric across the equator with a divergence from the model of $\sim$2-3 K, while the horizontal portion of the L is similarly warm, and extends eastward to $\sim$25° W. The 233 and 97

GHz leading images presented here provide more face-on viewing geometries for the horizontal and vertical components of this warm L, respectively. In Fig. 3.6, the 233 GHz residuals also bear the warmest T_b values in the area west and south of Valhalla, with a very similar morphology to that observed in the 343 GHz residuals. In the 97 GHz image, a warm region is reproduced in the same area, although the other parts of the "L" shape appear less structured. In Camarca et al. (2023), micrometeorite bombardment preferentially texturizing Callisto's leading hemisphere (and therefore resulting in lower Γ materials that can warm up faster) was proposed as a possible origin of this leading hemisphere warm anomaly. However, it is not clear from the model residuals whether or not Callisto's leading hemisphere is significantly warmer than the trailing. The 97 GHz residuals do seem to indicate that leading hemisphere low-latitude warm spots are warmer than trailing hemisphere low-latitude warm spots, however the 233 and 343 GHz trailing hemisphere residuals have systematic patterns that preclude a similar inspection. The large scale structure of the hot and cold spots on the trailing hemisphere as observed in the 233 and 343 GHz residuals may require more complex model physics (e.g., roughness) than is used by the present approach. Future efforts to model Callisto's unique thermal properties may address these issues.

3.5 Conclusions

We present millimeter thermal images of Callisto's leading and trailing hemisphere obtained at 97 GHz (3 mm), 233 GHz (1.3 mm), and 343 GHz (0.87 mm). Our observations were acquired using the Atacama Large Millimeter/submillimeter Array. We find disk-averaged brightness temperatures across the 97-343 GHz regime to be T_b = 106-116, and are consistent with past (unresolved) observations.

To interpret our data, we used three different thermal modeling procedures: 1) M_Γ: single-Γ models, 2) $M_{\Gamma,\delta}$: single-Γ models with a variable electrical skin depth δ_{elec}, and 3) $M_{\Gamma,\Gamma}$: two-Γ models. Consistent with the conclusions of Spencer (1987a) and Camarca et al. (2023), Callisto's thermal emission is not well modeled if only a simple single-Γ treatment is used. In this work, we find the M_Γ approach yielded systematic residuals across the disk, including a persistent inability to fit the disk limb and disk center simultaneously. We find that, for several observations, the addition of a variable δ_{elec} as a free parameter or a secondary Γ yielded a better fit to the data, as evidenced by an increased ability to fit both the disk center and disk limb emission, as well as lower overall T_b residuals. For example, a thermal cold spot associated with the Valhalla impact basin is barely discernible in M_Γ 233 GHz

leading hemisphere residuals, but is easily discernible in the $M_{\Gamma,\delta}$ and $M_{\Gamma,\Gamma}$ treatments. A robust finding is consistently high millimeter emissivities across all model treatments, ranging from 0.85-0.97, compared to 0.75-0.85 for Europa (Trumbo et al., 2017; Trumbo et al., 2018; Thelen et al., 2024) and Ganymede (de Kleer et al., 2021a) at these wavelengths. To summarize the thermal inertias derived from each of the three model approaches (M_{Γ},$M_{\Gamma,\delta}$,$M_{\Gamma,\Gamma}$) we find: the best-fit values derived from M_{Γ} are Γ = 600-1900, 100-1300, and unconstrained, for 343, 233, and 97 GHz respectively; we highlight that we find the M_{Γ} approach is not preferred for these Callisto data. The best-fit values adopting the $M_{\Gamma,\delta}$ approach are: Γ = 500-2000, 300-600, and 50-2000 for 343, 233, and 97 GHz respectively. Lastly, the best-fit (lower, higher) Γ ranges from $M_{\Gamma,\Gamma}$ are: Γ = (<100, unconstrained) for 233 GHz; Γ = (<50, >1200) for 343 GHz; and unconstrained for 97 GHz. The fact that we do not constrain an obvious difference in the value of the thermal properties across the sampled 97-343 GHz frequency range may suggest that these ALMA data, which probe depths of up ∼10s of cm, have not bypassed Callisto's dark material blanket.

Callisto's trailing hemisphere observations were generally much less responsive to thermophysical model alterations compared to the leading hemisphere. The 343 GHz and 233 GHz trailing hemisphere residuals both bear systematic T_b east/west structure that is not accounted for within our current model parameters. Because of this, identifying localized thermal features for those observations is difficult. Although the Γ values are also difficult to constrain for the 97 GHz trailing hemisphere data, regardless of model treatment, the residuals do not have the same systematic structure that persists at the other two higher frequencies.

After subtraction of the best-fit thermal models, the residual images reveal several thermal anomalies. There are 3-5 K cold thermal anomalies associated with Valhalla, as well as with the impact craters Adlinda/Heimdall/Lofn (which are not resolved from one another in the data). Regarding Valhalla, its thermal anomaly may be explained by the presence of a material that is either higher thermal inertia than surrounding terrain, and perhaps lower emissivity. An additional cold anomaly is seen in the trailing hemisphere southern latitudes, which is co-located with the maximum CO_2 gas observed by JWST/NIRSpec (Cartwright et al., 2024). Finally, an L-shaped warm anomaly in the center of the leading hemisphere tentatively presented by Camarca et al. (2023) in the standalone 343 GHz data is confirmed at additional frequencies, and may be due to a lower thermal inertia regolith there due to meteorite.

The data presented here provide the first global, spatially-resolved thermal maps of Callisto's surface at ALMA observing frequencies, and collectively shed light on the material properties of Callisto's bulk surface as well as providing a new window into the surface materials present in its large impact basins. From the ground, these ALMA data may be combined with observations of Callisto using the Very Large Array (VLA) which operates in the 1-50 GHz regime, as well as the planned upgrade to the VLA, the next generation VLA (ngVLA). The lower frequencies accessible by these observing facilities could reach >meter depths, and could help provide further constraints on Callisto's dark material blanket. Moreover, future spacecraft observations of Callisto by the JUICE instrument payload will provide ground-truth data to complement observations from telescope facilities. The JUICE instrumentation particularly relevant to these ALMA data includes the Submillimeter Wave Instrument (SWI), which operates at 530-1275 GHz, and will help link existing millimeter and infrared observations. Altogether, a new era of Callisto exploration is in the near future, and continued studies of Callisto's thermal properties will shed light on the origins of the surface material of this ancient moon.

Acknowledgements

We acknowledge support from the National Science Foundation through a Graduate Research Fellowship under Grant No. DGE-1745301 to M.C., as well as through grants 2308280 and 2308281, which supported K.d.K., M.C., A.E.T., and I.d.P. This research was also funded in part by the Heising-Simons Foundation through grant #2019-1611. Funding was additionally provided by the NASA ROSES Solar System Observations program (through Task Order 80NM0018F0612) for A.E.T., K.d.K., A.A. Contributions by A.A. were carried out at the Jet Propulsion Laboratory, California Institute of Technology, under a contract with the National Aeronautics and Space Administration (80NM0018D0004). This paper makes use of the following ALMA data: ADS/ JAO.ALMA#2016.1.00691.S. ALMA is a partnership of ESO (representing its member states), NSF (USA) and NINS (Japan), together with NRC (Canada), MOST and ASIAA (Taiwan), and KASI (Republic of Korea), in cooperation with the Republic of Chile. The Joint ALMA Observatory is operated by ESO, AUI/NRAO, and NAOJ. The National Radio Astronomy Observatory is a facility of the National Science Foundation operated under cooperative agreement by Associated Universities, Inc.

BIBLIOGRAPHY

Basilevsky, A. T. et al. (2002). "The Morphology of Small Craters and Knobs on the Surface of Jupiter's Satellite Callisto". *Solar System Research* Vol. 36, No. 4. DOI: 10.1023/A:1019576422376.

Berge, G. L. et al. (1975). "Callisto: Disk Temperature at 3.71-Centimeter Wavelength". *Science* Vol. 187, No. 4175. DOI: 10.1126/science.187.4175.441.

Bonnefoy, L. et al. (2020). "Rhea's subsurface probed by the Cassini radiometer: Insights into its thermal, structural, and compositional properties". *Icarus* Vol. 352. DOI: 10.1016/j.icarus.2020.113947.

Bottke, W. F. et al. (2013). "Black rain: The burial of the Galilean satellites in irregular satellite debris". *Icarus* Vol. 223, No. 2. DOI: 10.1016/j.icarus.2013.01.008.

Briggs, D. S. (1995). "High Fidelity Interferometric Imaging: Robust Weighting and NNLS Deconvolution". Vol. 187.

Brogan, C. L. et al. (2018). "Advanced Gain Calibration Techniques in Radio Interferometry". *arXiv:1805.05266 [astro-ph]*.

Brown, S. et al. (2023). "Microwave Observations of Ganymede's Sub-Surface Ice: I. Ice Temperature and Structure". *Journal of Geophysical Research: Planets* Vol. 128, No. 6. DOI: 10.1029/2022JE007609.

Butler, B. (2012). *ALMA Memo 594*.

Butler, B. J. et al. (1999). "Solar System Objects". *Synthesis Imaging in Radio Astronomy II*. Ed. by G. B. Taylor et al. Vol. 180.

Camarca, M. et al. (2023). "Thermal Properties of the Leading Hemisphere of Callisto Inferred from ALMA Observations". *The Planetary Science Journal* Vol. 4, No. 8. DOI: 10.3847/PSJ/aceb68.

Cambioni, S. et al. (2019). "Constraining the thermal properties of planetary surfaces using machine learning: Application to airless bodies". *Icarus* Vol. 325. DOI: 10.1016/j.icarus.2019.01.017.

Cartwright, R. J. et al. (2024). "Revealing Callisto's Carbon-rich Surface and CO_2 Atmosphere with JWST". *The Planetary Science Journal* Vol. 5, No. 3. DOI: 10.3847/PSJ/ad23e6.

Clark, B. G. (1980). "An efficient implementation of the algorithm 'CLEAN'". *Astronomy and Astrophysics* Vol. 89, No. 3.

de Kleer, K. et al. (2021a). "Ganymede's Surface Properties from Millimeter and Infrared Thermal Emission". *The Planetary Science Journal* Vol. 2, No. 1. DOI: 10.3847/PSJ/abcbf4.

de Kleer, K. et al. (2021b). "The Surface of (16) Psyche from Thermal Emission and Polarization Mapping". *The Planetary Science Journal* Vol. 2, No. 4. DOI: 10.3847/PSJ/ac01ec.

de Pater, I. et al. (1984). "VLA observations of the Galilean satellites". *Icarus* Vol. 57, No. 1. DOI: 10.1016/0019-1035(84)90011-3.

de Pater, I. et al. (1989). "Planetary Observations at a Wavelength of 355/zm". *Icarus* Vol. 79.

de Pater, I. et al. (2014). "Neptune's global circulation deduced from multi-wavelength observations". *Icarus* Vol. 237. DOI: 10.1016/j.icarus.2014.02.030.

de Pater, I. et al. (2019). "First ALMA Millimeter-wavelength Maps of Jupiter, with a Multiwavelength Study of Convection". *The Astronomical Journal* Vol. 158, No. 4. DOI: 10.3847/1538-3881/ab3643.

de Pater, I. et al. (2020). "ALMA Observations of Io Going into and Coming out of Eclipse". *The Planetary Science Journal* Vol. 1, No. 3. DOI: 10.3847/PSJ/abb93d.

de Pater, I. et al. (2021). "SOFIA Observations of Variability in Jupiter's Para-H_2 Distribution and Subsurface Emission Characteristics of the Galilean Satellites". *The Planetary Science Journal* Vol. 2, No. 6. DOI: 10.3847/PSJ/ac2d24.

Ferrari, C. (2018). "Thermal Properties of Icy Surfaces in the Outer Solar System". *Space Science Reviews* Vol. 214, No. 8. DOI: 10.1007/s11214-018-0546-x.

Francis, L. et al. (2020). "On the Accuracy of the ALMA Flux Calibration in the Time Domain and across Spectral Windows". *The Astronomical Journal* Vol. 160. DOI: 10.3847/1538-3881/abbe1a.

Greeley, R. et al. (2000). "Galileo views of the geology of Callisto". *Planetary and Space Science* Vol. 48, No. 9. DOI: 10.1016/S0032-0633(00)00050-7.

Greeley, R. et al. (2001). "Geology of Lofn Crater, Callisto". *Journal of Geophysical Research: Planets* Vol. 106 (E2). DOI: 10.1029/2000JE001262.

Grundy, W. M. et al. (1999). "Near-Infrared Spectra of Icy Outer Solar System Surfaces: Remote Determination of H2O Ice Temperatures". *Icarus* Vol. 142, No. 2. DOI: 10.1006/icar.1999.6216.

Hanuš, J. et al. (2015). "Thermophysical modeling of asteroids from WISE thermal infrared data - Significance of the shape model and the pole orientation uncertainties". *Icarus* Vol. 256. DOI: 10.1016/j.icarus.2015.04.014.

Hewison, T. et al. (1999). "Airborne retrievals of snow and ice surface emissivity at millimeter wavelengths". *IEEE Transactions on Geoscience and Remote Sensing* Vol. 37, No. 4. DOI: 10.1109/36.774700.

Hibbitts, C. A. et al. (2002). "CO2-rich impact craters on Callisto". *Journal of Geophysical Research: Planets* Vol. 107 (E10). DOI: 10.1029/2000JE001412.

Howett, C. et al. (2011). "A high-amplitude thermal inertia anomaly of probable magnetospheric origin on Saturn's moon Mimas". *Icarus* Vol. 216, No. 1. DOI: 10.1016/j.icarus.2011.09.007.

Howett, C. et al. (2012). "PacMan returns: An electron-generated thermal anomaly on Tethys". *Icarus* Vol. 221, No. 2. DOI: 10.1016/j.icarus.2012.10.013.

Howett, C. et al. (2019). "Maps of Tethys' thermophysical properties". *Icarus* Vol. 321. DOI: 10.1016/j.icarus.2018.12.018.

Janssen, M. et al. (2016). "Titan's surface at 2.18-cm wavelength imaged by the Cassini RADAR radiometer: Results and interpretations through the first ten years of observation". *Icarus* Vol. 270. DOI: 10.1016/j.icarus.2015.09.027.

Khurana, K. K. et al. (1998). "Induced magnetic fields as evidence for subsurface oceans in Europa and Callisto". *Nature* Vol. 395, No. 6704. DOI: 10.1038/27394.

Kivelson, M. G. et al. (1999). "Europa and Callisto: Induced or intrinsic fields in a periodically varying plasma environment". *Journal of Geophysical Research* Vol. 104. DOI: 10.1029/1998JA900095.

Mitchell, D. L. et al. (1994). "Microwave Imaging of Mercury's Thermal Emission at Wavelengths from 0.3 to 20.5 cm". *Icarus* Vol. 110, No. 1. DOI: 10.1006/icar.1994.1105.

Moore, J. et al. (2004). "Callisto". *Jupiter: The Planet, Satellites and Magnetosphere*. Cambridge: Cambridge University Press.

Moreno, R. (2007). *Report on continuum measurements of Ganymede and Callisto with the IRAM–PdB interferometer : Application to flux calibration, Internal Memo*.

Morrison, D. (1977). "Galilean Satellites: Anomalous Temperatures Disputed". *Science* Vol. 195, No. 4273. DOI: 10.1126/science.195.4273.90.c.

Morrison, D. et al. (1972). "Temperatures of Titan and the Galilean Satellites at 20 Microns". *The Astrophysical Journal* Vol. 173. DOI: 10.1086/180934.

Muhleman, D. O. et al. (1986). "Precise VLA positions and flux-density measurements of the Jupiter system." *The Astronomical Journal* Vol. 92. DOI: 10.1086/114279.

Muhleman, D. O. et al. (1991). "Observations of Mars, Uranus, Neptune, Io, Europa, Ganymede, and Callisto at a wavelength of 2.66 mm". *Icarus* Vol. 92. DOI: 10.1016/0019-1035(91)90050-4.

Müller, T. G. et al. (2016). "Far-infrared photometric observations of the outer planets and satellites with Herschel-PACS". *Astronomy & Astrophysics* Vol. 588. DOI: 10.1051/0004-6361/201527371.

Pauliny-Toth, I. I. K. et al. (1974). "The Brightness Temperatures of Ganymede and Callisto at 2.8 CM Wavelength". *Astronomy and Astrophysics, Vol. 34, p. 129 (1974)* Vol. 34.

Pauliny-Toth, I. I. K. et al. (1977). “Observations of Ganymede and Callisto at 1.3 cm wavelength.” *Astronomy and Astrophysics* Vol. 58, No. 3.

Press, W. H. et al. (1986). *Numerical recipes. The art of scientific computing*.

Rau, U. et al. (2011). “A multi-scale multi-frequency deconvolution algorithm for synthesis imaging in radio interferometry”. *Astronomy & Astrophysics* Vol. 532. DOI: 10.1051/0004-6361/201117104.

Sault, R. J. et al. (1994). “Multi-frequency synthesis techniques in radio interferometric imaging.” *Astronomy and Astrophysics Supplement Series* Vol. 108.

Saur, J. et al. (2010). “Induced Magnetic Fields in Solar System Bodies”. *Space Science Reviews* Vol. 152, No. 1. DOI: 10.1007/s11214-009-9581-y.

Sparks, W. B. et al. (2017). “Active Cryovolcanism on Europa?” *The Astrophysical Journal Letters* Vol. 839, No. 2. DOI: 10.3847/2041-8213/aa67f8.

Spencer, J. R. (1987a). “Thermal segregation of water ice on the Galilean satellites”. *Icarus* Vol. 69, No. 2. DOI: 10.1016/0019-1035(87)90107-2.

Spencer, J. R. et al. (1999). “Temperatures on Europa from Galileo Photopolarimeter-Radiometer: Nighttime Thermal Anomalies”. *Science* Vol. 284, No. 5419. DOI: 10.1126/science.284.5419.1514.

Spencer, J. R. (1987b). “THE SURFACES OF EUROPA, GANYMEDE, AND CALLISTO: AN INVESTIGATION USING VOYAGER IRIS THERMAL INFRARED SPECTRA (JUPITER).” PhD thesis. University of Arizona.

Spilker, L. J. et al. (2005). “CASSINI CIRS OBSERVATIONS OF A ROLL-OFF IN SATURN RING SPECTRA AT SUBMILLIMETER WAVELENGTHS”. *Earth, Moon, and Planets* Vol. 96, No. 3. DOI: 10.1007/s11038-005-9060-8.

Spilker, L. J. et al. (2018). “Thermal Properties of Rings and Ring Particles”. *Planetary Ring Systems*. Ed. by M. S. Tiscareno et al. 1st ed. Cambridge University Press. DOI: 10.1017/9781316286791.015.

Team, T. C. et al. (2022). “CASA, the Common Astronomy Software Applications for Radio Astronomy”. *Publications of the Astronomical Society of the Pacific* Vol. 134, No. 1041. DOI: 10.1088/1538-3873/ac9642.

Thelen, A. E. et al. (2024). “Subsurface Thermophysical Properties of Europa’s Leading and Trailing Hemispheres as Revealed by ALMA”. *The Planetary Science Journal* Vol. 5, No. 2. DOI: 10.3847/PSJ/ad251c.

Thompson, A. R. et al. (2017). *Interferometry and Synthesis in Radio Astronomy*. Astronomy and Astrophysics Library. Cham: Springer International Publishing. DOI: 10.1007/978-3-319-44431-4.

Trumbo, S. K. et al. (2017). “ALMA Thermal Observations of a Proposed Plume Source Region on Europa”. *The Astronomical Journal* Vol. 154, No. 4. DOI: 10.3847/1538-3881/aa8769.

Trumbo, S. K. et al. (2018). “ALMA Thermal Observations of Europa”. *The Astronomical Journal* Vol. 156, No. 4. DOI: 10.3847/1538-3881/aada87.

Ulich, B. L. (1981). “Millimeter-wavelength continuum calibration sources.” *The Astronomical Journal* Vol. 86. DOI: 10.1086/113046.

Ulich, B. L. et al. (1976). “Observations of Ganymede, Callisto, Ceres, Uranus, and Neptune at 3.33 mm wavelength”. *Icarus* Vol. 27, No. 2. DOI: 10.1016/0019-1035(76)90001-4.

Ulich, B. L. et al. (1984). “Planetary observations at a wavelength of 1.32 mm”. *Icarus* Vol. 60, No. 3. DOI: 10.1016/0019-1035(84)90166-0.

Warren, S. G. (2019). “Optical properties of ice and snow”. *Philosophical Transactions of the Royal Society A: Mathematical, Physical and Engineering Sciences* Vol. 377, No. 2146. DOI: 10.1098/rsta.2018.0161.

Yan, B. et al. (2008). “Retrieval of snow surface microwave emissivity from the advanced microwave sounding unit”. *Journal of Geophysical Research: Atmospheres* Vol. 113 (D19). DOI: 10.1029/2007JD009559.

Zahnle, K. et al. (1998). “Cratering Rates on the Galilean Satellites”. *Icarus* Vol. 136, No. 2. DOI: 10.1006/icar.1998.6015.

Zimmer, C. (2000). “Subsurface Oceans on Europa and Callisto: Constraints from Galileo Magnetometer Observations”. *Icarus* Vol. 147, No. 2. DOI: 10.1006/icar.2000.6456.

Chapter 4

A STUDY OF CALLISTO'S VOLATILES USING JWST NIRSPEC FEATURING A NEW VALHALLA-CENTERED OBSERVATION

The content of this chapter was adapted from the following article:

Camarca, M., K. de Kleer, R. J. Cartwright, G. L. Villanueva, B. Holler, K. P. Hand, L. Roth, and C. P. Glein (in preparation). "A Study of Callisto's Volatiles using JWST NIRSpec Featuring a New Valhalla-Centered Observation". *Planetary Science Journal*.

Abstract

We present maps of H_2O, CO_2, and a tentative CN-bearing 4.57 μm spectral feature across Callisto's surface as observed with JWST. H_2O ice is mapped by measuring the band area of the 3.1 μm Fresnel peak across the leading and trailing hemispheres. Here, we update the CO_2 and 4.57 μm band depth maps originally presented in Cartwright et al. (2024) with a new JWST observation of Callisto, centered over Valhalla, the largest multi-ring impact basin in the solar system. Our H_2O ice map shows the Fresnel peak exhibits a depleted, bull's eye pattern on the trailing hemisphere, and is largely controlled by geology/albedo on the leading hemisphere. This dichotomy is possibly related, either directly or indirectly, to Jovian plasma impinging on the trailing hemisphere. Our solid-phase CO_2 map recovers a strong enhancement in this volatile in the vicinity of the Lofn/Heimdall impacts, an area that may be the largest reservoir of non-radiolytic CO_2 on Callisto. We also present a new detection of gas-phase CO_2 with a patchy distribution that does not correlate with the peak surface CO_2 abundance.

4.1 Introduction

The Galilean moons of Jupiter—Io, Europa, Ganymede, and Callisto—host an incredible treasury of surface processes. Endogenic geologic processes such as volcanism, tectonics, and evidence of surface-interior interactions are present on Io (Morabito et al., 1979; de Kleer et al., 2024; Davies et al., 2006), Europa (McCord et al., 1999; Schmidt et al., 2011), and Ganymede (Pappalardo et al., 2004), but are

mainly absent from Callisto (Moore et al., 2004). Although Callisto is excluded from the Laplace resonance that helps drive tidal heating on the inner three moons (de Kleer et al., 2019), Galileo magnetometer results indicate the signature of an induced field, possibly originating from a saline subsurface ocean (Zimmer, 2000; Cochrane et al., 2025). At the global scale, Callisto's geology is dominated by large impacts, including exotic multi-ring impact basins of great diameters unseen on any other solar system object (Moore et al., 2004). Callisto's surface volatile inventory includes H_2O, CO_2, and possibly S-bearing compounds (Hibbitts et al., 2000; McCord et al., 1998; Cartwright et al., 2020). These volatiles are accompanied by the largest share of dark material in the Galilean system, as evidenced by Callisto bearing the lowest albedo ($\sim$0.2) compared to the other three moons. This dark material is likely a thick lag deposit formed by the removal of high-albedo volatiles via continual sublimation (Moore et al., 1999), akin to the process observed on comets. Substantial amounts of dust have likely accumulated on Callisto's ancient surface over the age of the Solar System, perhaps including dust from the Jovian irregular satellites (Bottke et al., 2013). As such, by virtue of its geologic quiescence, Callisto serves as a template for understanding how an airless body evolves under the near exclusive control of exogenic processes.

At present, the study of exposed H_2O ice on Callisto and its sibling moons is motivated by the centrality of ice in feeding surface chemistry and atmospheric processes. Because the Galilean satellites are embedded in the intense Jovian magnetosphere, H_2O ice on their surfaces is subject to ongoing processing by a variety of trapped charged particles (electrons, protons, S^+ and other heavy ions), exhibiting a wide range of energies from $\sim$1 KeV to 100s MeV (e.g., Cassidy et al. 2010 and references therein). For instance, H_2O ice radiolysis is a fundamental step in the formation of molecular oxygen (Johnson et al., 1997b). Molecular oxygen exists in the Galilean satellite atmospheres as inferred from UV and optical atomic O emissions (de Kleer et al., 2023; Cunningham et al., 2015), as well as on their surfaces, likely trapped in H_2O ice (Spencer et al., 2002; Trumbo et al., 2021; Oza et al., 2024; Johnson et al., 1997a). Additionally, H_2O ice may serve as a solid-phase host that helps Callisto retain some of its highly volatile CO_2. In the near-infrared, the state of H_2O ice may be probed through analyses of spectral features in the 1 to 3 μm range. Examples of early ground-based observations of H_2O ice on Callisto include those acquired with Kuiper Airborne Observatory (Pollack et al., 1978) and Mauna Kea Observatory (Clark et al., 1980), and evidence for the presence of frost was also noted in early thermal measurements (Morrison et al., 1972). The current primary

source of information about Callisto's H_2O ice originates from data acquired by the NIMS instrument onboard the Galileo spacecraft. The NIMS instrument provided spectral measurements in the 0.7-5.2 μm range with a spectral resolving power of R ∼40-200 (Carlson et al., 1992). The NIMS data show that the presence of exposed H_2O ice generally tracked with the presence of craters, however the NIMS spectra were often noisy due to internal instrument performance and Callisto's low levels of exposed surface ice (∼10 percent areal coverage, Hansen et al. 2004).

At present, studies of H_2O and the chemistry of volatiles in the Galilean system are being greatly advanced by the James Webb Space Telescope (JWST). As an infrared telescope, JWST is sensitive to the ro-vibrational absorption and emission features of solid- and gas-phase volatiles that dominate the surface compositions of these moons. And with the incredible spatial resolution of JWST, the location of these volatiles can be tethered to geologic maps of the surface made from spacecraft data, such that their origins (either endogenic or exogenic) can be evaluated. For example, SO gas has been observed right above an active volcano on Io (de Pater et al., 2023). JWST observations of Europa confirmed that surficial CO_2 reservoirs are largely (but not exclusively) concentrated in chaos terrains located in Tara and Powys Regiones, consistent with a subsurface origin (Trumbo et al., 2023b; Villanueva et al., 2023a). JWST observations of Ganymede show in great detail how the moon's intrinsic magnetic field promotes the collection of select volatiles near the poles (Trumbo et al., 2023a; Bockelée-Morvan et al., 2024b). The first published analysis of Callisto using the Near Infrared Spectrograph (NIRSpec) instrument onboard JWST focused on the moon's CO_2 reservoirs (Cartwright et al., 2024). In this work, we provide JWST spectral maps of the 3.1 μm Fresnel Reflectance peak on Callisto. In addition, we extend recent spectral maps of CO_2 and the 4.57 μm feature (Cartwright et al., 2024) with a new JWST observation centered on Callisto's largest impact basin, Valhalla.

The organization of this paper is as follows: Section 4.2 describes the reduction of the JWST NIRSpec data and parameter extraction for the spectral features. Section 4.3 describes the results of mapping the Fresnel Peak across Callisto's entire surface, as well as the maps of CO_2 and the 4.57 μm feature. Section 4.4 offers our interpretation of these features, including how localized enhancements do/do not correlate with local geology. We also place these new Callisto results in context with those obtained for the other icy Galilean moons. Section 4.5 summarizes the conclusions of this work.

4.2 Methods

Observations

Observations of Callisto were obtained using the James Webb Space Telescope (JWST), located at the L2 Lagrange point of the Sun-Earth system (Gardner et al., 2023). The primary mirror of JWST is 6.5 m, and the telescope's incredible sensitivity and spatial resolution permit detailed mapping of spectral features on the Galilean satellites and other solar system bodies. We used the NIRSpec instrument (Jakobsen et al., 2022) as part of General Observer (GO) program 2060, which observed Callisto on 2022 November 15th and 25th (previously reported in Cartwright et al. 2024) and 2023 September 20th (reported here). The respective sub-observer longitudes of these observations were 279° W, 137° W, and 56° W; these viewing geometries permitted samples of Callisto's trailing hemisphere, the Asgard impact basin, and the Valhalla impact basin, respectively. The G395H grating was used in all three observations, spanning 2.85–5.35 μm with an average R $\sim$ 2700. Each observation was acquired via a set of four 32 s exposures that each sample different parts of the detector (i.e., four dithers), using the NRSRAPID readout mode. Data were collected using NIRSpec's integral field unit (IFU) that has a $3'' \times 3''$ field of view, and a pixel size of $0.1''$.

The data were downloaded from the Mikulski Archive for Space Telescopes (MAST) at the Space Telescope Science Institute, and they can be accessed via `doi:10.17909/w8qj-5v21`. Additional custom codes were developed to combine dithered frames and remove bad pixels. The four dithers were georeferenced to Callisto's disk and then median combined, which assisted in removing abnormal pixels. At each spatial pixel (spaxel), we distinguished between reflectance and thermal emission components by applying a two-component model: a realistic solar model for reflected light and a Planck function for thermal radiation. We generated the solar model using the Planetary Spectrum Generator (PSG; Villanueva et al. 2018; Villanueva et al. 2022), which adjusts for Doppler shifts, uses the high-fidelity ACE solar spectrum (Hase et al. 2010) to account for solar Fraunhofer lines, and employs the Kurucz (2005) model to reproduce the continuum intensity. After subtracting the thermal component, we calculated reflectance spectra for each spaxel by dividing the calibrated flux values by a solar model. This model was scaled according to the pixel's projected spatial dimensions and corrected for the Sun-Callisto and JWST-Callisto distances at the observation times. This methodology parallels that used in previous analyses of NIRSpec IFU data for Europa (Villanueva et al., 2023a), Callisto (Cartwright et al., 2024), and Enceladus (Villanueva et al., 2023b).

Data Analysis

Retrieval of solid-state spectral features: After the NIRSpec cubes were thermally-corrected and dither-averaged, we mapped the spatial distribution of three spectral features of interest. First, we registered the center point of Callisto's disk and determined the range of pixels that fall within the projected radius of Callisto at the time of each observation. After spatial registration, we proceeded to map: the 4.25 μm CO_2 feature, the 3.1 μm H_2O ice Fresnel peak, and a 4.57 μm absorption. For these fits, we used the Python package lmfit to retrieve band parameters (Newville et al., 2025). For the 4.25 μm CO_2 and 4.56 μm features, we simultaneously fit Gaussian absorption profiles and linear continuum fits. The value of the absorption feature at their minimums was divided by the appropriate continuum value to retrieve the band depth. For the 3.1 μm Fresnel reflectance peak, we fit a three-component model that consisted of a 1) linear continuum from 3.00 to 3.30 μm, 2) a Gaussian profile centered near 3.1 μm, and 3) a second Gaussian profile centered near 3.2 μm. We initially tested the Fresnel peak fits with a single Gaussian at 3.1 μm, however the need for a secondary component was motivated by structure in the residuals, especially for pixels with stronger 3.1 μm peaks (e.g., see Fig. 4.2). The multi-peaked structure of the Fresnel peak is well-documented in icy satellites (including Callisto, Hansen et al. 2004). After both peaks were fit by a full model, we then summed the areas of both peaks above the continuum to determine the integrated band area in units of μm. We note this approach differs from the Fresnel peak band measurement techniques used for Ganymede NIRSpec data by (Bockelée-Morvan et al., 2024a; Trumbo et al., 2023a) and for Europa (Cartwright et al., 2025). In those articles, the authors report band areas that are normalized by the underlying continuum. However, as a reflectance, and not absorption or emission feature, the Fresnel peak is not a function of the underlying continuum. Additionally, we perform a preliminary analysis of the broad OH 3 μm feature using a modified approach. Because the NIRSPec data presented in this work do not sample wavelengths short of 2.85 μm, we only sample about half of the full 3 μm absorption feature. As such, we do not attempt to fit the full feature with a gaussian profile. Instead, we fit the bottom portion of the absorption feature between 2.9-3.05 μm with a small gaussian to locate the band minimum. To approximate the continuum, we simply fit a constant model in the portion of the spectrum from 4.64-5.1 μm.

Retrieval of gaseous CO_2: Although Callisto's spectral profile around 4.25 μm is dominated by absorption from the solid-phase CO_2, weak gaseous features can

be extracted from this same wavelength range via a careful treatment of the continuum. This procedure for JWST NIRSpec observations was first demonstrated at Callisto (Cartwright et al., 2024), and has since been applied to Ganymede (Bockelée-Morvan et al., 2024b). Here, we reiterate the primary details of this extraction. Solar-pumped molecules of CO_2 gas produce a fluorescent emission band in the 4.2 to 4.3 μm spectral range. This band is divided into two groups of features called the P and R branches. These branches are further divided into narrow emission features that are resolvable at the resolution of NIRSpec's G395H grating (R ∼3000 at 4.25 μm). These lines are separated from the solid-phase CO_2 absorption by generating a smoothed Callisto spectra between 4.2 and 4.3 μm (R = 1000) that only retains the shape of the solid-phase profile. This smoothed continuum profile was then subtracted from the native resolution NIRSpec data (R ∼ 3000), to isolate the residual CO_2 gas emission features. We performed this technique on all spaxels covering Callisto's disk and a ∼0.3″ wide annulus of spaxels beyond its disk to search for CO_2 gas over a range of altitudes above its surface (∼1000 km). Next, the residuals containing the gaseous emission lines were compared using cross-correlation to synthetic spectra of varying CO_2 concentrations generated by PSG. The output of this approach is an estimate of the average line-of-sight CO_2 gas column density as seen by the observer. This line-of-sight was not corrected for the observing geometry (i.e., incidence and emission angles). For our PSG model, we assume that the excitation process is photon-dominated, rather than electron-dominated. An assessment of CO_2 electron excitation, employing an electron population comparable to that used for analyzing ultraviolet emissions (Cunningham et al., 2015; Roth, 2021), indicates minimal contributions (<0.1 percent), reinforcing solar-pumped fluorescence as the primary excitation mechanism at Callisto. The observation rms and χ^2 statistics between the finalized continuum model and the data informed the 1σ uncertainties for the resulting CO_2 column density estimates.

4.3 Results

The Distribution of the Fresnel Peak

Our map of the band area of Callisto's Fresnel peak demonstrates that H_2O ice is not homogeneously distributed across the moon (Fig. 4.1). Instead, this H_2O ice feature exhibits leading vs trailing hemisphere differences, as well as localized enhancements related to regional geology. In addition to the Fresnel peak maps, we show sample spectra from the three observations (Fig. 4.2) and highlight the improved spectral resolution of JWST NIRSpec compared to Galileo NIMS. In this section,

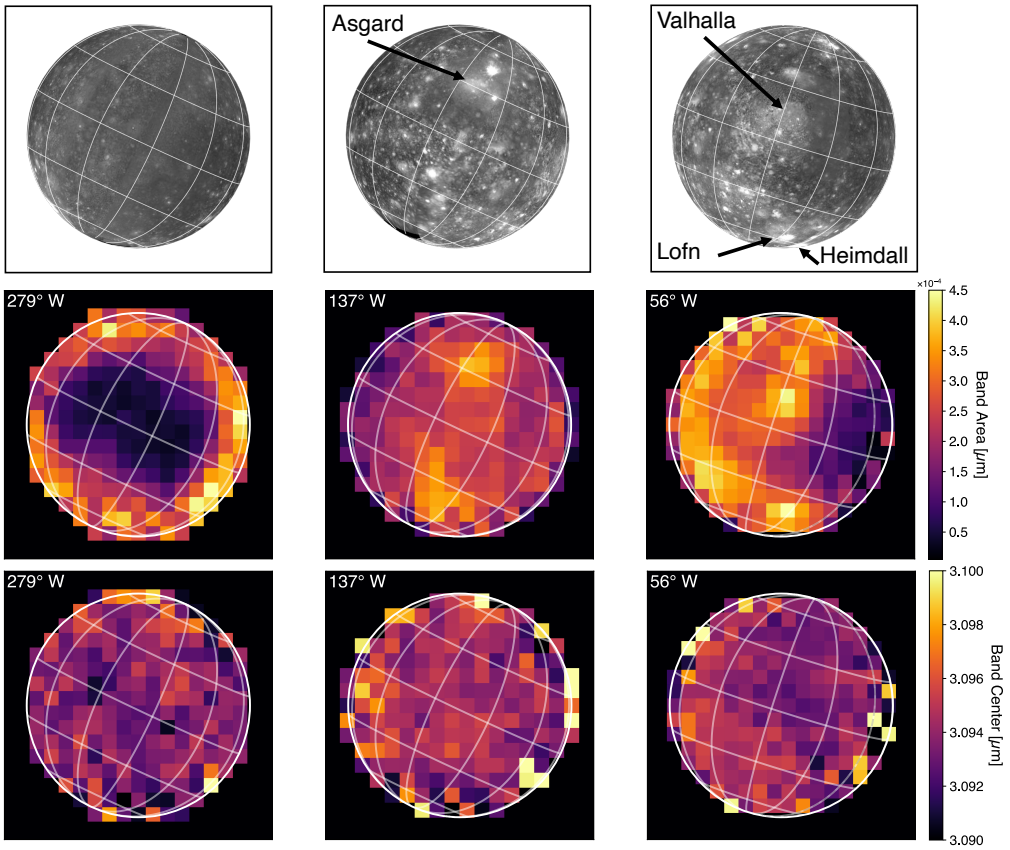

Figure 4.1: The band areas and centers of Callisto's Fresnel peak as measured at 3.1 µm for three viewing geometries. The top three panels are projected USGS albedo maps of Callisto, and have been stretched to allow for easier identification of the major geologic terrains. The bottom three panels are our measured band areas. The white circle on each bottom panel denotes the radius of Callisto. Latitude and longitude lines are spaced in 30° increments. The sub-observer longitude of the observation is indicated in the panels. The projected angular size of Callisto varies slightly between each observation, so the spaxel scale is slightly different in each panel.

we describe these major behaviors of Callisto's Fresnel peak area.

Leading vs Trailing Hemisphere: The Fresnel peak is clearly different on the trailing hemisphere in both strength and spatial distribution compared to the leading hemisphere. We find band areas are larger on Callisto's leading hemisphere than they are on the trailing hemisphere. The average trailing hemisphere band area is $\sim 1.9 \times 10^{-4}$ μm, while the averages for the Asgard and Valhalla observations are $\sim 2.2 \times 10^{-4}$ μm and $\sim 2.5 \times 10^{-4}$ μm, respectively. The ratio of the band areas of the Asgard and Valhalla observations is ∼1.2 times greater than the average band areas of the trailing hemisphere. Additionally, the trailing hemisphere exhibits a distinct bullseye pattern with smaller band areas concentrated at low latitudes, and increasing band strengths at high latitudes and toward the anti-Jovian and sub-Jovian limbs, while the Asgard and Valhalla observations do not exhibit this pattern. Instead, the largest band areas on the two leading hemisphere observations form more complex groupings.

Localized Enhancements on Asgard and Valhalla: For the Asgard-centered observation, there are localized regions of elevated band areas. The impact basin Asgard is centered near 32° N, 140° W, an area co-located with a group of higher-intensity Fresnel peaks. A representative value for this area is $\sim 3.7 \times 10^{-4}$ μm, which is ∼1.4 times greater than neighboring pixels at similar latitudes. Another smaller (D∼610 km) multiring basin, Utgard, is just north of Asgard's center at 45° N, 134° W and may be contributing to the elevated band areas. In the southern hemisphere, more to the east, there is another group of spaxels with increased band areas, which are spread over a slightly larger area than those clustered near Asgard. Beyond these two regional enhancements, the Fresnel band area measurements across the Asgard-centered observation are fairly uniform.

Similarly, we find additional enhancements of the Fresnel peak on the Valhalla-centered observation. The dominant feature in the center of Callisto's disk for this observation is the increased band area near the center of Valhalla, close to 14° N, 56° W. The band areas of pixels near the center are $\sim 4 \times 10^{-4}$ μm. Just above these bright pixels is another area that could possibly be linked to the additional bright craters seen on the albedo map. In the south, we find larger swaths of higher band areas, including one region that appears co-located with Lofn near −56° N, 22° W. Beyond these broad enhancements of the Fresnel peak area, we also identify a region east of Valhalla between (∼0°-30° N, 0°-30° W) that bears generally weaker band areas than the pixels to the west of Valhalla. The Fresnel peak areas in this region

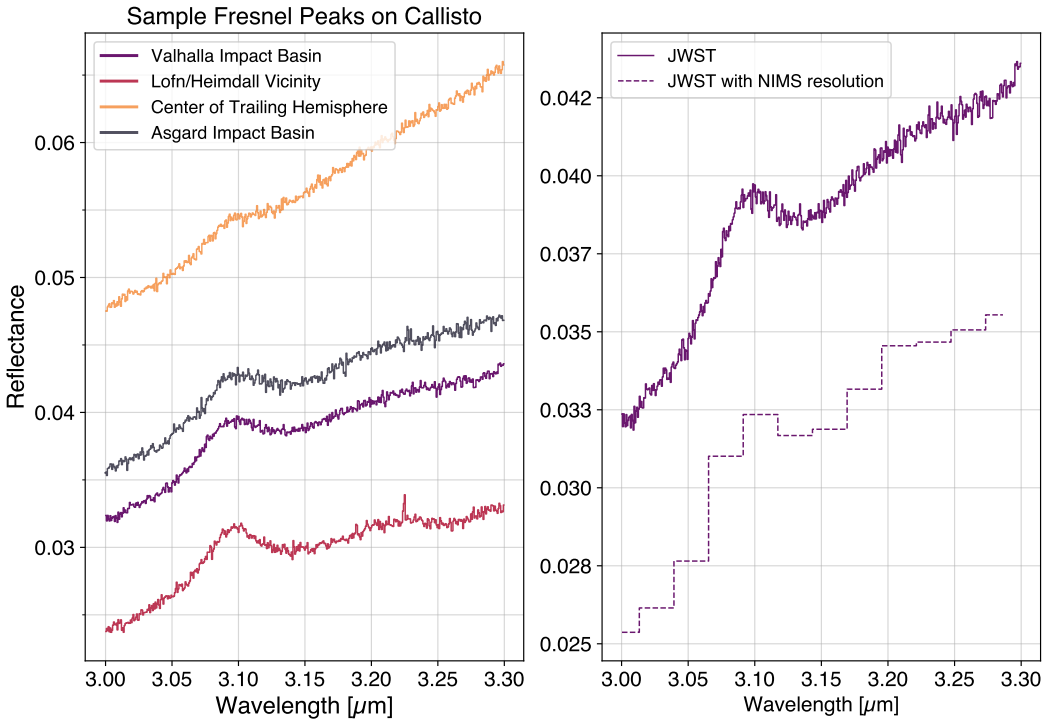

Figure 4.2: *Left:* A sample of Fresnel Peak spectra taken from the three JWST NIRSpec observations of Callisto. Each spectrum represents data from one representative spaxel for each of the locations listed. The spectra are shown prior to continuum subtraction. The Fresnel peak is smaller and more muted across most of Callisto's trailing hemisphere. On the leading hemisphere, spaxels that overlap with Callisto's major multi-ring basins, Asgard and Valhalla, show more defined structure. A spaxel from the Lofn/Heimdall region shows a particularly large Fresnel peak for Callisto. *Right*: A comparison of a Fresnel peak from a JWST spaxel to how that data would look if sampled every ∼0.026 μm to simulate the resolution of NIMS near 3 μm (Hansen et al., 2004). This basic comparison only serves to showcase the excellent resolution of JWST compared to NIMS, not the sensitivity difference.

are ∼0.5× lower than the Valhalla-observation full-disk average.

The Distribution of the 4.25 μm CO_2 Feature

The map of the band depth of the 4.25 μm CO_2 on the Valhalla-centered hemisphere displays a diffuse distribution with a notable southern hemisphere enhancement (Fig. 4.3). The disk-average CO_2 band depth is ∼19 percent, while the enhanced pixels near 0°W and −45°N are closer to ∼25 percent. These CO_2-rich pixels are geographically near Callisto's most prominent southern hemisphere impact features, mainly Lofn and Heimdall (−63°N, 357°W). We find the CO_2 is concentrated more

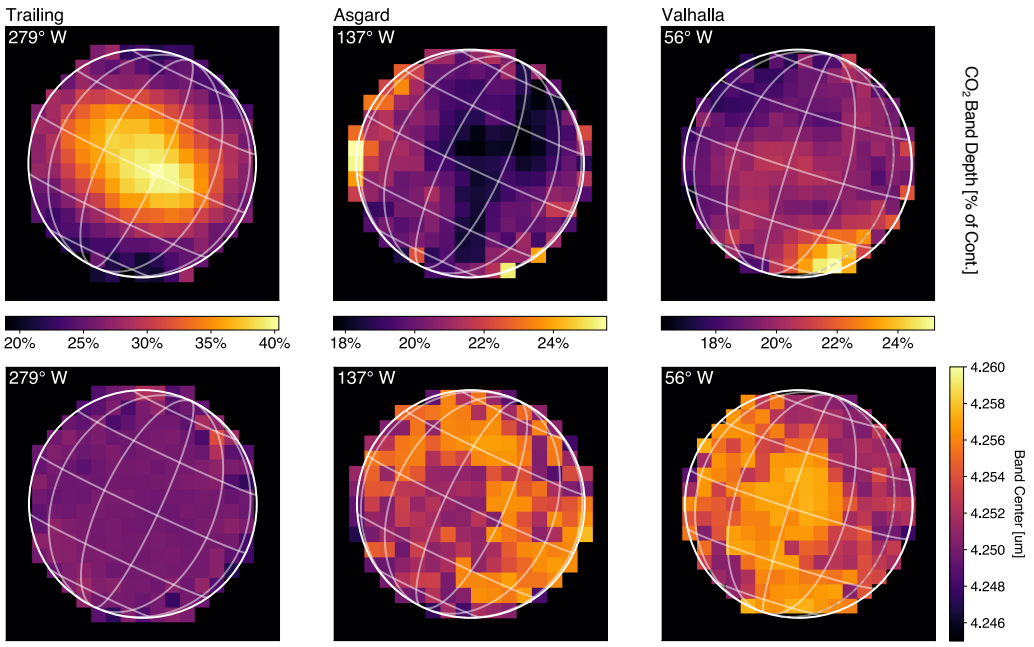

Figure 4.3: The band depths of Callisto's CO_2 as measured at 4.25 μm for three viewing geometries. The trailing hemisphere and Asgard-centered data were previously published by Cartwright et al. (2024). The white circle denotes the radius of Callisto. Latitude and longitude lines are spaced in 30° increments. The sub-observer longitude of the observation is indicated in the panels. The projected angular size of Callisto varies slightly between each observation, so the spaxel scale is slightly different in each panel. Interpretation of noisier pixels that fall along the disk edge is not recommended.

so at low latitudes than at high latitudes. In contrast to the Fresnel peak data, Valhalla is not clearly distinctive in the CO_2 distribution. Although much of Valhalla overlaps with where the low-latitude CO_2 is, the CO_2 is not concentrated in "round" group of pixels in the same way that the strongest Fresnel peaks are congregated. In Fig. 4.4, we present example spectra from spaxels in the vicinity of Valhalla as well as near the Lofn/Heimdall region.

In addition to detecting solid-phase CO_2 across this hemisphere, we report the detection of gas phase CO_2. The characteristic sawtooth pattern of the ν_3 fundamental vibration of gaseous CO_2 is seen in the residuals (left panel of Fig. 4.5). As seen in the right panel of Fig. 4.5, the NIRSpec spaxels with the highest column densities ($>1.1 \times 10^{19}$ m^{-2}) are clustered together in a region in the northern hemisphere.

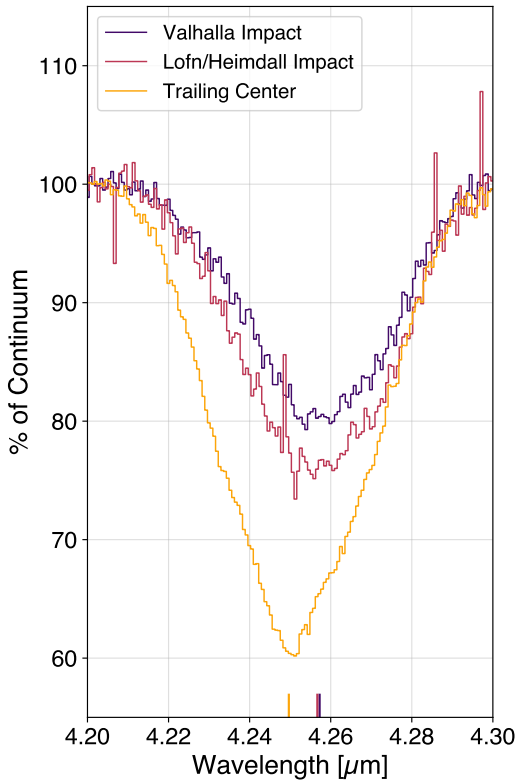

Figure 4.4: Sample continuum-divided CO_2 absorption features extracted from individual spaxels for select terrains on Callisto. Sampled regions include a spaxel from near the center of the Valhalla impact basin, a spaxel from the CO_2 enrichment near the Lofn/Heimdall impacts in the southern hemisphere, and a spaxel from the center of the trailing hemisphere. The vertical lines at the bottom of the plot indicate the best-fit band center for each spaxel.

The Distribution of the 4.57 µm Feature

In addition to maps of the 3.1 µm Fresnel peak and the 4.25 µm CO_2 absorption feature on Callisto's Valhalla-centered observation, we also provide a new map of the 4.57 µm band depths (Fig. 4.6. Focusing on pixels closer to the disk center rather than the noisier edge pixels closer to the limb, we identify possible areas of interest. Per the map, it appears that the 4.57 µm is depleted in the materials in the center of Valhalla relative to nearby terrain of similar latitude. There is another possible group of weaker 4.57 µm band depths to the southwest of Valhalla's center, roughly between 0 to 30°W and 0 to 30°N.

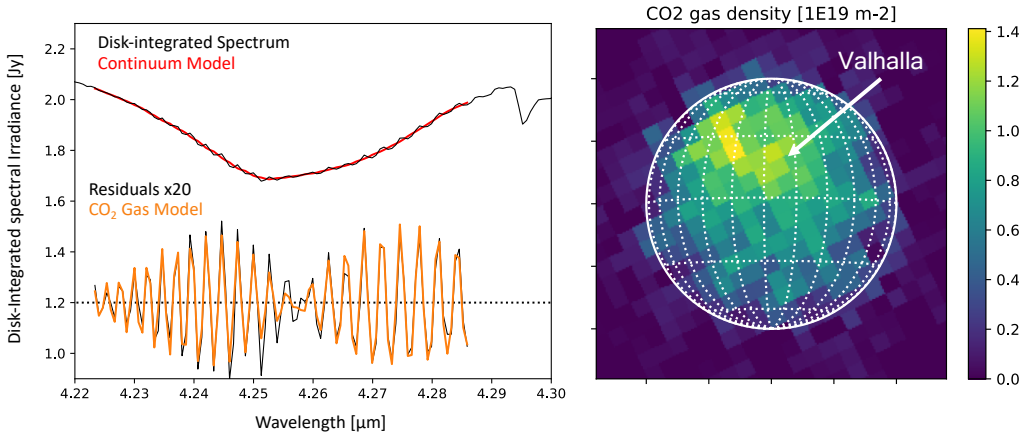

Figure 4.5: A detection of CO_2 gas on the Valhalla-centered observation using JWST. *Left panel:* A slice of the disk-integrated NIRSpec spectrum containing the 4.25 μm absorption feature (black). This absorption feature is dominated by solid-phase CO_2 to which a continuum was fit (red). The subtraction of the continuum from the data reveals the much weaker gas phase signal (black, bottom). The fit of the CO_2 gas-phase model is shown in orange. *Right panel:* The column density of CO_2 gas across Callisto's disk.

4.4 Discussion

The Geologic Origins of Callisto's 3.1 μm Fresnel Peak

In the results section, we presented a high-sensitivity, comprehensive map of Callisto's 3.1 μm Fresnel feature. Because these Fresnel peaks are generated by the first reflection of light off a H_2O crystal, these maps can be interpreted as a "first-pass" approximation of the areal exposure of H_2O ice on Callisto's surface. However, it is important to emphasize the intensity, shape, and band center of the Fresnel peak are functions of factors including temperature, grain size, and crystal structure (i.e., crystalline vs amorphous) (Stephan et al., 2020; Hansen et al., 2004; Mastrapa et al., 2009). It is beyond the scope of the current work to include these factors in our analysis, as it would require detailed laboratory experiments and robust radiative transfer modeling. As such, we publish these Fresnel peak area maps as a "first-pass" at Callisto's H_2O ice distribution as observed by JWST, much like the approach taken for the JWST Ganymede Fresnel peak maps by Bockelée-Morvan et al. (2024a). These "crystalline" results are complemented by recent work by Cartwright et al. (2025) on analyzing the state of H_2O ice across the surface of Europa using JWST.

The Fresnel maps presented here represent a step forward in quality compared to the prior Galileo NIMS dataset. As illustrated in Fig. 4.2, the better resolution of

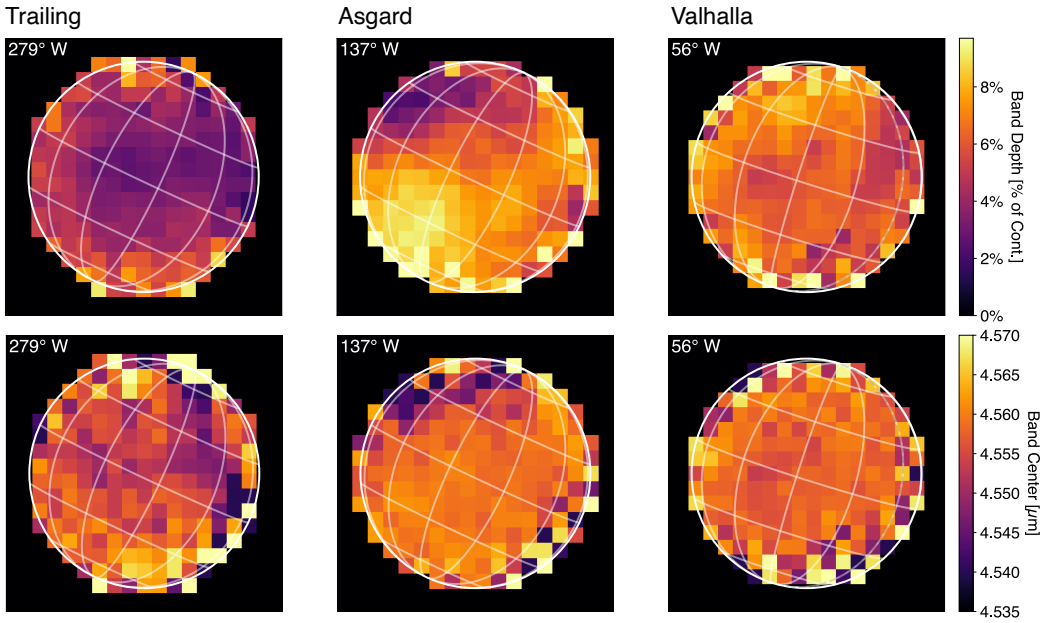

Figure 4.6: The band depths and centers of Callisto's 4.57 μm for three viewing geometries. The trailing hemisphere and Asgard-centered data were previously published by Cartwright et al. (2024). The white circle on each panel denotes the radius of Callisto. Latitude and longitude lines are spaced in 30° increments. The sub-observer longitude of the observation is indicated in the panels. The projected angular size of Callisto varies slightly between each observation, so the spaxel scale is slightly different in each panel.

JWST allows for a higher fidelity extraction of features compared to the NIMS data. Because Callisto has relatively little exposed ice (∼10 percent areal coverage), the 3.1 μm signal in individual NIMS pixels was weak. As a result, Hansen et al. (2004) did not present a global map of the feature, but instead report averages of icy pixels from five large regions. Other maps of H_2O spectral features using NIMS data include the 1.48 μm band depths mapped by Hibbitts et al. (2000) and McCord et al. (1998), as well as by Stephan et al. (2020). In this work, we primarily use the 1.48 μm band depth map in Hibbitts et al. (2000) as a point of reference, as the band depths are presented as a global map, allowing for a straightforward comparison between our data and the Callisto geologic map (Greeley et al., 2000).

Interpretation of Regional Fresnel Peak Trends (Leading): Indeed, as shown in Fig. 4.1, the Fresnel peak band appears tightly tethered to regional geology on Callisto's leading hemisphere in both the Valhalla-centered and Asgard-centered observations. The intensity is stronger in the large impact basins, Asgard and Valhalla

(Fig. 4.1). This finding is consistent with their general bright albedos and previous evaluations of Callisto's H_2O ice distribution, including Hibbitts et al. (2000). For the large multi-ring impacts, Valhalla and Asgard, the pixels with the highest intensity Fresnel peaks appear to be contained to the center regions of the crater, with a drop off in strength toward the outer rims. This is mirrored in the albedo maps, which show the the brightest material of these craters is similarly retained by the impact centers. Supporting these JWST results are millimeter/submillimeter observations of Callisto using ALMA, which show the Valhalla impact region is co-located with a thermal cold spot discernible in model residuals spanning 97-343 GHz Camarca et al. (2023), Camarca submitted. This cold spot may be explained if there is higher thermal inertia material present that suppresses daytime temperatures in the crater center, and/or lower emissivity materials, both of which are consistent with exposed H_2O ice. Moreover, the dimensions of the JWST NIRSpec pixel are comparable to the ALMA beamsize (within a factor of ∼2.5 for the beam major axis) for the Callisto observations, and we find the spatial extent of the largest Fresnel peaks in this area to be comparable to the size of cold spot in the ALMA data (of order $<0.3''$).

The large-impact enhancement in the Fresnel peak intensity is accompanied by smaller geologic units with similar levels of enhancement. On the Asgard-centered observation, the other group of more intense Fresnel peaks located near 130° W, 45° N may be associated with a pair of overlapping "lp" (light plains) units noted in the Greeley et al. (2000) geologic map. This pixel group appears to extend close to 60 S, however interpreting this region further is complicated by the geologic map at this longitude being cutoff at ∼-40° N because of poor spatial resolution. On the Valhalla-centered observation, there are several pixel groups with elevated Fresnel intensity that are likely sampling smaller impact features. The Fresnel peak enhancement just north of Valhalla is likely linked to a c3 unit containing two craters near 38°N, 65°W that lies on the boundary of the Valhalla inner and outer crater units (Greeley et al., 2000). Southwest of the Valhalla center, between about 55 to 90°W and 20 to 57°S there are about 15 mapped crater units (Greeley et al., 2000) that likely explain the Fresnel peak enhancement in this area in our maps. This particular section of Callisto's geologic map appears to bear a higher density of mapped young crater units than other similarly sized sections of the geologic map. The brightest of the craters in this spatial group, Agloolik (−47°N, 82°W), appears to have partially saturated in the USGS albedo map.

In the southern hemisphere on the Valhalla-centered observation, we recover ele-

vated Fresnel band areas in the vicinity of Lofn. Lofn (−57°N, 22°W) is one of Callisto's youngest large-scale features (∼1.4-3.9 gyr) and is geologically significant because its morphology points toward a fragmented parent body that impacted obliquely into a slushy or liquid zone (Greeley et al., 2001). In particular, the ejecta units inferred to be sourced from the greatest subsurface depths are interpreted to retain impact melt, and, possibly, materials from the subsurface ocean (Greeley et al., 2001). Mapped units from Lofn partially obscure Heimdall to the southeast and Adlinda to the northwest. Heimdall is another large, bright impact feature that is largely saturated in the Galileo images, and Adlinda is possibly the oldest multiring structure on Callisto. Here, we note that the pixels we propose to be associated with Lofn/Heimdall are close to the edge of the disk, and therefore the spatial sampling of this region is poor. Therefore, it is difficult to infer the relative contributions of Lofn/Heimdall separately to the Fresnel peak. However, we infer that the contribution of Adlinda is probably not as important based on its lower albedo and less ice-rich spectra compared to Lofn (e.g., see Plate 2 in Greeley et al. 2001.) In the NIMS dataset, the Fresnel peak was extracted from the Lofn region as the representative high-latitude, Jovian-facing spectra (Fig. 8, Hansen et al. 2004) and exhibits the same two-component structure in the same wavelength region as our extractions (Fig. 4.2). Altogether, we find the Lofn/Heimdall region, along with the large multiring basins and smaller crater units described in the previous paragraph, are the primary terrains with elevated 3.1 μm Fresnel band areas on the leading hemisphere. This suggest the distribution of Callisto's leading hemisphere water ice exposure primarily geology (i.e., impact) driven. Here, we now turn to describing a region with depleted 3.1 μm Fresnel peaks on the leading hemisphere.

A new region of interest Although the salient feature of Callisto's leading hemisphere is larger Fresnel band areas and their preference for the large impact craters, the terrain just east/southeast of Valhalla stands out for its weaker Fresnel band areas. This "depleted" region is fairly large compared the spatial scale of individual groups of high-intensity Fresnel peaks, and may exhibit some amount of curvature around Valhalla. The dominant geologic unit in this region is a cratered plains unit, the dominant terrain on Callisto as readily observed in the Greeley et al. (2001) geologic map. As summarized by Greeley et al. (2001), the crater plains terrain appears to be more ice-poor/possibly silicate rich than the centers of the large icy impacts (Carlson et al., 1996; McCord et al., 1997). Although this context helps explain why this region bears depleted Fresnel peaks relative to the icy craters, more information is required to explain why this region is depleted compared to other swaths of leading

hemisphere crater plains terrain. Our results do appear consistent with the albedo map, as this region appears darker than much of cratered plains unit sampled by the Asgard-centered observation. The 1.48 μm band depths are approximately <10 percent in this area (Hibbitts et al., 2002).

Notably, this Fresnel-depleted region appears to overlap with a thermal anomaly reported in the ALMA data. In Camarca et al. (2023), a region about ∼3 K warmer than model predictions (which account for albedo) in a 345 GHz observation was noted in the region just southeast of Valhalla near −15°N, 45°W; this warm terrain was also detected in the 233 and 97 GHz data (Camarca, submitted). As described by Camarca et al. (2023), this region may be consistent with locally low thermal inertia terrain, e.g., more texturized, loosely compacted regolith. Such regolith could be plausibly generated by preferential micrometeorite bombardment at low-latitudes on the leading hemisphere (a similar process was hypothesized to explain the Ganymede ALMA data de Kleer et al. 2021). This micrometeorite hypothesis may be linked to the Fresnel peak if the locally warm terrain has allowed for shallow ice to sublimate away. Such a scenario bears similarities to processes proposed for Iapetus, which is suspected to have removed equatorial water ice via sublimation due to the exogenically-derived Cassini Regio (Spencer et al., 2010). A caveat to this explanation is that, although this region is observed on the leading hemisphere, it not centered at Callisto's apex of motion (90° W). Altogether, this interpretation presents an alternative to the suggestion that impacts excavate subsurface H_2O ice, as was posited by Bockelée-Morvan et al. (2024a) to explain the Ganymede JWST Fresnel peak maps. Here, it is necessary to emphasize that the balance between the endogenic and exogenic origin of dark material on Callisto is a major outstanding question for this satellite, which motivate the acquisition of additional telescope observations for this region.

Ice migration? Another application of the Fresnel peak map is to evaluate an icy moon for evidence of the migration of ice crystals. As reported by Bockelée-Morvan et al. (2024a), the strength of the Fresnel peak on the trailing hemisphere appears to favor the morning limb. Such a distribution could be explained if the morning limb excess represents an accumulation of ice particles that have yet to be sublimated away in the daytime heat. In this work, we do not recover obvious evidence for a morning sublimation front. There is potentially evidence for the afternoon limb on the trailing hemisphere bearing elevated Fresnel band areas. However, because the strength of Callisto's Fresnel peak is much weaker than those on Ganymede, pixels

near the disk edge must be interpreted with greater caution. If this limb brightening is real, it may not be distributed evenly above/below the 0°N line in the same manner the Ganymede Fresnel peak is. If this limb brightening was only controlled by geology, that unit would be located at near 210° W, and we do not recover a similar limb brightening for this longitude at the morning limb of the Asgard-centered observation.

Ice Crystallinity on Callisto: One of the interesting diagnostics that can be derived from analysis of the Fresnel peak is whether the crystal is amorphous or crystalline. At Galilean satellite temperatures, the Fresnel peak is broad and weak for amorphous ice, and strong and structured for crystalline ice (Hansen et al., 2004). The identification of amorphous ice on the Galilean satellites is of interest given the dependence of ice crystallization on factors including temperature and the radiation environment. For example, Jenniskens et al. (1996) show that for a modest change in temperature from ∼105-125 K, the change in the crystallization timescale is a factor of 10^5 faster. The laboratory work by Jenniskens et al. (1996) points to thermal recrystallization timescales for 150 K temperatures of order 10 seconds, with timescales under 1 minute for this same temperature including porosity-dependent measurements by Mitchell et al. (2017). The paradigm established by analyses of the NIMS data is that radiation works quickly to produce amorphous ice on Europa, with some available on Ganymede, while thermal crystallization dominants at Callisto Hansen et al. (2004). The presence of amorphous ice at Ganymede's north pole was recovered by Bockelée-Morvan et al. (2024a) using JWST NIRSpec. In the Ganymede data, the Fresnel peak is clearly broad with a lower band center reported at 3.05 μm. Laboratory work by Stephan et al. (2020) demonstrates that the band center of the Fresnel peak can shift closer to 3.09 μm in 150 K crystalline ice, which is broadly consistent with our band center measurements (Fig. 4.1).

Interpretation of Leading vs Trailing: Our finding that Fresnel peak band areas are smaller on the trailing hemisphere than on the leading hemisphere is consistent with the trend observed on Callisto's neighbor, Ganymede (Bockelée-Morvan et al., 2024a). This is apparent by comparing example leading/trailing hemisphere spaxels here (Fig. 4.2), as well as in the disk-integrated leading/trailing spectra presented in Fig. 4 in Cartwright et al. (2024) with Fig. 4 of Bockelée-Morvan et al. (2024a). The contrast in the leading/trailing hemisphere measured here of ∼1.4 x is much lower than the contrast of >10 reported for Ganymede. As summarized in Bockelée-Morvan et al. (2024a), the Fresnel peak may be strengthened on the

leading hemisphere of Ganymede due to more ions on the leading hemisphere that sputter fresh ice, as well as the effect of increased meteorite flux excavating the ice. Cooper et al. (2001) found that the Jovian radiation density is 10x lower at Callisto than Ganymede, and Johnson (1990) calculated the effectiveness of sputtering on ice to be much less effective at Callisto compared to Ganymede and Europa. Therefore, it is reasonable to infer that Callisto's more muted leading/trailing Fresnel peak asymmetry may be due in part to a weakening of the processes that would otherwise enhance this asymmetry. In the prior key work on Callisto's Fresnel peak, the presented global "leading" and "trailing" hemisphere Fresnel peaks appear to show that the trailing hemisphere Fresnel peak is stronger (Hansen et al., 2004). This would be a discrepancy with the results here, as well as Cartwright et al. (2024). However, the Fresnel peaks reported in Hansen et al. (2004) for Callisto are based on the average spectra of icy pixels that have an averaged dark material spectrum subtracted from them. The spatial resolution of the NIMS pixels (<120 km) used for this analysis is much smaller than the hundreds of km footprint of JWST NIRSpec. This difference in methodology precludes a one-to-one comparison of the Fresnel peaks, but given the increased sensitivity of JWST over NIMS, our result that, globally, the Fresnel peak is weaker on the trailing hemisphere than the leading is a robust finding.

Interpretation of Regional Fresnel Peak Trends (Trailing): In addition to a difference in the intensity of the Fresnel peak between the leading and trailing hemispheres, there are also sub-hemisphere variations. On the trailing hemisphere, the primary trend is an increase of peak area toward the high latitudes (Fig. 4.1). A similar trend is discernible the map of the 1.48 μm band depth on Callisto in Hibbitts et al. (2000), which also increases toward high latitudes. Moreover, the map of Ganymede's Fresnel peak on the trailing hemisphere also exhibit this behavior (Bockelée-Morvan et al., 2024a). Laboratory work by Stephan et al. (2021b) demonstrates that the intensity of the Fresnel peak decreases with increasing temperature. This result would predict that Callisto's equatorial Fresnel peak should be weaker, which would be consistent with our trailing hemisphere map, but not our leading hemisphere maps. This suggests another processes is required to help explain the trailing hemisphere Fresnel peak bull's eye. Is grain size a main factor? The laboratory data demonstrate that increasing the grain size of H_2O ice will increase the Fresnel peak intensity across the 70-150 K range for grains of order 70-1300 μm. A detailed analysis of NIMS data by Stephan et al. (2020) using the 2 μm and 1.5 μm features find that Callisto's trailing hemisphere has an apparent bull's eye pattern, that imply larger grains at the equator, and smaller grains at the poles. Based on grain size alone, this

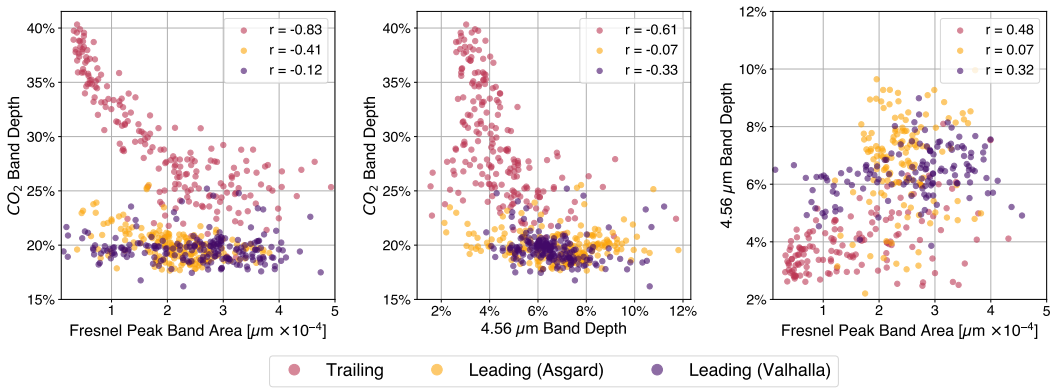

Figure 4.7: Correlation diagrams for the strength of the three volatiles surveyed in this work. For the third panel comparing the H_2O ice Fresnel peak and the 4.57 µm feature, we excluded the pixels that fall along the projected radius of Callisto.

result would predict a larger Fresnel peak at the equator and a smaller one at the pole on the trailing hemisphere, which is opposite to our result. In the next section, we speculate on whether or the large presence of CO_2 on Callisto's trailing hemisphere is related. First, we will evaluate the geologic setting of Callisto's CO_2, including on the new Valhalla-centered observation.

Placing Our CO_2 Results in Context

Solid-phase CO_2: We find that our map of CO_2 on Callisto's Valhalla-centered hemisphere as observed with JWST NIRSpec is consistent with past observations of this volatile. Our results are consistent with the analyses of McCord et al. (1998) and Hibbitts et al. (2000) that CO_2 band depths are weaker in Callisto's polar regions compared to lower latitudes. The average CO_2 band depth measured for the Valhalla-centered observation of ∼19 percent appears consistent with the CO_2 map provided by Hibbitts et al. (2000), although the Galileo map includes much finer spatial resolution observations that showcase elevated CO_2 in smaller craters well below the resolution of a NIRSpec pixel. The inter-crater band depths in the Hibbitts et al. (2000) map appear to be ∼15 percent, while the dotted areas of elevated CO_2 in small craters appears to be ∼30 percent. The average CO_2 band depth measured for this Valhalla observation is much lower than those measured on the trailing using JWST data by Cartwright et al. (2024), again consistent with past analyses (Hibbitts et al., 2000; McCord et al., 1998).

Moreover, we find that our recovery of an enrichment of CO_2 in the vicinity of the large Lofn/Heimdall impacts agrees well with Galileo results. Our measured band

depths of order 25 percent are comparable to those measured at higher resolution with NIMS, although there are several regions below the NIRSpec resolution in the Hibbitts et al. (2000) map that have band depths upwards of 40 percent. In the Hibbitts et al. (2002) dedicated analysis of CO_2-rich craters on Callisto, Lofn is not specifically analyzed, nor is the origin of CO_2 in Lofn specifically considered by Greeley et al. (2001). As shown in Figs. 4.3 and 4.1, both the center of Valhalla and Lofn are ice-rich regions per the Fresnel peak map, and sample JWST spectra for these impacts are morphologically similar, suggesting a comparable host material for the solid-phase CO_2 (Figs. 4.4). As discussed earlier, Lofn may retain H_2O ice melt possibly derived from a subsurface liquid/slushy zone. Therefore, we evaluate the NIMS dataset in combination with these new JWST results to evaluate the origin of CO_2 in the vicinity of Lofn.

First, we consider the evidence for CO_2 derived from a deep subsurface slushy/liquid zone. Here, it is important to emphasize we are not exploring a *recent* source. Although Lofn is young by Callisto standards, its age (at minimum ∼1.4 gyr, Wagner et al. 1999; Wagner et al. 1998) does not qualify as young by general Galilean moon standards. The most promising example of young, subsurface-derived CO_2 in the Galilean system is the extraction of strong, double-lobed absorption features near Tara Regio on Europa (Trumbo et al., 2023b; Villanueva et al., 2023a). Here, we evaluate if the CO_2 in Lofn/Heimdall appear connected to the water-rich ejecta deposits. Based on the high-resolution NIMS dataset, this does not appear to be the case. There are several units of impact ejecta described in the Greeley et al. (2001) Lofn geologic map, and ejecta material streaks enriched in H_2O ice are discernible in the 1.48 μm map. By contrast, in the NIMS map, CO_2 is distributed very broadly across the entire Lofn unit with no apparent correlation with the excavated H_2O ice or decrease in band depths with distance from the crater center. As described by Hibbitts et al. (2002), CO_2 rich craters on Callisto may follow a depletion pattern whereby the ice is first depleted from the ejecta blanket, then the crater rays, and lastly the crater itself. A subsurface liquid origin for the CO_2 in Lofn is also complicated by the fact the much older, adjacent Adlinda multi-ring basin is similarly enriched in CO_2 in the NIMS map. As such, in light of the present data, a deep subsurface origin for the majority of Lofn's CO_2 seems unlikely. Why then might this region be enhanced in CO_2? It has been demonstrated that thermal properties of large impact features on Ganymede and Callisto are consistent with the presence of locally high thermal inertia materials (de Kleer et al. 2021; Camarca et al. 2023, Camarca et al. submitted). The Lofn/Heimdall/Adlinda region is observed to be

colder in model residuals at 97-345 GHz than other terrains of similarly high latitude. As such, it is possible that CO_2 is preferentially being cold trapped in these areas.

CO_2 and exposed H_2O ice on the trailing hemisphere: Earlier in the discussion section, we highlighted that the trailing hemisphere Fresnel peak distribution appears to be an "inverted" bull's eye pattern, with depletion at the disk center (Fig. 4.1). Here, we compare this pattern to the well-known CO_2 bullseye pattern, which features an enrichment at the disk center. In Fig. 4.7, we show that the strength of the Fresnel peak band area is anti-correlated with the band depth of the CO_2 feature. If we interpret this anti-correlation as a tradeoff in the relative abundance of CO_2 and H_2O ice on Callisto's trailing hemisphere, there are several possible explanations. First, the production of the CO_2 on Callisto's trailing hemisphere is radiolytic, and may proceed via chemistry between dark, C-rich material and H_2O ice, a process supported by laboratory investigations (e.g., Raut et al. 2012; Mennella et al. 2004). Therefore, the areas of high radiolytic CO_2 production may have depleted a region of feeder H_2O molecules. However, Moore et al. (2004) suggest that irradiated H_2O ice is not sufficient to explain the CO_2 abundance as it would require the H_2O ice to migrate into the dark, non-ice material before escaping to space. Results from Galileo demonstrate that H_2O ice and non-icy material exists on scales below a few km (the best NIMS resolution), however higher-resolution Solid State Imager (SSI) images show light/dark patches at the scale of tens of meters, and areal mixing might even occur at cm levels (Moore et al., 2004; Spencer, 1987). Alternatively, it is possible that the presence of highly-volatile CO_2 in the regolith promoted the sublimation of H_2O away from equatorial latitudes. For example, work by Moore et al. (1999) concluded that Callisto's greater share of sublimation-driven landform modification relative to Ganymede is likely driven by the greater abundance of CO_2 on Callisto. Lastly, it is possible Callisto's low-latitude trailing hemisphere ice is preferentially sputtered away by the impinging plasma. The latitude dependence of ions, such as O+, H+, can be visualized through models tethered to Galileo magnetometer measurements (e.g.,Vorburger et al., 2019). In summary, the story of how radiolytic CO_2 generation and its possible links to interpreting surface ice measurements is clearly a complicated one to write with a coherent narrative across temperature, grain size, and areal exposure constraints. Future work to tether surface chemistry with the proper sources and sinks of CO_2 and H_2O on Callisto's trailing hemisphere in the context of the local plasma environment would be incredibly useful in understanding this puzzling moon.

Gas-phase CO_2: In addition to our maps of CO_2 ice on Callisto's leading hemisphere, we also present a new map of the distribution of CO_2 gas on the leading hemisphere (Fig. 4.5). The peak column densities of individual spaxels on this Valhalla-centered observation $\sim 1.4 \times 10^{19}\ m^{-2}$ appear higher than representative $\sim 1.0 \times 10^{19}\ m^{-2}$ pixels observed on the trailing hemisphere and the other Asgard-centered hemisphere observation (Cartwright et al., 2024). As before with the prior CO_2 gas maps, the distribution of this molecule in the atmosphere is quite patchy. The CO_2-gas enriched pixels in the prior Asgard observation appeared spatially correlated with the edge of Valhalla, which is generally consistent with the distribution of gas found here with this more favorable viewing geometry of the basin. The CO_2-gas rich spaxels here appear more tightly clustered near/above 30 N than is obvious in the Asgard observation. This high-latitude clustering is comparable to the pattern of CO_2 gas observed on Callisto's trailing hemisphere by Cartwright et al. (2024), for which the peak column densities largely occupied latitudes >30 S. In addition to these latitudinal similarities, the leading (Valhalla) and trailing hemisphere peak CO_2 gas clusters appear to be similarly sized (e.g., a few spaxels across). Moreover, the surprising finding from Cartwright et al. (2024) that the Callisto's trailing hemisphere gaseous CO_2 peaks (near -45 N, 280 W) in a different location than the largest trailing hemisphere solid-phase CO_2 band depths (near 0 N, 270 W) is repeated in an even more dramatic fashion in this new Valhalla-centered observation. As seen by comparing the results in Fig. 4.5 and in Fig. 4.3, the cluster of peak CO_2 column densities is emplaced close to the opposite side of the disk from the solid-CO_2 enriched region in the southern hemisphere near the Lofn/Heimdall impacts. As seen in Fig. 4.5, the primary CO_2 gas cluster is close to, but offset to the northwest, from the center of Valhalla. It does appear there is a modest increase in the CO_2 column density near the center of Valhalla compared to the rest of the disk, however. On the Greeley et al. (2000) geologic map, the notable unit that is northwest of the Valhalla center is a pair of two bright, young "c3" crater units slightly east of the peak CO_2 pixels.

If these small craters, as well as Valhalla, are the origin of the gaseous CO_2 on Callisto's leading hemisphere, it remains puzzling why the Lofn/Heimdall region is seemingly insignificant in terms of CO_2 gas despite being the primary solid CO_2 reservoir on this face of the moon. One explanation might be that the Lofn/Heimdall region is at a geographic disadvantage with regard to participating in the processes expected to drive the transfer of CO_2 to the atmosphere from the surface–sublimation and sputtering, which dominate at low latitudes. However, this does not explain

why peak CO_2 gas at Callisto is observed at high (roughly >30°) latitudes on both hemispheres. The role that Callisto's thermal properties play in organizing the CO_2 gas across the surface is also unclear in light of this new Valhalla-centered observation. Camarca et al. (submitted) suggested the trailing hemisphere CO_2 gas peak in Cartwright et al. (2024) might be related to a cold spot observed in the 97 GHz trailing hemisphere residuals, with cold-trapping of the gas possibly playing a role. Alternatively, Cartwright et al. (2024) suggested that the warm, sub-Valhalla detected in the ALMA residuals might promote sublimation of CO_2 in those regions. The cold trapping hypothesis is somewhat complicated by the fact that, even if Lofn/Heimdall is in a poor location to generate CO_2 gas, its thermal properties (Camarca et al. 2023, Camarca et al. submitted) and location seems more favorable for cold trapping. By contrast, if Callisto's thermally warm regions are preferentially sublimating CO_2, then why is the CO_2 gas not positioned over the sub-Valhalla warm spot identified in Camarca et al. (2023), Camarca et al. (submitted)? The release mechanism of CO_2 is likely complicated, much like the CO_2 gas on its sister moon, Ganymede (Bockelée-Morvan et al., 2024b). Of note, these CO_2 gas observations are only "snapshots" of Callisto's atmosphere—if CO_2 gas is on the move across Callisto, then our ability to diagnose the primary geologic units where the CO_2 originates is limited. These results motivate future JWST observations of Callisto to build our understanding of the time-resolved characteristics of its CO_2 atmosphere.

The 4.57 μm **Feature**

Next, we discuss the implications regarding the distribution of the 4.57 μm absorption feature in our dataset. This spectral signature was first identified on Callisto by McCord et al. (1998) using NIMS observations, and later confirmed from ground-based measurements with the SpeX instrument at NASA's Infrared Telescope Facility (Cartwright et al., 2020). More recently, its spatial distribution was mapped across the trailing and Asgard-centered hemispheres by Cartwright et al. (2024) using JWST.

The 4.57 μm feature is of particular interest due to its proposed origin in a CN-bearing structural group (McCord et al., 1997; Cartwright et al., 2024). If this assignment holds, the feature may be the planetary surface analogue to the well-known 4.62 μm band attributed to the OCN^- ion (e.g., Grim et al. 1987) in astrophysical ice settings, including protostars (Soifer et al., 1979), young stellar objects (Van Broekhuizen et al., 2005), and molecular clouds (McClure et al., 2023). Exam-

ples of detections of the 4.57 μm feature on planetary satellites include Ganymede (McCord et al., 1998), Phoebe (Coradini et al., 2008), and potentially Enceladus (Villanueva et al., 2023b).

Some key results from the Cartwright et al. (2024) JWST observations of Callisto include the finding that this feature is largely depleted on the trailing hemisphere and that the spaxels overlapping Asgard and parts of Valhalla exhibit lower band depths. In this work, we further confirm these trends. First, Fig. 4.6 demonstrates that Valhalla appears to be depleted in this feature. Typical band depths across the Valhalla-centered disk are of order ∼7%, which remain higher than those measured on the trailing hemisphere by Cartwright et al. (2024). There are two other possible regions of 4.57 μm depletion, one to the southwest of Valhalla at around 75° W, -7° N, and one to the east of Valhalla. The eastern 4.57 μm depletion overlaps with the northern part (∼30-60° N) of the spaxels with low-intensity Fresnel peaks. Determining what geologic unit is relevant to the western depletion is somewhat difficult. The depletion falls within the outer bounds of Valhalla, and appears offset from Fimbulthul Catena (a crater chain).

In the prior analyses of the 4.57 μm feature on Callisto, it was suggested that perhaps CN-bearing dust was being delivered to Callisto from the irregular satellite population (Cartwright et al., 2024; Cartwright et al., 2020). Between the first publication of Callisto JWST observations (Cartwright et al., 2024) and the present work, a key JWST observation of the Jovian irregular satellite population was obtained that allows this hypothesis to be tested. Using JWST Nirspec, Sharkey et al. (2025) procured 0.7-5.2 μm reflectance spectra of eight Jovian irregulars, including three members from the dominant satellite family by mass, the Himalia irregulars. Sharkey et al. (2025) report the surveyed Jovian irregulars do *not* possess a 4.57 μm absorption feature, but some (including Himalia) do possess absorption features at 2.7 and 3.05 μm indicative of the presence of ammoniated phyllosilicates. This result suggests that Jovian irregulars are not delivering CN-bearing dust "as is" to Callisto, but may be responsible for delivering N-bearing species to the surface that subsequently reacts with C-rich material on Callisto to yield CN-bearing products (Sharkey et al., 2025).

Moreover, the addition of the Valhalla-centered hemisphere to the 4.57 μm maps provides additional context for evaluating the balance of delivery and radiolytic processes on Callisto. For example, Chen et al. (2024) predicted that dust from the prograde Himalia family may be found at all longitudes, while retrograde satellite

dust is primarily concentrated on the leading hemisphere. Sharkey et al. (2025) do not report a detection of ammoniated phyllosilicates for any retrograde satellites, so it remains uncertain whether delivered N-bearing dust to Callisto bears any leading/trailing asymmetry. However, our finding that the 4.57 μm is elevated across both the Valhalla-centered and Asgard-centered leading hemisphere observations further emphasizes the report by Cartwright et al. (2024) that the depletion of the 4.57 μm on the trailing hemisphere is unique. As such, it is possible the dichotomy of the strength of Callisto's 4.57 μm feature may be developed post-delivery.

If the paradigm of N-rich dust being delivered to Callisto by the irregular satellites is correct, then there is a need for a suitable source of C to produce the CN-bearing species likely responsible for the 4.57 μm. Is CO_2 a relevant source? As shown in Fig. 4.7, the band depths of the 4.57 μm and the CO_2 are convincingly anti-correlated (r = -0.61) on the trailing hemisphere, and not convincingly correlated on either of the two leading hemisphere observations (r = -0.33/-0.07). If CO_2 was feeding C to N-bearing dust to produce CN-bearing products, one might expect to find greater band depths for the 4.57 μm in regions of high-CO_2 abundance, an expectation not supported by our measurements. Ultimately, a proper interpretation of how N, C, and O-bearing compounds on Callisto's surface, either delivered or endogenic, may interact to produce the observed depths of the 4.57 μm feature would be greatly aided by laboratory studies of radiolytic and temperature conditions appropriate to Callisto.

The broad 3 μm Feature

In this section, we offer a preliminary discussion of the spatial variability of the 3 μm feature on Callisto. The 3 μm absorption is a characteristic absorption of the OH stretching vibration due to H_2O ice (Ehrenfreund et al., 1996) as well as OH in minerals (e.g., Roush et al. 1990), and has been detected on all three icy Galilean moons (McCord et al., 1998). The shape and depth of this feature can be altered by many factors including abundance, grain size, and the presence of non-ice impurities. For the purposes of this work, we use the band depth map presented in Fig. 4.8 to provide a preliminary view of regions of interest that warrant more detailed future investigation. As seen by comparing the results of Fig. 4.8 to the Fresnel peak map in Fig. 4.1, there is not a direct correlation between the strength of the Fresnel peak and the preliminary depth of the 3 μm band as measured here. For example, both the 3 μm map and the Fresnel peak strength map (Fig. 4.1) recover the Asgard and Valhalla impact basins as notable terrain. However, the region with elevated Fresnel

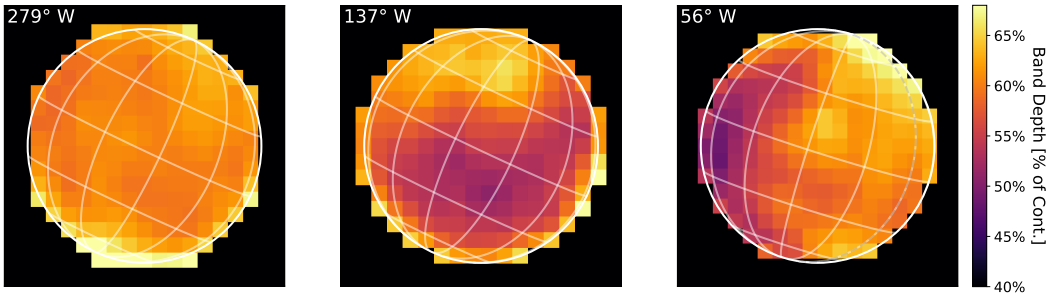

Figure 4.8: A preliminary map of the 3 μm absorption feature across Callisto. This map is preliminary because only half of the absorption feature is sampled in the current JWST NIRSpec observations, which do not contain data short of 2.85 μm.

band areas in the southern hemisphere of the Asgard-centered observation is not recovered as a notable feature in the 3 μm map. On the trailing hemisphere, the salient feature of the Fresnel band area map is the bullseye pattern with depleted areas in the disk center. By contrast, the 3 μm map in Fig. 4.8 demonstrates variation across the disk not discernible in the Fresnel peak map. Altogether, these results may further confirm that Callisto's near-surface H_2O ice and OH-bearing non-ice components vary in a non-uniform manner across the disk. A more mature analysis of Callisto's 3 μm band depth as observed with JWST would be greatly enhanced by a sampling of the satellite's spectrum shortward of 2.5 μm using NIRSpec. As demonstrated by McCord et al. (1998), the NIMS spectra show that both ice-rich and ice-free regions on Callisto bear a strong 3 μm absorption, but the ice-free regions are missing diagnostic H_2O/OH features in the 1-2.3 μm regime, suggestive of the relevance of OH-bearing minerals on Callisto.

4.5 Conclusions

In this paper, we explored the distribution of surface volatiles on Callisto's leading hemisphere using the NIRSpec instrument onboard JWST. Here, we present 1) the first global, high-resolution and high-sensitivity map of the 3.1 μm Fresnel reflection peak across Callisto's entire surface, and 2) a new map of spectral features at 4.25 μm (CO_2) and 4.57 μm on a Valhalla-centered viewing geometry. For CO_2, we map both the solid-phase distribution as well as the gaseous-phase column densities. With these data products in hand, we arrive at the following key takeaways:

— We find that the strength of Callisto's 3.1 μm Fresnel peak tracks primarily with geology (i.e., large impacts) on the leading hemisphere. Valhalla, Asgard, and Lofn/Heimdall are all terrains with increased Fresnel band areas. This finding is

consistent with their high albedoes and previously measured H_2O ice content from the NIMS instrument onboard Galileo (Moore et al., 2004; Hibbitts et al., 2000). On the trailing hemisphere, the Fresnel peak exhibits an "inverted bullseye" pattern, with the band areas being weaker toward the lower lattitudes.

— The greatest abundance of CO_2 on Callisto's leading hemisphere is co-located with the Lofn/Heimdall impact suite. The shape and band center of the CO_2 spectral feature in this region is comparable to that in the Valhalla impact basin, suggesting the two impacts host their CO_2 in similar (icy) material. Lofn/Heimdall may host the largest share of non-radiolytic CO_2 on Callisto. It is possible that CO_2 in the Lofn/Heimdall region has remained enriched relative to the rest of the leading hemisphere given its location at high latitudes, where mechanisms that would otherwise release volatiles from the surface—such as solar insolation and sputtering—are weakened. Alternatively, the thermal properties of the region as inferred from ALMA observations (Camarca et al. 2023, Camarca submitted) may favor the retention of CO_2 in this area. Fortunately, Lofn and Heimdall have been identified as "Regions of Interest" on Callisto for JUICE, and the JANUS camera will image this region at ∼3-4 km per pixel, and the imaging infrared spectrometer MAJIS will acquire 30 m/pixel resolution (Stephan et al., 2021a).

— On the trailing hemisphere, we identify that the band depth of the solid-phase CO_2 is anti-correlated with the strength of the Fresnel peak band area. The regions of highest CO_2 absorption at the low latitudes centered on the trailing hemisphere are the regions of lowest Fresnel peak strength, and both molecules exhibit a characteristic "bullseye" pattern. This anti-correlation could be explained if the radiolytic processes on Callisto's trailing hemisphere regolith are depleting the region of its exposed H_2O ice, an ingredient in the generation of CO_2. Alternatively, H_2O ice could be removed from low-latitude regions by sublimation promoted by the highly volatile nature of CO_2, or perhaps by sputtering via charged particles that preferentially interact with the trailing hemisphere.

— We detect a patchy CO_2 atmosphere with peak column densities $\sim 1.4 \times 10^{19}\ m^{-2}$ on the Valhalla-centered observation. We find that the peak column densities of the gaseous CO_2 are offset from the region of strongest solid-phase CO_2 absorption. A similar offset was noted for Callisto's trailing hemisphere (Cartwright et al., 2024). Future modeling efforts as well as telescopic observations are needed to understand the mechanisms driving CO_2 release from the surfaces of icy moons like Callisto.

— We find the the band depth of the 4.57 μm is stronger on Callisto's leading hemi-

sphere, including with the new Valhalla-centered observation, than on the trailing hemisphere. The material responsible for the 4.57 μm appears somewhat depleted in the center of the Valhalla impact basin. These findings, in combination with those put forward by Cartwright et al. (2024) and Sharkey et al. (2025), may suggest the exogenic delivery of dust from Jovian irregular satellites is a relevant processes for partially explaining the distribution of the 4.57 μm feature.

Acknowledgments

This research is based on observations made with the NASA/ESA James Webb Space Telescope obtained from the Space Telescope Science Institute, which is operated by the Association of Universities for Research in Astronomy, Inc., under NASA contract NAS 5–26555. These observations are associated with program 2060 (JWST-GO-02060.001-A). M.C. acknowledges support from the National Science Foundation through a Graduate Research Fellowship, grant No. DGE-1745301. K.d.K. and M.C. acknowledge support from the National Science Foundation through grant No. 2308280.

M.C. thanks Ryleigh Davis for some very helpful conversations about Callisto, and Zac Milby for help with lmfit and much encouragement.

BIBLIOGRAPHY

Bockelée-Morvan, D. et al. (2024a). "Composition and thermal properties of Ganymede's surface from JWST/NIRSpec and MIRI observations". *Astronomy & Astrophysics* Vol. 681. DOI: 10.1051/0004-6361/202347326.

Bockelée-Morvan, D. et al. (2024b). "A patchy CO2 exosphere on Ganymede revealed by the James Webb Space Telescope". *Astronomy & Astrophysics* Vol. 690. DOI: 10.1051/0004-6361/202451599.

Bottke, W. F. et al. (2013). "Black rain: The burial of the Galilean satellites in irregular satellite debris". *Icarus* Vol. 223, No. 2. DOI: 10.1016/j.icarus.2013.01.008.

Camarca, M. et al. (2023). "Thermal Properties of the Leading Hemisphere of Callisto Inferred from ALMA Observations". *The Planetary Science Journal* Vol. 4, No. 8. DOI: 10.3847/PSJ/aceb68.

Carlson, R. et al. (1996). "Near-Infrared Spectroscopy and Spectral Mapping of Jupiter and the Galilean Satellites: Results from Galileo's Initial Orbit". *Science* Vol. 274, No. 5286. DOI: 10.1126/science.274.5286.385.

Carlson, R. W. et al. (1992). "Near-Infrared Mapping Spectrometer experiment on Galileo". *Space Science Reviews* Vol. 60, No. 1. DOI: 10.1007/BF00216865.

Cartwright, R. J. et al. (2020). "Evidence for Sulfur-bearing Species on Callisto's Leading Hemisphere: Sourced from Jupiter's Irregular Satellites or Io?" *The Astrophysical Journal* Vol. 902, No. 2. DOI: 10.3847/2041-8213/abbdae.

Cartwright, R. J. et al. (2024). "Revealing Callisto's Carbon-rich Surface and CO_2 Atmosphere with JWST". *The Planetary Science Journal* Vol. 5, No. 3. DOI: 10.3847/PSJ/ad23e6.

Cartwright, R. J. et al. (2025). *JWST Reveals Spectral Tracers of Recent Surface Modification on Europa*. DOI: 10.48550/arXiv.2504.05283.

Cassidy, T. et al. (2010). "Radiolysis and Photolysis of Icy Satellite Surfaces: Experiments and Theory". *Space Science Reviews* Vol. 153, No. 1. DOI: 10.1007/s11214-009-9625-3.

Chen, Z. et al. (2024). "'Life' of dust originating from the irregular satellites of Jupiter". *Monthly Notices of the Royal Astronomical Society* Vol. 527, No. 4. DOI: 10.1093/mnras/stad3829.

Clark, R. N. et al. (1980). "The Galilean Satellites: New Near-Infrared Spectral Reflectance Measurements (0.65-2.5 microns) and a 0.325-5 micron Summary". Vol. 41.

Cochrane, C. J. et al. (2025). "Stronger Evidence of a Subsurface Ocean Within Callisto From a Multifrequency Investigation of Its Induced Magnetic Field". *AGU Advances* Vol. 6, No. 1. DOI: 10.1029/2024AV001237.

Cooper, J. F. et al. (2001). "Energetic Ion and Electron Irradiation of the Icy Galilean Satellites". *Icarus* Vol. 149, No. 1. DOI: 10.1006/icar.2000.6498.

Coradini, A. et al. (2008). "Identification of spectral units on Phoebe". *Icarus* Vol. 193, No. 1. DOI: 10.1016/j.icarus.2007.07.023.

Cunningham, N. J. et al. (2015). "Detection of Callisto's oxygen atmosphere with the Hubble Space Telescope". *Icarus* Vol. 254. DOI: 10.1016/j.icarus.2015.03.021.

Davies, A. G. et al. (2006). "The heartbeat of the volcano: The discovery of episodic activity at Prometheus on Io". *Icarus* Vol. 184, No. 2. DOI: 10.1016/j.icarus.2006.05.012.

de Kleer, K. et al. (2019). *Tidal Heating: Lessons from Io and the Jovian System - Final Report*. DOI: 10.26206/d4wc-6v82.

de Kleer, K. et al. (2021). "Ganymede's Surface Properties from Millimeter and Infrared Thermal Emission". *The Planetary Science Journal* Vol. 2, No. 1. DOI: 10.3847/PSJ/abcbf4.

de Kleer, K. et al. (2023). "The Optical Aurorae of Europa, Ganymede, and Callisto". *The Planetary Science Journal* Vol. 4. DOI: 10.3847/PSJ/acb53c.

de Kleer, K. et al. (2024). "Isotopic evidence of long-lived volcanism on Io". *Science* Vol. 384, No. 6696. DOI: 10.1126/science.adj0625.

de Pater, I. et al. (2023). "An Energetic Eruption With Associated SO 1.707 Micron Emissions at Io's Kanehekili Fluctus and a Brightening Event at Loki Patera Observed by JWST". *Journal of Geophysical Research: Planets* Vol. 128, No. 8. DOI: 10.1029/2023JE007872.

Ehrenfreund, P. et al. (1996). "Infrared properties of isolated water ice." *Astronomy and Astrophysics* Vol. 312.

Gardner, J. P. et al. (2023). "The James Webb Space Telescope Mission". *Publications of the Astronomical Society of the Pacific* Vol. 135, No. 1048. DOI: 10.1088/1538-3873/acd1b5.

Greeley, R. et al. (2000). "Galileo views of the geology of Callisto". *Planetary and Space Science* Vol. 48, No. 9. DOI: 10.1016/S0032-0633(00)00050-7.

Greeley, R. et al. (2001). "Geology of Lofn Crater, Callisto". *Journal of Geophysical Research: Planets* Vol. 106 (E2). DOI: 10.1029/2000JE001262.

Grim, R. J. A. et al. (1987). "Ions in grain mantles - The 4.62 micron absorption by OCN(-) in W33A". *The Astrophysical Journal* Vol. 321. DOI: 10.1086/185012.

Hansen, G. B. et al. (2004). “Amorphous and crystalline ice on the Galilean satellites: A balance between thermal and radiolytic processes”. *Journal of Geophysical Research: Planets* Vol. 109 (E1). DOI: 10.1029/2003JE002149.

Hase, F. et al. (2010). “The ACE-FTS atlas of the infrared solar spectrum”. *Journal of Quantitative Spectroscopy and Radiative Transfer* Vol. 111, No. 4. DOI: 10.1016/j.jqsrt.2009.10.020.

Hibbitts, C. A. et al. (2000). “Distributions of CO_2 and SO_2 on the surface of Callisto”. *Journal of Geophysical Research: Planets* Vol. 105 (E9). DOI: 10.1029/1999JE001101.

Hibbitts, C. A. et al. (2002). “CO2-rich impact craters on Callisto”. *Journal of Geophysical Research: Planets* Vol. 107 (E10). DOI: 10.1029/2000JE001412.

Jakobsen, P. et al. (2022). “The Near-Infrared Spectrograph (NIRSpec) on the James Webb Space Telescope - I. Overview of the instrument and its capabilities”. *Astronomy & Astrophysics* Vol. 661. DOI: 10.1051/0004-6361/202142663.

Jenniskens, P. et al. (1996). “Crystallization of Amorphous Water Ice in the Solar System”. *The Astrophysical Journal* Vol. 473, No. 2. DOI: 10.1086/178220.

Johnson, R. E. et al. (1997a). “O2/O3 Microatmospheres in the Surface of Ganymede”. *The Astrophysical Journal* Vol. 480, No. 1. DOI: 10.1086/310614.

Johnson, R. E. et al. (1997b). “Photolysis and radiolysis of water ice on outer solar system bodies”. *Journal of Geophysical Research: Planets* Vol. 102 (E5). DOI: 10.1029/97JE00068.

Johnson, R. E. (1990). *Energetic Charged-Particle Interactions with Atmospheres and Surfaces*. Berlin, Heidelberg: Springer Berlin Heidelberg. DOI: 10.1007/978-3-642-48375-2.

Kurucz, R. L. (2005). “New atlases for solar flux, irradiance, central intensity, and limb intensity”. *Memorie della Societa Astronomica Italiana Supplementi* Vol. 8.

Mastrapa, R. M. et al. (2009). “OPTICAL CONSTANTS OF AMORPHOUS AND CRYSTALLINE H2O-ICE: 2.5–22 μm (4000–455 cm–1) OPTICAL CONSTANTS OF H2O-ICE”. *The Astrophysical Journal* Vol. 701, No. 2. DOI: 10.1088/0004-637X/701/2/1347.

McClure, M. K. et al. (2023). “An Ice Age JWST inventory of dense molecular cloud ices”. *Nature Astronomy* Vol. 7, No. 4. DOI: 10.1038/s41550-022-01875-w.

McCord, T. B. et al. (1997). “Organics and Other Molecules in the Surfaces of Callisto and Ganymede”. *Science* Vol. 278, No. 5336. DOI: 10.1126/science.278.5336.271.

McCord, T. B. et al. (1998). “Non-water-ice constituents in the surface material of the icy Galilean satellites from the Galileo near-infrared mapping spectrometer investigation”. *Journal of Geophysical Research: Planets* Vol. 103 (E4). DOI: 10.1029/98JE00788.

McCord, T. B. et al. (1999). “Hydrated salt minerals on Europa’s surface from the Galileo near-infrared mapping spectrometer (NIMS) investigation”. *Journal of Geophysical Research: Planets* Vol. 104 (E5). DOI: 10.1029/1999JE900005.

Mennella, V. et al. (2004). “Formation of CO and CO2 Molecules by Ion Irradiation of Water Ice-covered Hydrogenated Carbon Grains”. *The Astrophysical Journal* Vol. 615, No. 2. DOI: 10.1086/424685.

Mitchell, E. H. et al. (2017). “Porosity effects on crystallization kinetics of amorphous solid water: Implications for cold icy objects in the outer solar system”. *Icarus* Vol. 285. DOI: 10.1016/j.icarus.2016.11.004.

Moore, J. et al. (2004). “Callisto”. *Jupiter: The Planet, Satellites and Magnetosphere*. Cambridge: Cambridge University Press.

Moore, J. M. et al. (1999). “Mass Movement and Landform Degradation on the Icy Galilean Satellites: Results of the Galileo Nominal Mission”. *Icarus* Vol. 140, No. 2. DOI: 10.1006/icar.1999.6132.

Morabito, L. A. et al. (1979). “Discovery of Currently Active Extraterrestrial Volcanism”. *Science* Vol. 204, No. 4396. DOI: 10.1126/science.204.4396.972.

Morrison, D. et al. (1972). “Temperatures of Titan and the Galilean Satellites at 20 Microns”. *The Astrophysical Journal* Vol. 173. DOI: 10.1086/180934.

Newville, M. et al. (2025). *LMFIT: Non-Linear Least-Squares Minimization and Curve-Fitting for Python*. Version 1.3.3. DOI: 10.5281/zenodo.15014437.

Oza, A. V. et al. (2024). “Common origin of trapped volatiles in oxidized icy moons and comets”. *Icarus* Vol. 411. DOI: 10.1016/j.icarus.2024.115944.

Pappalardo, R. et al. (2004). “Ganymede”. *Jupiter: The Planet, Satellites and Magnetosphere*. Ed. by F. Bagenal et al. Cambridge University Press.

Pollack, J. B. et al. (1978). “Near-infrared spectra of the Galilean satellites: Observations and compositional implications”. *Icarus* Vol. 36, No. 3. DOI: 10.1016/0019-1035(78)90110-0.

Raut, U. et al. (2012). “Radiation synthesis of carbon dioxide in ice-coated carbon: Implications for interstellar grains and icy moons”. *The Astrophysical Journal* Vol. 752, No. 2. DOI: 10.1088/0004-637X/752/2/159.

Roth, L. (2021). “A Stable H2O Atmosphere on Europa’s Trailing Hemisphere From HST Images”. *Geophysical Research Letters* Vol. 48, No. 20. DOI: 10.1029/2021GL094289.

Roush, T. L. et al. (1990). “Ice and minerals on Callisto: A reassessment of the reflectance spectra”. *Icarus* Vol. 86. DOI: 10.1016/0019-1035(90)90225-X.

Schmidt, B. E. et al. (2011). “Active formation of ’chaos terrain’ over shallow subsurface water on Europa”. *Nature* Vol. 479, No. 7374. DOI: 10.1038/nature10608.

Sharkey, B. N. L. et al. (2025). *JWST Reveals Varied Origins Between Jupiter's Irregular Satellites*. DOI: 10.48550/arXiv.2501.16484.

Soifer, B. T. et al. (1979). "The 4 - 8 micron spectrum of the infrared source W33 A." *The Astrophysical Journal* Vol. 232. DOI: 10.1086/183035.

Spencer, J. R. (1987). "Thermal segregation of water ice on the Galilean satellites". *Icarus* Vol. 69, No. 2. DOI: 10.1016/0019-1035(87)90107-2.

Spencer, J. R. et al. (2002). "Condensed O2 on Europa and Callisto". *The Astronomical Journal* Vol. 124, No. 6. DOI: 10.1086/344307.

Spencer, J. R. et al. (2010). "Formation of Iapetus' Extreme Albedo Dichotomy by Exogenically Triggered Thermal Ice Migration". *Science* Vol. 327. DOI: 10.1126/science.1177132.

Stephan, K. et al. (2021a). "Regions of interest on Ganymede's and Callisto's surfaces as potential targets for ESA's JUICE mission". *Planetary and Space Science* Vol. 208. DOI: 10.1016/j.pss.2021.105324.

Stephan, K. et al. (2020). "H2O-ice particle size variations across Ganymede's and Callisto's surface". *Icarus* Vol. 337. DOI: 10.1016/j.icarus.2019.113440.

Stephan, K. et al. (2021b). "VIS-NIR/SWIR Spectral Properties of H2O Ice Depending on Particle Size and Surface Temperature". *Minerals* Vol. 11, No. 12. DOI: 10.3390/min11121328.

Trumbo, S. K. et al. (2021). "The Geographic Distribution of Dense-phase O2 on Ganymede". *The Planetary Science Journal* Vol. 2, No. 4. DOI: 10.3847/PSJ/ac0cee.

Trumbo, S. K. et al. (2023a). "Hydrogen peroxide at the poles of Ganymede". *Science Advances* Vol. 9, No. 29. DOI: 10.1126/sciadv.adg3724.

Trumbo, S. K. et al. (2023b). "The distribution of CO $_2$ on Europa indicates an internal source of carbon". *Science* Vol. 381, No. 6664. DOI: 10.1126/science.adg4155.

Van Broekhuizen, F. A. et al. (2005). "A 3–5 $\mathsf{\mu}$m VLT spectroscopic survey of embedded young low mass stars II: Solid OCN$\mathsf{^{-}}$". *Astronomy & Astrophysics* Vol. 441, No. 1. DOI: 10.1051/0004-6361:20041711.

Villanueva, G. L. et al. (2018). "Planetary Spectrum Generator: An accurate online radiative transfer suite for atmospheres, comets, small bodies and exoplanets". *Journal of Quantitative Spectroscopy and Radiative Transfer* Vol. 217. DOI: 10.1016/j.jqsrt.2018.05.023.

Villanueva, G. L. et al. (2023a). "Endogenous CO $_2$ ice mixture on the surface of Europa and no detection of plume activity". *Science* Vol. 381, No. 6664. DOI: 10.1126/science.adg4270.

Villanueva, G. L. et al. (2023b). “JWST molecular mapping and characterization of Enceladus’ water plume feeding its torus”. *Nature Astronomy* Vol. 7, No. 9. DOI: 10.1038/s41550-023-02009-6.

Villanueva, G. L. et al. (2022). *Fundamentals of the Planetary Spectrum Generator*.

Vorburger, A. et al. (2019). “Three-Dimensional Modeling of Callisto’s Surface Sputtered Exosphere Environment”. *Journal of Geophysical Research: Space Physics* Vol. 124, No. 8. DOI: 10.1029/2019JA026610.

Wagner, R. et al. (1998). “Time-Stratigraphy and Crater Retention Ages of Geologic Units on Callisto”. Lunar and Planetary Science Conference.

Wagner, R. et al. (1999). “Ages of Individual Craters on the Galilean Satellites Ganymede and Callisto”. Lunar and Planetary Science Conference.

Zimmer, C. (2000). “Subsurface Oceans on Europa and Callisto: Constraints from Galileo Magnetometer Observations”. *Icarus* Vol. 147, No. 2. DOI: 10.1006/icar.2000.6456.

Chapter 5

THE GALILEAN SATELLITES AND ALMA: A SHORT GUIDED TOUR

5.1 Introduction

Within a postage stamp of sky ∼1 arcsecond across, the Atacama Large Millimeter/submillimeter Array (ALMA) can capture a portrait of a whole solar system. The remarkable sensitivity and milliarcsecond resolution of ALMA reveals the grandeur of protoplanetary disks—complex rings, gaps, and even embedded planets in their infancy (Huang et al., 2018; Benisty et al., 2021). Using a similarly sized frame on the sky, ALMA can also acquire portraits of astronomy's most famous mini-solar system: the Galilean moons.

At present, ALMA has mapped the continuum emission between ∼97-343 GHz from the surfaces of Jupiter's three large icy moons: Europa (Trumbo et al., 2017; Trumbo et al., 2018; Thelen et al., 2024), Ganymede (de Kleer et al., 2021), and Callisto (Camarca et al. 2023, Camarca in review). These observations have yielded two primary science products: estimates of the subsurface material properties and spatially resolved maps of thermal anomalies. This article offers a summary of these findings at a particularly timely moment—ESA's JUICE mission and NASA's Europa Clipper are enroute to the Jovian satellite system, and data is actively flowing to the community from major observatories like JWST (Gardner et al., 2023). A guided tour through ALMA's observations of the Galilean moons will assist planetary astronomers in integrating these results into their research by highlighting the key geologic patterns revealed through (sub)millimeter continuum data.

The flow of the tour is as follows: in Section 5.2, we outline the basic operating principle of ALMA. In Section 5.3, we outline how ALMA continuum observations are turned into a measure of material properties and maps of thermal anomalies. In Section 5.4, we summarize the main findings ALMA has made for the icy Galileans. Next, in Section 5.5, we compare the science outcomes of the Galilean moon continuum survey to early ALMA science case documents to highlight this work fulfills decades-old science promises for the array. Afterwards, in Section 5.6, we comment on future avenues for ALMA satellite research. Lastly, in Section 5.7, we summarize our discussion.

5.2 How ALMA works

As a radio interferometer, ALMA operates in a fundamentally different way than most optical and infrared astronomical facilities. To illustrate, consider the diffraction equation:

$$\theta \approx \frac{\lambda}{D} 206265$$

which relates the resolution θ in arcseconds of an observation at wavelength λ in m to the diameter of the telescope D in m. For a proposed observation at 1 millimeter of a $\sim$1 arcsecond Galilean moon, resolving major geologic units on the moon using six resolution elements across the disk requires $\sim 0.17''$ resolution. To meet this resolution, D must be $>$1 km; a single dish of this size is unfeasible to build. What *is* feasible to build is an array of many single dishes spaced across a large distance that are linked using fiber optic cables and a powerful correlator to operate as a large virtual telescope. This is the principle underlying radio interferometry. The ALMA interferometric array comprises 66 individual antennas, each of which is 12 m in diameter. In the radio astronomy literature, the phrase "synthesized beam" or sometimes just the word "beam" refer to the resolution element of the entire array. Although the SubMillimeter Array (SMA) is also capable of achieving subarcsecond resolution in the millimeter, only ALMA can do so in integrations short enough for Galilean moon science.

The incredible sensitivity of ALMA is evident when compared to the mm/submm observation record of the Galilean moons. Nearly all past observations required hours-long integration times just to collect one disk-averaged brightness temperature (e.g., Muhleman et al. 1991). By contrast, the resolved ALMA observations were acquired in $\sim$ 2 min time. Lowering the observing time is not just a matter of efficiency, it necessary to prevent the smearing of geologic features over long integration times (e.g., Europa's subobserver longitude would change by $\sim$25 deg in a 6 hour integration). As such, ALMA distinguishes itself as the only telescope capable of achieving the spatial resolution and sensitivity required for material property science on the Galilean moons.

In the next section, we describe the key steps that take one from Galilean moon observation to thermophysical properties and emission maps.

5.3 From warm disk to thermal properties

The published ALMA icy moon observations include images of their leading and trailing hemispheres (Fig. 5.1) at Bands 3 (97 GHz/3 mm), 6 (233 GHz/1 mm),

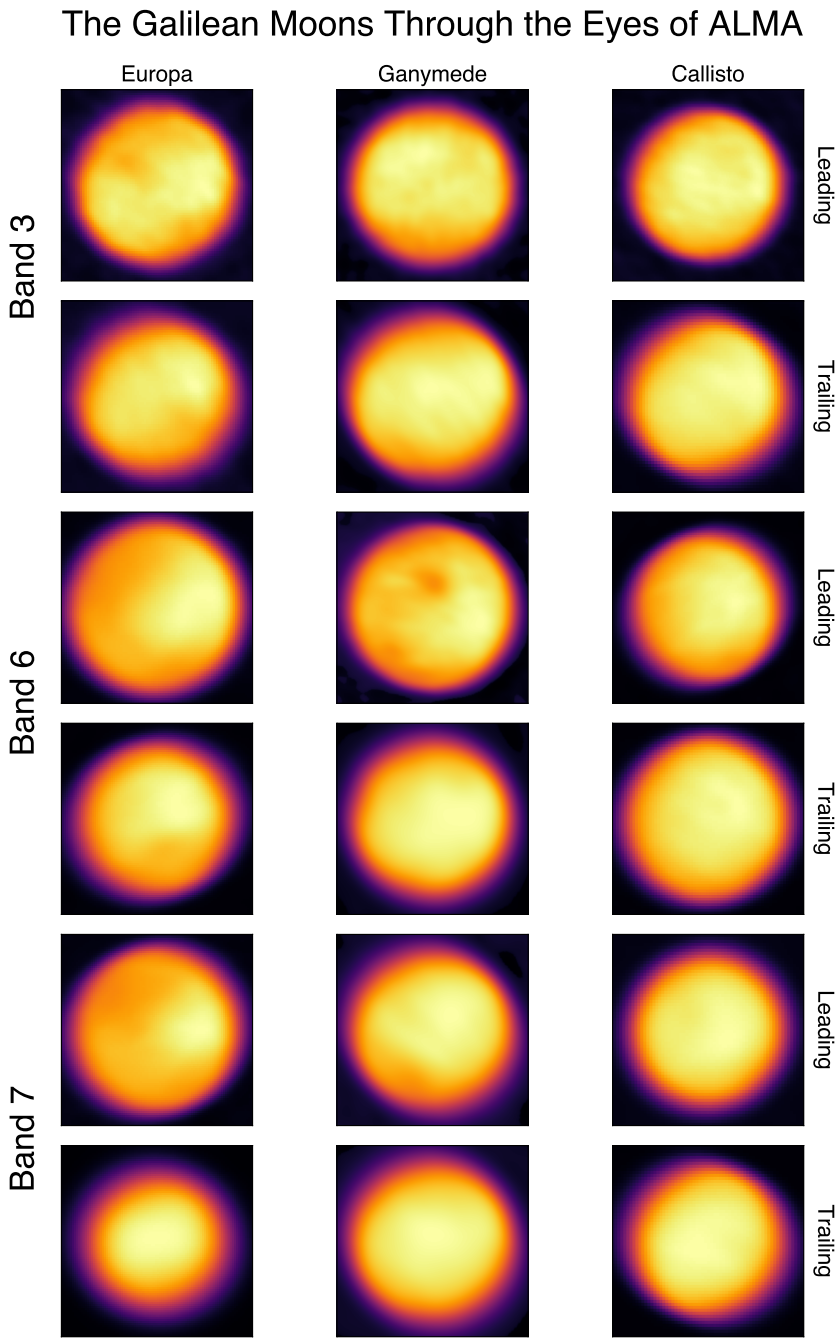

Figure 5.1: The thermal emission of Jupiter's three large icy satellites as observed by ALMA. The leading and trailing hemispheres of each satellite have been observed at Bands 3 (97 GHz/3 mm), 6 (233 GHz/1 mm), and 7 (343 GHz/0.87 mm). Images are not shown on a common color scale to highlight differences across the disk for an individual moon. Data taken from: Thelen et al. 2024; de Kleer et al. 2021; Camarca et al. 2023, and Chapter 3 of this work.

and 7 (343 GHz/0.87 mm). For a porous, icy surface, Band 7 observations sound thermal emission from $\sim\frac{1}{2}$ cm depths, while the Band 3 frequency may sense $\sim\frac{1}{2}$ meter depths. These are deeper than the shallower (∼mm) depths probed by infrared wavelengths, and therefore allow us to inspect the materials further below the diurnal wave. As such, proper thermal modeling of Galilean moon millimeter/submillimeter data incorporates radiative transfer and the integration of emission from the subsurface layers.

Using just a few tunable parameters such as thermal inertia and emissivity, a warm satellite disk observed by ALMA can be surprisingly well-modeled. Thermal inertia is parameterized as $\Gamma = \sqrt{k\rho c}$, where k is the thermal conductivity, ρ is the density, and c is the heat capacity. The higher the value of Γ, the more resistant a material is to changing its temperature. For a planetary surface, Γ offers a clue toward the presence of loosely compacted (low Γ) or more tightly compacted, denser materials (high Γ). Additionally, emissivity ϵ is a unitless quantity that ranges from 0 to 1 that defines how well a surface radiates its heat compared to a blackbody of the same temperature. In this work, we refer to spectral emissivities measured at the sub/millimeter frequencies. Together, these quantities can serve as signposts pointing toward unique (or expected) geologic terrains on an icy moon.

Here, it is important to highlight that a strategic workaround is oft employed in the ALMA icy satellite literature in response to data limitations. The gold standard of material property measurements would be a map where every location on the disk is assigned a unique Γ and ϵ. Such a map can be constructed with high-fidelity if the daily temperature cycle of each location is well-sampled. However, a single spatially-resolved ALMA image is only a "snapshot" of the satellite's emission. In this snapshot, the temperature is retrieved for many locations across the disk, but only for a single local time at each location. However, the local time of each location is different. Therefore, under the assumption that the material properties are uniform across the disk, spatial differences may be treated as time of day samples to inform a global model. These globally-derived properties are then reported for different frequencies and different hemispheres, and the subsequent subtraction of the global model from corresponding data reveals which locations diverge most from the global estimate.

5.4 What have we learned with ALMA?

In this section, we identify the most salient features of the thermal modeling outcomes for Europa, Ganymede, and Callisto, and propose a coherent narrative that weaves the thermal properties of these moons together.

Emissivity and thermal inertia:

Consistent with the established microwave paradigm (e.g.,Muhleman et al. 1991), the ALMA-derived emissivities for the icy moons point toward increased ice exposure lowering the emissivity. All three icy satellites have ALMA emissivities typically greater >0.75. For Europa and Ganymede, the range of measured emissivities are lower than those measured for Callisto. A probable cause for this difference is that Callisto retains a very large dark blanket of material (possibly 10s of meters thick, Basilevsky et al. 2002; Moore et al. 2004) and very little ice exposure (<10 percent areal coverage), while Ganymede and Europa have progressively more fresh ice on their surfaces. The Saturnian system provides a strong example of the link between high emissivity/dark material and low emissivity/clean ice. Iapetus, with its dark, dust-covered leading hemisphere from Phoebe and its icy trailing side (Denk et al., 2010), shows this clearly: Cassini observations modeled higher emissivity on the dark side (∼0.88) than on the icy side (∼0.68) (Le Gall et al., 2014; Bonnefoy et al., 2024). This pattern is repeated across the system as a whole, where satellite emissivities at 2.2 cm increase with distance from Saturn. Though, the relationship between dark material and emissivity is not always straightforward. For example, warm residuals (more suggestive of dark material) are not as well correlated in the millimeter with Ganymede's dark terrain compared to IR data, despite the expectation the dark material is a few mm thick on Ganymede (de Kleer et al., 2021). Additionally, there appears to be an increase in thermal inertia with distance from Jupiter. To distill the Γ values into a sentence, the values are roughly $\Gamma \sim$ low 100s for Europa, $\Gamma \sim$ mid-high 100s for Ganymede, $\Gamma \sim$ high 100s and >1000 for Callisto. This thermal inertia difference can also be inspected by eye, as shown in Fig. 5.1, Callisto mostly looks like a uniform, warm ball while the other icy satellites bear more pronounced limb-to-limb gradients.

Temperature Maps: Beyond just lists of Γ and ϵ are the exciting temperature residuals that arise from the subtraction of a synthetic satellite from the actual data. Such maps are interesting when tethered to geologic maps, as they sometimes reveal new regions of interest. Here, we highlight the motifs in ALMA data between the three moons.

Impacts: Cold thermal anomalies are associated with large craters on all three Galilean moons. These include Pwyll on Europa, Tros and Osiris on Ganymede, and Valhalla and Lofn (and/or Heimdall and Adlinda) on Callisto. These craters are usually >3 K (sometimes up to 10 K) colder than surrounding terrain in the thermal model residuals. This behavior is consistent over an impressive range of ∼ two orders of magnitude in age (∼10s of millions to billions years old) and two orders of magnitude in diameter (10s km to 1000s of km). The origin of this is likely because craters may excavate denser (icier) subsurface materials that are higher thermal inertia than their surroundings. In this case, the lower emissivity of water ice is also a probable contributing factor. At the micrometeorite scale, the ALMA data do appear to encode some evidence for surface texture alteration. On Ganymede and Callisto, some regions of low-latitude warm regions on the leading hemisphere are suggestive of the possible presence of preferential micrometeorite bombardment in those areas.

Endogenic heating? Anecdotally, it is sometimes asked whether or not there is evidence for endogenic heating in ALMA data. At present, there are no claimed detections of endogenic hotspots in ALMA literature. If anything, one of the early icy moon results was that ALMA observations at 233 GHz demonstrated that a purported endogenic hotspot on Europa could be satisfactorily modeled as an area with high-thermal inertia material (Trumbo et al., 2017)..

5.5 Fulfilled Promises

With its initial survey of the continuum emission profiles of the icy Galilean satellites now complete, ALMA has successfully delivered on a science goal articulated during its development phase. The task of observing the Galilean moons with a giant interferometer actually predates ALMA. Before the formation of the international ALMA collaboration, a predecessor project from NRAO—the Millimeter Array (MMA)— had already bookmarked the Galilean satellites for its solar system science objectives (Vanden Bout et al., 2023; F Schloerb et al., 1995; F Schloerb et al., 1998). The MMA documents also highlighted other topics that now define ALMA's current planetary science portfolio, such as investigations of cometary atmospheres (Cordiner et al., 2019; Cordiner et al., 2020; Roth et al., 2021) and Titan's organic-rich atmosphere (Nixon et al., 2020; Thelen et al., 2022; Palmer et al., 2017). After the MMA was incorporated into ALMA, the thermal characterization of the Galilean moons remained a core solar system objective (Butler et al., 2001). In these early science cases, the teams envisioned that millimeter observations of the Galilean satellites would provide unprecedented access to their thermal properties

and by extension, their unique surface processes. Three decades later, this vision has now been realized.

5.6 Looking Forward

Is CO_2 gas on the move? JWST has revealed both Ganymede (Bockelée-Morvan et al., 2024) and Callisto (Cartwright et al. 2024, Chapter 4 of this work) bear patchy CO_2 atmospheres. The location of the peak CO_2 column densities is not tied to the areas of peak solid-phase CO_2 on the surface, which is expected to source the atmosphere. One can speculate about what underlying geologic units might be the cause of this (impact exposed crustal CO_2?), but only if the CO_2 gas clusters are stationary. Modelers might be able to use the ALMA brightness temperature maps to inform models of CO_2 gas migration.

To what extent are the patterns in satellite thermal properties broadly applicable? The parallel gradients in surface properties with orbital distance observed in both Jovian and Saturnian moon systems may echo their shared formation setting (i.e., a circumplanetary disk; Lunine et al., 1982; Batygin et al., 2020; Canup et al., 2002). By contrast, the library of origin stories for the Neptunian and Uranian satellites is far more broad as it features giant impact scenarios and captured satellites (Agnor et al., 2006; Morbidelli et al., 2012; Krapp et al., 2024; Ida et al., 2020). Currently, the only published ALMA result for either system is an observation of Triton (Gurwell et al., 2019). When the full set of moons is finally observed in the radio for the first time, will the survey reveal a whole new template of surface properties? Whatever the findings may be, the ALMA Galilean moon survey can anchor the Uranian and Neptunian satellites to the rest of the solar system.

5.7 Conclusion

ALMA is a powerful astronomical facility made famous by its remarkable pictures of distant early-stage solar systems. Closer to home, it offers an incredible platform for geology-oriented inquiry on Jupiter's three icy moons, Europa, Ganymede, and Callisto via continuum observations of their surfaces. At the satellite system scale, ALMA observations further confirm a gradient in thermal properties with distance from Jupiter. At the local scale, the satellites share some thermal anomalies with common geologic origins, as well as some which highlight the unique processes active on each moon. In a few years, this ALMA dataset will provide an excellent ground-based complement to ESA's JUICE Submillimetre Wave Instrument (SWI), as well as the E-THEMIS instrument onboard Europa Clipper. Perhaps in a few years

there will enough ALMA data to support follow-up article entitled "The Planetary Satellites and ALMA: A Long Guided Tour".

BIBLIOGRAPHY

Agnor, C. B. et al. (2006). "Neptune's capture of its moon Triton in a binary–planet gravitational encounter". *Nature* Vol. 441, No. 7090. DOI: 10.1038/nature04792.

Basilevsky, A. T. et al. (2002). "The Morphology of Small Craters and Knobs on the Surface of Jupiter's Satellite Callisto". *Solar System Research* Vol. 36, No. 4. DOI: 10.1023/A:1019576422376.

Batygin, K. et al. (2020). "Formation of Giant Planet Satellites". *The Astrophysical Journal* Vol. 894, No. 2. DOI: 10.3847/1538-4357/ab8937.

Benisty, M. et al. (2021). "A Circumplanetary Disk around PDS70c". *The Astrophysical Journal* Vol. 916, No. 1. DOI: 10.3847/2041-8213/ac0f83.

Bockelée-Morvan, D. et al. (2024). "A patchy CO2 exosphere on Ganymede revealed by the James Webb Space Telescope". *Astronomy & Astrophysics* Vol. 690. DOI: 10.1051/0004-6361/202451599.

Bonnefoy, L. E. et al. (2024). "Microwave spectra of the leading and trailing hemispheres of Iapetus". *Icarus* Vol. 411. DOI: 10.1016/j.icarus.2024.115950.

Butler, B. J. et al. (2001). "Solar System Science with ALMA". *Science with the Atacama Large Millimeter Array, ASP Conference Proceeding Vol. 235. Edited by Alwyn Wootten. San Francisco: Astronomical Society of the Pacific. ISBN: 1-58381-072-2, 2001., p.225-228* Vol. 235.

Camarca, M. et al. (2023). "Thermal Properties of the Leading Hemisphere of Callisto Inferred from ALMA Observations". *The Planetary Science Journal* Vol. 4, No. 8. DOI: 10.3847/PSJ/aceb68.

Canup, R. M. et al. (2002). "Formation of the Galilean Satellites: Conditions of Accretion". *The Astronomical Journal* Vol. 124, No. 6. DOI: 10.1086/344684.

Cartwright, R. J. et al. (2024). "Revealing Callisto's Carbon-rich Surface and CO_2 Atmosphere with JWST". *The Planetary Science Journal* Vol. 5, No. 3. DOI: 10.3847/PSJ/ad23e6.

Cordiner, M. A. et al. (2019). "ALMA Autocorrelation Spectroscopy of Comets: The HCN/H13CN Ratio in C/2012 S1 (ISON)". *The Astrophysical Journal* Vol. 870. DOI: 10.3847/2041-8213/aafb05.

Cordiner, M. A. et al. (2020). "Unusually high CO abundance of the first active interstellar comet". *Nature Astronomy* Vol. 4. DOI: 10.1038/s41550-020-1087-2.

de Kleer, K. et al. (2021). "Ganymede's Surface Properties from Millimeter and Infrared Thermal Emission". *The Planetary Science Journal* Vol. 2, No. 1. DOI: 10.3847/PSJ/abcbf4.

Denk, T. et al. (2010). “Iapetus: Unique Surface Properties and a Global Color Dichotomy from Cassini Imaging”. *Science* Vol. 327. DOI: 10.1126/science.1177088.

F Schloerb et al. (1995). *Report of Solar System Working Group*.

F Schloerb et al. (1998). *UPDATE OF MMA SOLAR SYSTEM WORKING GROUP REPORT*.

Gardner, J. P. et al. (2023). “The James Webb Space Telescope Mission”. *Publications of the Astronomical Society of the Pacific* Vol. 135, No. 1048. DOI: 10.1088/1538-3873/acd1b5.

Gurwell, M. et al. (2019). “The Atmosphere of Triton Observed With ALMA”. EPSC-DPS Joint Meeting 2019. Vol. 2019.

Huang, J. et al. (2018). “The Disk Substructures at High Angular Resolution Project (DSHARP). II. Characteristics of Annular Substructures”. *The Astrophysical Journal Letters* Vol. 869, No. 2. DOI: 10.3847/2041-8213/aaf740.

Ida, S. et al. (2020). “Uranian satellite formation by evolution of a water vapour disk generated by a giant impact”. *Nature Astronomy* Vol. 4, No. 9. DOI: 10.1038/s41550-020-1049-8.

Krapp, L. et al. (2024). “A Thermodynamic Criterion for the Formation of Circumplanetary Disks”. *The Astrophysical Journal* Vol. 973, No. 2. DOI: 10.3847/1538-4357/ad644a.

Le Gall, A. et al. (2014). “Iapetus’ near surface thermal emission modeled and constrained using Cassini RADAR Radiometer microwave observations”. *Icarus* Vol. 241. DOI: 10.1016/j.icarus.2014.06.011.

Lunine, J. I. et al. (1982). “Formation of the galilean satellites in a gaseous nebula”. *Icarus* Vol. 52, No. 1. DOI: 10.1016/0019-1035(82)90166-X.

Moore, J. et al. (2004). “Callisto”. *Jupiter: The Planet, Satellites and Magnetosphere*. Cambridge: Cambridge University Press.

Morbidelli, A. et al. (2012). “Explaining why the uranian satellites have equatorial prograde orbits despite the large planetary obliquity”. *Icarus* Vol. 219, No. 2. DOI: 10.1016/j.icarus.2012.03.025.

Muhleman, D. O. et al. (1991). “Observations of Mars, Uranus, Neptune, Io, Europa, Ganymede, and Callisto at a wavelength of 2.66 mm”. *Icarus* Vol. 92. DOI: 10.1016/0019-1035(91)90050-4.

Nixon, C. A. et al. (2020). “Detection of Cyclopropenylidene on Titan with ALMA”. *The Astronomical Journal* Vol. 160. DOI: 10.3847/1538-3881/abb679.

Palmer, M. Y. et al. (2017). “ALMA detection and astrobiological potential of vinyl cyanide on Titan”. *Science Advances* Vol. 3. DOI: 10.1126/sciadv.1700022.

Roth, N. X. et al. (2021). “Rapidly Varying Anisotropic Methanol (CH3OH) Production in the Inner Coma of Comet 46P/Wirtanen as Revealed by the ALMA Atacama Compact Array”. *The Planetary Science Journal* Vol. 2. DOI: 10.3847/PSJ/abdd3a.

Thelen, A. E. et al. (2022). “Variability in Titan’s Mesospheric HCN and Temperature Structure as Observed by ALMA”. *The Planetary Science Journal* Vol. 3. DOI: 10.3847/PSJ/ac7050.

Thelen, A. E. et al. (2024). “Subsurface Thermophysical Properties of Europa’s Leading and Trailing Hemispheres as Revealed by ALMA”. *The Planetary Science Journal* Vol. 5, No. 2. DOI: 10.3847/PSJ/ad251c.

Trumbo, S. K. et al. (2017). “ALMA Thermal Observations of a Proposed Plume Source Region on Europa”. *The Astronomical Journal* Vol. 154, No. 4. DOI: 10.3847/1538-3881/aa8769.

Trumbo, S. K. et al. (2018). “ALMA Thermal Observations of Europa”. *The Astronomical Journal* Vol. 156, No. 4. DOI: 10.3847/1538-3881/aada87.

Vanden Bout, P. A. et al. (2023). “The Millimeter Array”. *The ALMA Telescope: The Story of a Science Mega-Project*. Cambridge: Cambridge University Press. DOI: 10.1017/9781009279727.